THESIS

Persistency and Breathing Behavior of Chimera States in Nonlocally Coupled Phase Oscillators

Yusuke Suda

Department of Condensed Matter Physics,
Graduate School of Science, Hokkaido University

March 2019

Acknowledgements

The author is very grateful to Professor Koji Okuda and Professor Koji Nemoto for continuous guidance and encouragement. The author would also like to thank Professor Migaku Oda and Professor Takafumi Kita for helpful suggestions and critical reading. The author thanks all members of the Statistical Physics Laboratory for their encouragement.

Finally, I would like to thank my parents in Yamanashi for their mental and financial support.

Abstract

We study chimera states in the one-dimensional array of nonlocally coupled phase oscillators. The chimera state is a stable state characterized by the coexistence of coherent regions of synchronized oscillators and incoherent regions of drifting oscillators.

Chimera states are surely stable in the continuum limit with infinitely many oscillators. However, it is reported that in finitely discretized systems, chimera states are chaotic transient and finally collapse into the completely synchronous solution. In this thesis, we numerically study chimera states by using the coupling function different from the previous studies and show that chimera states can be stable even in the system composed of a small number of oscillators.

In most previous works, chimera states in the continuum limit are assumed to be stationary states. However, a few studies report the existence of breathing (oscillating) chimera states. In this thesis, we focus on multichimera states with two coherent and incoherent regions and numerically demonstrate that there can appear breathing multichimeras whose global order parameter oscillates temporally. Then, we show that the system exhibits a Hopf bifurcation from a stationary multichimera to a breathing one.

We also confirm that there appear another type of the breathing multichimera, which has the second coherent regions with the different average frequency in addition to the original coherent regions. Moreover, we show that the second coherent regions appear by increasing the amplitude of the breathing. Furthermore, we derive a new self-consistency equation extended for breathing chimeras and numerically solve it.

Contents

Chapter 1

Introduction

We study chimera states in nonlocally coupled phase oscillators. Chimera states are symmetry breaking appearing in a large group of identical self-sustained oscillators and are characterized by the coexistence of synchronized and desynchronized oscillators. In this chapter, we qualitatively explain the background of our studies and mention the purpose of this thesis in the last section.

1.1 Self-sustained Oscillator

There often appear self-sustained rhythmic phenomena in various natural or artificial dissipative systems [1,2]. For instance, the pendulum of a metronome oscillates with a constant frequency as long as energy is supplied. An electronic oscillator as typified by a triode generator persistently produces a periodically alternating current. The Belousov-Zhabotinsky reaction is a famous oscillating chemical reaction characterized by oscillation of concentration of the reactants. Others include neuronal firing, a circadian rhythm, light of a glow-worm, and the list goes on. These systems consist of respective different components. However, the self-sustained oscillations have universal properties and can be understood within a unified framework.

Self-sustained oscillators generally interact with one another. A many-body system composed of interacting self-sustained oscillators is called the

coupled oscillator system, which has been studied extensively in various scientific fields, e.g. physics, mathematics, chemistry, biology, and so on, for many years.

1.2 Limit Cycle

Self-sustained oscillators have their own rhythms and are maintained by internal energy sources. Therefore, even if an oscillator is separated from the external environment, it continues to oscillate autonomously. Such oscillators can be described within a class of nonlinear dissipative systems, and they are fundamentally different from harmonic oscillators in conservative systems and forced oscillators in forced systems.

An individual self-sustained oscillation is often described as the periodic motion on the *limit cycle* in the phase space. Note that some of self-sustained oscillators, such as chaotic oscillators, are not described as limit cycle oscillators, though we do not consider them in this thesis. The limit cycle is an isolated closed trajectory that depends only on parameters of the dynamical system and that does not depend on initial conditions. In contrast, the periodic motion in a conservative system is described as a family of infinite closed trajectories with respective different amplitudes, and one of them is practically chosen by an initial condition. Nonlinearity in the dynamical system is essential for the realization of limit cycle oscillations. Let $\boldsymbol{X}(t)$ be a periodic solution in a linear system such as a harmonic oscillator. Then, $c\boldsymbol{X}(t)$ is also a periodic solution for any constant c. Therefore, all periodic solutions in the linear system are not limit cycles, because $\boldsymbol{X}(t)$ is not "isolated".

Stability of the amplitude with respect to small perturbations also distinguishes between self-sustained oscillators and harmonic oscillators. The amplitude of a limit cycle oscillation is stable. Therefore, points in the neighborhood of the limit cycle trajectory gradually approach it. On the other hand, that of a harmonic oscillation is neutral. If the perturbation is added to a point on a periodic trajectory of the harmonic oscillation, it would forget the original trajectory and maintain the new trajectory.

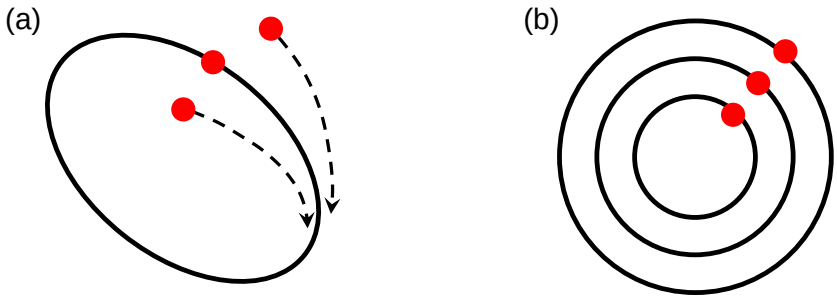

Figure 1.1: Schematic diagrams of (a) the limit cycle oscillator and (b) the harmonic oscillator in the phase space. In the nonlinear dissipative system, points in the neighborhood of the limit cycle trajectory gradually approach it. In contrast, each harmonic oscillator in the linear conservative system has a respective different amplitude.

The *phase* on a limit cycle is another important quantity. For simplicity, we consider the limit cycle of a quasilinear oscillator $X(t) = A\sin(\omega t + \theta_0)$. Then, the constant A is the amplitude, and the quantity $\theta(t) := \omega t + \theta_0$ is the phase. The phase on a limit cycle depends on the initial conditions, and limit cycle oscillations with any initial phase θ_0 are equivalently realized. This neutrality of the phase distinguishes self-sustained oscillators from forced oscillators in forced systems. The phase of a forced oscillation is not free, because it depends on the phase of the external force.

1.3 Synchronization & Chimera State

Synchronization is a typical collective motion of self-sustained oscillators. It was first discovered by Christiaan Huygens in the 17th century [2]. He observed that oscillations of two pendulum clocks hanging from a common wooden beam were gradually synchronized with each other and finally coincided perfectly. Furthermore, he found that weak interaction caused by the motion of the beam adjusted rhythms of clocks. At the present day, it is reported that synchronization is encountered in various systems. Moreover, it plays an important part in understanding a wide variety of scientific

phenomena.

Recently, a strange phenomenon called the *chimera state* has attracted great interest. The chimera state is a stable state appearing in a large group of coupled identical oscillators. Surprisingly, despite the system composed of identical oscillators, it has the spatiotemporal pattern characterized by the coexistence of synchronized and desynchronized oscillators. Such a pattern was first discovered by Kuramoto and Battogtokh [3]. Later Abrams and Strogatz named this phenomenon the chimera state inspired by the Greek mythological creature [4, 5].

Chimera states have been actively studied since the first discovery. One of the most basic models where chimera states appear is the one-dimensional array of nonlocally coupled phase oscillators [3–24], which was used also in the first discovery of the chimera state. Chimera states can also appear in the phase oscillator systems with different coupling topologies, e.g. two dimensions [25, 26], interacting populations of globally coupled oscillators [27–29], and the complex network [30]. Similar spatiotemporal patterns have been found in other oscillator systems, e.g. Logistic maps [31, 32], Rössler systems [31,32], Lorenz systems [32], FitzHugh-Nagumo oscillators [33], complex Ginzburg-Landau equations [3,34–36], Van der Pol oscillators [37], and Brusselators [38]. Furthermore, the appearance of chimera states is also reported experimentally [39–42].

1.4 Purpose of Thesis

In this thesis, we study chimera states in the one-dimensional array of nonlocally coupled phase oscillators. Chimera states in the one-dimensional systems are surely stable in the continuum limit $N \to \infty$, where N is the number of oscillators, while they are considered unstable in the finitely discretized systems [8–10]. Moreover, chimera states in the continuum limit are assumed to be stationary states in most analytical studies [3–6, 11, 13, 18, 23]. Our studies deal with two simple questions: (a) whether there exist persistent chimera states that are stable even in the finitely discretized systems,

and (b) whether there exist non-stationary chimera states in the continuum limit. We present the answers to these questions.

The contents of this thesis are as follows. In Chapters 2 and 3, we review the previous works of phase oscillators and chimera states, respectively. Then, we especially focus on the analytical theory. In Chapter 4, we consider the system with the coupling function different from the previous works and numerically demonstrate that there can appear persistent chimera states that are stable even in the system composed of a small number of oscillators. In Chapter 5, we numerically demonstrate that there can appear breathing (non-stationary) chimera states. Moreover, we show that the system exhibits a Hopf bifurcation from a stationary chimera to a breathing one by the linear stability analysis for the stationary chimera. In Chapter 6, we observe two types of breathing chimeras and show that the appearance of them is switched by increasing the amplitude of the breathing. Furthermore, we derive a new self-consistency equation extended for breathing chimeras and numerically solve it.

Chapter 2

Review: Phase Oscillator

First of all, we must understand the phase oscillator. If the external force is applied to a oscillator is sufficiently weak, the limit cycle oscillator can be transformed into the phase oscillator by the phase reduction method. In this chapter, we review the phase reduction method and analyze synchronization of phase oscillators. For all our numerical simulations of this thesis, we used the fourth-order Runge-Kutta method with time interval $\Delta t = 0.01$.

2.1 Examples of Dynamical Models

In this section, we introduce some mathematical models of self-sustained oscillators. A nonlinear dissipative system is often described as the n-dimensional dynamical system obeying the first-order ordinary differential equation

$$\dot{\boldsymbol{X}}(t) = \boldsymbol{F}(\boldsymbol{X}), \tag{2.1}$$

where $\boldsymbol{X} = [X_1, X_2, \cdots, X_n]^T \in \mathbb{R}^n$ and $\boldsymbol{F}$ is a real function of $\boldsymbol{X}$. A point $\boldsymbol{X}(t)$ in the phase space corresponds to the state of the system at time t. If Eq. (2.1) has a stable solution, appropriate initial conditions $\boldsymbol{X}(0)$ converge on it after a sufficiently long transient time. One of the typical solutions is the fixed point $\boldsymbol{X}_{\rm fp}(t)$ such that $\boldsymbol{F}(\boldsymbol{X}_{\rm fp}) = 0$. Moreover, the limit cycle $\boldsymbol{X}_{\rm lc}(t)$ is also a typical solution. Since $\boldsymbol{X}_{\rm lc}(t)$ is a periodic solution, there exists some $\tau > 0$ such that $\boldsymbol{X}_{\rm lc}(t+\tau) = \boldsymbol{X}_{\rm lc}(t)$ for all t. The minimum value

of τ is a period of $\boldsymbol{X}_{\rm lc}(t)$. The following examples are some of dynamical models with the stable limit cycle solution.

The Van der Pol oscillator [43] is an oscillator model with nonlinear damping and obeys the evolution equation

$$\ddot{X} = \epsilon(1 - X^2)\dot{X} - X, \tag{2.2}$$

where ϵ denotes the strength of nonlinear damping. This model was originally proposed as a mathematical model to describe stable oscillations in a triode circuit. When $\epsilon < 0$, Eq. (2.2) has a stable fixed point $X = 0$, but it does not have limit cycles. On the other hand, when $\epsilon > 0$, a stable limit cycle appears. For $\epsilon \simeq 0$, this limit cycle is quasilinear as shown in Fig. 2.1. As ϵ is increased, it becomes distorted and changes its form to the relaxation oscillator as shown in Fig. 2.2. Note that when $\epsilon = 0$, Eq. (2.2) is identical with a harmonic oscillator.

The FitzHugh-Nagumo oscillator [44, 45]

$$\begin{aligned} \dot{X} &= c(X - X^3/3 + Y), \\ \dot{Y} &= -(X - a + bY)/c, \end{aligned} \tag{2.3}$$

describes the action potential of an electrically excitable cell such as a neuron. The FitzHugh-Nagumo model is derived by simplifying the Hodgkin-Huxley model [46], which is famous for describing action potentials in the squid giant axon. Eq. (2.3) has a stable limit cycle solution that is the typical relaxation oscillator corresponding to the spike of neuronal firing, as shown in Fig. 2.3. When $a = b = 0$, Eq. (2.3) is identical with Eq. (2.2).

The Belousov-Zhabotinsky reaction is a well-known example of the self-sustained oscillation. The Brusselator [47]

$$\begin{aligned} \dot{X} &= a - (b + 1)X + X^2Y, \\ \dot{Y} &= bX - X^2Y, \end{aligned} \tag{2.4}$$

is one of the mathematical models describing such a oscillating chemical reaction. Eq. (2.4) has a stable fixed point $(X, Y) = (a, b/a)$ for $b < 1 + a^2$.

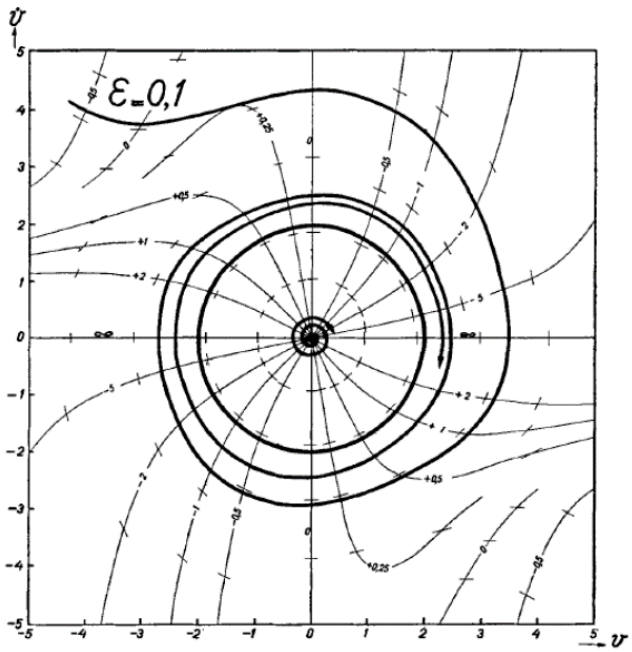

Figure 2.1: Limit cycle of the Van der Pol oscillator with $\epsilon = 0.1$. The variable v in the figure is the same as the variable X in Eq. (2.2) [43].

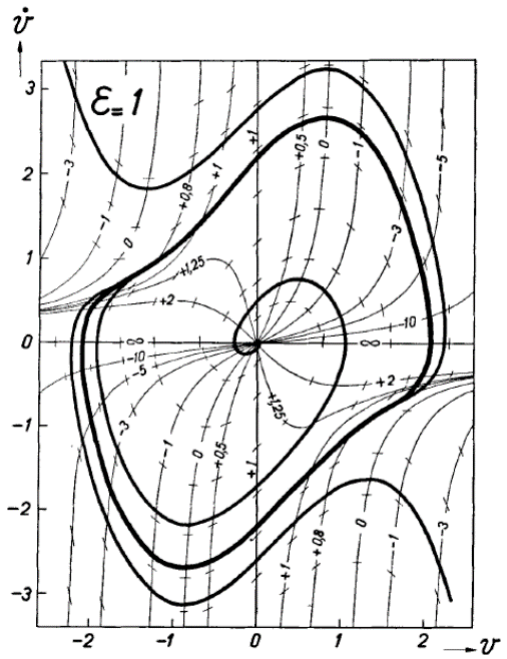

Figure 2.2: Limit cycle of the Van der Pol oscillator with $\epsilon = 1$ [43].

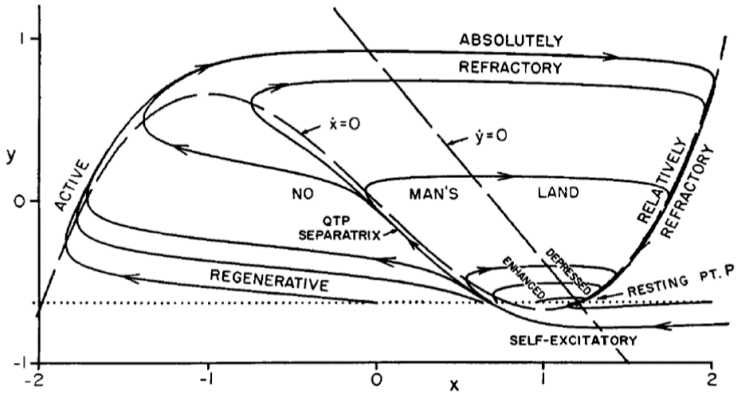

Figure 2.3: Limit cycle of the FitzHugh-Nagumo oscillator with $a = 0.7$, $b = 0.8$, and $c = 3.0$ [44].

However, when $b > 1 + a^2$, the fixed point becomes unstable, and a stable limit cycle appears by a Hopf bifurcation.

Each oscillator model has the oscillator's character that is important to describe the specific phenomenon. However, it may be obstructive to understanding the properties common to all limit cycle oscillators.

2.2 Phase Reduction Method

In this section, we derive the phase oscillator. The description of the limit cycle oscillator generally require at least two variables, namely, the amplitude and the phase. However, the phase oscillator expresses the limit cycle oscillation in only the motion of the phase. The method for deriving the phase oscillator from an original oscillator is called the *phase reduction method*.

2.2.1 Phase of Limit Cycle

First, we define the phase on a limit cycle. Let C be the stable limit cycle trajectory of Eq. (2.1).

Definition. *The phase $\theta(t)$ on the limit cycle C is defined as*

$$\dot{\theta}(t) = \omega, \tag{2.5}$$

where ω is a real constant. The constant ω is called the natural frequency and defined as

$$\omega = \frac{2\pi}{T}, \tag{2.6}$$

where T is a period of the limit cycle solution $\boldsymbol{X}_{\rm lc}(t)$.

The phase $\theta(t)$ increases at a constant velocity along C and by 2π per period. Then, θ and $\theta + 2m\pi$ for any $m \in \mathbb{Z}$ correspond to the same point, and any point on C can be set to the origin $\theta = 0$. Note that any limit cycle solution does not always rotate on C at a constant velocity. However, we can obtain the phase $\theta(t)$ defined as Eq. (2.5) with respect to any limit cycle solution because any angular variable $\phi(t)$ is transformed into $\theta(t)$ by

$$\theta(t) = \omega \int_0^{\theta(t)} d\phi \left[\frac{d\phi}{dt}\right]^{-1}. \tag{2.7}$$

Next, we define the phase in the neighborhood of the limit cycle. The new phase must be identical with Eq. (2.5) on C. A point $\boldsymbol{X}_S(t)$ in the neighborhood of C asymptotically approaches C with time and finally overlaps with a point $\boldsymbol{X}_P(t)$ rotating on C. Then, the point $\boldsymbol{X}_P(t)$ is uniquely determined since Eq. (2.1) is deterministic. Therefore, the phase in the neighborhood of C can be defined as follows.

Definition. *Let S be a subspace of the phase space that consists of the whole of initial conditions asymptotically approaching the limit cycle C with time. Now, there exists some point $\boldsymbol{X}_P(t)$ on C for any point $\boldsymbol{X}_S(t) \in S$ such that $\boldsymbol{X}_S(t)$ is identical with $\boldsymbol{X}_P(t)$ in $t \to \infty$. Then, the phase $\theta(t)$ of $\boldsymbol{X}_S(t)$ is defined as the same quantity to that of $\boldsymbol{X}_P(t)$ given as Eq. (2.5).*

The phase $\theta(t)$ uniformly rotate in the neighborhood of the limit cycle. Therefore, the phase is constant under the Poincaré map

$$\boldsymbol{X}(t) \to \boldsymbol{X}(t+T), \tag{2.8}$$

in the neighborhood of C. The map (2.8) has a stable fixed point $\boldsymbol{X}_{\rm lc}$ on C, and all points around $\boldsymbol{X}_{\rm lc}$ on the Poincaré section converge on it in $t \to \infty$.

The whole of points converging on $\boldsymbol{X}_{\rm lc}$ forms a $(n-1)$-dimensional hyperplane called the *isochrone*. Because the phase is constant on the isochrone, we can also define the phase as "all points on the isochrone have an identical phase given as Eq. (2.5)". The phase is the smooth function of $\boldsymbol{X}$ in the neighborhood of C. Substituting Eq. (2.1) and Eq. (2.5) into the identity

$$\dot{\theta} = \nabla_{\boldsymbol{X}}\theta \cdot \dot{\boldsymbol{X}}, \tag{2.9}$$

we have

$$\omega = \nabla_{\boldsymbol{X}}\theta \cdot \boldsymbol{F}(\boldsymbol{X}). \tag{2.10}$$

If the point $\boldsymbol{X}(t)$ is always in the neighborhood of the limit cycle, the behavior of this limit cycle oscillator is described by only the motion of the phase $\theta(t)$ very well. Therefore, we can consider Eq. (2.5) to be an oscillator, which is called the *phase oscillator*.

2.2.2 Phase Equation

When an oscillator obeying Eq. (2.1) is affected by the external force or the interaction with other oscillators, the evolution equation for the phase $\theta(t)$ changes from Eq. (2.5). Now, we consider the dynamical system of weakly coupled oscillator as

$$\dot{\boldsymbol{X}}(t) = \boldsymbol{F}(\boldsymbol{X}) + \boldsymbol{P}(t), \tag{2.11}$$

where $\boldsymbol{P}(t)$ is the small perturbation and denotes the external force. For instance, when $\boldsymbol{P}(t) = \hat{D}\nabla^2\boldsymbol{X}$ with the diffusion coefficient matrix $\hat{D}$, Eq. (2.11) is the reaction-diffusion system. From Eq. (2.10), we have

$$\begin{aligned} \dot{\theta} &= \nabla_{\boldsymbol{X}}\theta \cdot \dot{\boldsymbol{X}} \\ &= \nabla_{\boldsymbol{X}}\theta \cdot [\boldsymbol{F}(\boldsymbol{X}) + \boldsymbol{P}(t)] \\ &= \omega + \nabla_{\boldsymbol{X}}\theta \cdot \boldsymbol{P}(t). \end{aligned} \tag{2.12}$$

The trajectory of $\boldsymbol{X}(t)$ generally gets out of the limit cycle C by the perturbation. However, when $\boldsymbol{P}(t)$ is sufficiently small, the gap between them is

also small. Therefore, because it is permitted to replace $\nabla_{\boldsymbol{X}}$ to $\nabla_{\boldsymbol{X}_{\rm lc}} =: \boldsymbol{Z}(\theta)$, we finally obtain the *phase equation*

$$\dot{\theta} = \omega + \boldsymbol{Z}(\theta) \cdot \boldsymbol{P}(t). \tag{2.13}$$

This equation is the self-contained equation for $\theta(t)$.

When oscillators are weakly coupled, the sum of interactions with other oscillators can be considered as one small perturbation. Now, we consider coupled two oscillators

$$\begin{aligned} \dot{\boldsymbol{X}}_1 &= \boldsymbol{F}(\boldsymbol{X}_1) + \delta \boldsymbol{f}_1(\boldsymbol{X}_1) + \boldsymbol{g}_{12}(\boldsymbol{X}_1, \boldsymbol{X}_2), \\ \dot{\boldsymbol{X}}_2 &= \boldsymbol{F}(\boldsymbol{X}_2) + \delta \boldsymbol{f}_2(\boldsymbol{X}_2) + \boldsymbol{g}_{21}(\boldsymbol{X}_1, \boldsymbol{X}_2), \end{aligned} \tag{2.14}$$

where $\delta \boldsymbol{f}$ denotes the slight difference of individual oscillators and $\boldsymbol{g}$ denotes the interaction. Let $\theta(t) = \omega t$ be the phase of the standard oscillator obeying Eq. (2.1), and let $\theta_1(t)$ and $\theta_2(t)$ be the phase of each oscillator obeying Eq. (2.14), respectively. From Eq. (2.13), the evolution equation for $\theta_1(t)$ is obtained as

$$\dot{\theta}_1 = \omega + \boldsymbol{Z}(\theta_1) \cdot [\delta \boldsymbol{f}_1(\boldsymbol{X}_1) + \boldsymbol{g}_{12}(\boldsymbol{X}_1, \boldsymbol{X}_2)]. \tag{2.15}$$

Because $\delta \boldsymbol{f}$ and $\boldsymbol{g}$ are small perturbations, the variables $\boldsymbol{X}_1(t)$ and $\boldsymbol{X}_2(t)$ can be replaced to $\boldsymbol{X}_{\rm lc}(\theta_1)$ and $\boldsymbol{X}_{\rm lc}(\theta_2)$ on the limit cycle of Eq. (2.1), respectively. Therefore, we have

$$\dot{\theta}_1 = \omega + \boldsymbol{Z}(\theta_1) \cdot [\delta \boldsymbol{f}_1(\theta_1) + \boldsymbol{g}_{12}(\theta_1, \theta_2)]. \tag{2.16}$$

To simplify notation, we change the arguments of $\delta \boldsymbol{f}$ and $\boldsymbol{g}$ from $\boldsymbol{X}_{\rm lc}(\theta)$ to θ. Putting $\phi_{1,2}(t) := \theta_{1,2}(t) - \omega t$, Eq. (2.16) is rewritten as

$$\dot{\phi}_1 = \boldsymbol{Z}(\omega t + \phi_1) \cdot [\delta \boldsymbol{f}_1(\omega t + \phi_1) + \boldsymbol{g}_{12}(\omega t + \phi_1, \omega t + \phi_2)]. \tag{2.17}$$

This equation means that the variable $\phi_1(t)$ changes much more slowly than ωt, and $\phi_2(t)$ is also similar. Therefore, considering $\phi_{1,2}$ to be the constant

and temporally averaging Eq. (2.17) over the period $T = 2\pi/\omega$, we have

$$\dot{\phi}_1 = \delta\omega_1 + \Gamma_{12}(\phi_1 - \phi_2), \tag{2.18}$$

$$\delta\omega_1 := \frac{1}{2\pi}\int_0^{2\pi} d\theta\, \boldsymbol{Z}(\theta + \phi_1) \cdot \delta\boldsymbol{f}_1(\theta + \phi_1), \tag{2.19}$$

$$\Gamma_{12}(\phi_1 - \phi_2) := \frac{1}{2\pi}\int_0^{2\pi} d\theta\, \boldsymbol{Z}(\theta + \phi_1) \cdot \boldsymbol{g}_{12}(\theta + \phi_1, \theta + \phi_2), \tag{2.20}$$

where $\delta\omega_1$ is constant not depending on $\phi_1(t)$ and Γ_{12} is a smooth 2π-periodic function of the phase difference. Obviously, $\phi_2(t)$ also obeys the similar equations. Putting $\omega_{1,2} := \omega + \delta\omega_{1,2}$, we finally obtain the phase equations

$$\begin{aligned} \dot{\theta}_1 &= \omega_1 + \Gamma_{12}(\theta_1 - \theta_2), \\ \dot{\theta}_2 &= \omega_2 + \Gamma_{21}(\theta_2 - \theta_1). \end{aligned} \tag{2.21}$$

Eq. (2.21) brings a physical picture such that two phase oscillators with different natural frequencies ω_1 and ω_2 interact with each other by the *coupling function* Γ.

In the case of the N-body system, we can also obtain the similar phase equations

$$\dot{\theta}_j = \omega_j + \frac{1}{N}\sum_{k=1}^{N} \Gamma_{jk}(\theta_j - \theta_k), \tag{2.22}$$

with $j = 1, \cdots, N$. The coefficient $1/N$ is inserted in order to prevent the divergence of the interaction term in $N \to \infty$. The coupling function Γ is a smooth 2π-periodic function. For instance, when we choose

$$\Gamma_{jk}(\phi) = -K\sin(\phi), \tag{2.23}$$

where $K > 0$ denotes the coupling strength, Eq. (2.22) becomes the *Kuramoto model* [1]

$$\dot{\theta}_j = \omega_j - \frac{K}{N}\sum_{k=1}^{N} \sin(\theta_j - \theta_k), \tag{2.24}$$

which is famous for describing the synchronization of self-sustained oscilla-

tors.

2.3 Synchronization

In this section, we consider coupled identical phase oscillators and analyze synchronization of them. The word "identical" means that the dynamics of each oscillator is described as the identical evolution equation. Therefore, the natural frequency ω_j and the coupling function Γ_{jk} do not depend on indexes of oscillators. As the coupling function, we choose the sine coupling [48]

$$\Gamma(\phi) = -K\sin(\phi + \alpha), \tag{2.25}$$

with the phase lag parameter $\alpha \in [-\pi, \pi)$. The sine coupling consists of only the fundamental component of the coupling function. Phase oscillators with the sine coupling have been heavily used in many studies.

2.3.1 Two-Body System

We consider coupled two phase oscillators with the sine coupling

$$\begin{aligned} \dot{\theta}_1(t) &= \omega - K\sin[\theta_1(t) - \theta_2(t) + \alpha], \\ \dot{\theta}_2(t) &= \omega - K\sin[\theta_2(t) - \theta_1(t) + \alpha], \end{aligned} \tag{2.26}$$

with 2π-periodic phase $\theta(t) \in [-\pi, \pi)$. Eq. (2.26) has two synchronous solutions such that $\dot{\theta}_1 = \dot{\theta}_2$. Putting $\Delta\theta(t) := \theta_2(t) - \theta_1(t)$, the evolution equation for $\Delta\theta(t)$ is obtained as

$$\begin{aligned} \frac{d}{dt}[\Delta\theta(t)] &= -K[\sin(\Delta\theta(t) + \alpha) - \sin(-\Delta\theta(t) + \alpha)] \\ &= -2K\cos\alpha\sin[\Delta\theta(t)]. \end{aligned} \tag{2.27}$$

Then, we can set $\Delta\theta(t) \in [0, 2\pi)$ without loss of generality. Synchronous solutions for Eq. (2.26) correspond to fixed points for Eq. (2.27), namely,

$\Delta\theta = 0$ and $\Delta\theta = \pi$. Therefore, two synchronous solutions for Eq. (2.26) are

$$\theta_1 = \theta_2, \tag{2.28}$$

$$\theta_1 = \theta_2 + \pi. \tag{2.29}$$

Eq. (2.28) denotes *in-phase synchronization* where two oscillators completely coincide and are synchronized with a frequency $\omega - K\sin\alpha$. On the other hand, Eq. (2.29) denotes *anti-phase synchronization* where oscillators are separated from each other by the phase π though they are synchronized with an identical frequency $\omega + K\sin\alpha$. By the way, when synchronization was first discovered by Christian Huygens, he observed anti-phase synchronization of two pendulum clocks [2].

Eq. (2.26) always has in-phase and anti-phase synchronous solutions. However, when either one is stable, the other is unstable. This can be shown by the *linear stability analysis* for each solution. Before actually studying the stability of Eq. (2.28) and Eq. (2.29), we explain the general linear stability analysis. As the easiest case, we consider a fixed point $\boldsymbol{X}_{\rm fp}$ of Eq. (2.1). Substituting $\boldsymbol{X}_{\rm fp} + \boldsymbol{V}(t)$ with a small perturbation $\boldsymbol{V}(t) \in \mathbb{R}^n$ into Eq. (2.1) and linearizing it, we obtain a linear evolution equation for $\boldsymbol{V}(t)$ as

$$\begin{aligned} \dot{\boldsymbol{V}}(t) &= \boldsymbol{F}(\boldsymbol{X}_{\rm fp} + \boldsymbol{V}) - \boldsymbol{F}(\boldsymbol{X}_{\rm fp}) \\ &\simeq \hat{L}(\boldsymbol{X}_{\rm fp})\boldsymbol{V}(t), \end{aligned} \tag{2.30}$$

where $\hat{L}$ is the Jacobian matrix of $\boldsymbol{F}$ at a point $\boldsymbol{X}_{\rm fp}$:

$$\hat{L}(\boldsymbol{X}_{\rm fp}) = \frac{\partial \boldsymbol{F}}{\partial \boldsymbol{X}}(\boldsymbol{X}_{\rm fp}). \tag{2.31}$$

It is clear that the stability of $\boldsymbol{X}_{\rm fp}$ is determined by eigenvalues of $\hat{L}$. When the real parts of all eigenvalues are negative, $\boldsymbol{V}(t)$ decreases with time and finally becomes zero. Therefore, $\boldsymbol{X}_{\rm fp}$ is stable. On the other hand, when any one of eigenvalues has the positive real part, $\boldsymbol{V}(t)$ diverges in $t \to \infty$, that is, $\boldsymbol{X}_{\rm fp}$ is unstable. Also, when the maximum value of the real parts of eigenvalues is zero, $\boldsymbol{X}_{\rm fp}$ is neutral or neutrally stable.

	$0 \leq \lvert\alpha\rvert < \pi/2$	$\pi/2 < \lvert\alpha\rvert \leq \pi$
in-phase	stable	unstable
anti-phase	unstable	stable

Table 2.1: Stability regions of two synchronous solutions to Eq. (2.26).

To study the stability of Eq. (2.28) and Eq. (2.29) more easily, we use Eq. (2.27) again. Because $\hat{L}$ of Eq. (2.27) at a fixed point $\Delta\theta_{\rm fp}$ is obtained as

$$\hat{L}(\Delta\theta_{\rm fp}) = -2K\cos\alpha\cos(\Delta\theta_{\rm fp}), \tag{2.32}$$

we have

$$\hat{L}(0) = -2K\cos\alpha, \tag{2.33}$$

$$\hat{L}(\pi) = 2K\cos\alpha, \tag{2.34}$$

for in-phase synchronization ($\Delta\theta_{\rm fp} = 0$) and anti-phase synchronization ($\Delta\theta_{\rm fp} = \pi$), respectively. Tab. 2.1 shows the stability regions of the in-phase and anti-phase synchronous solutions. Here, for $|\alpha| = \pi/2$, both of solutions are neutral. Fig. 2.4 shows the time evolution of $\theta_1(t)$ and $\theta_2(t)$ obtained by the numerical simulation of Eq. (2.26). There appear in-phase synchronization for $\alpha = 0$ and anti-phase synchronization for $\alpha = \pi$. These results are in good agreement with Tab. 2.1. Note that the natural frequency ω and the coupling strength K do not affect the appearance of solutions essentially.

2.3.2 Globally Coupled Phase Oscillators

Next, we consider coupled N identical phase oscillators

$$\dot{\theta}_j(t) = \omega - \frac{K}{N}\sum_{k=1}^{N}\sin[\theta_j(t) - \theta_k(t) + \alpha], \tag{2.35}$$

with $j = 1, \cdots, N$. In this system, all oscillators are coupled with the uniform coupling strength. Such a system is called the *globally coupled system*. Here, the natural frequency ω can be set to zero without loss of generality because

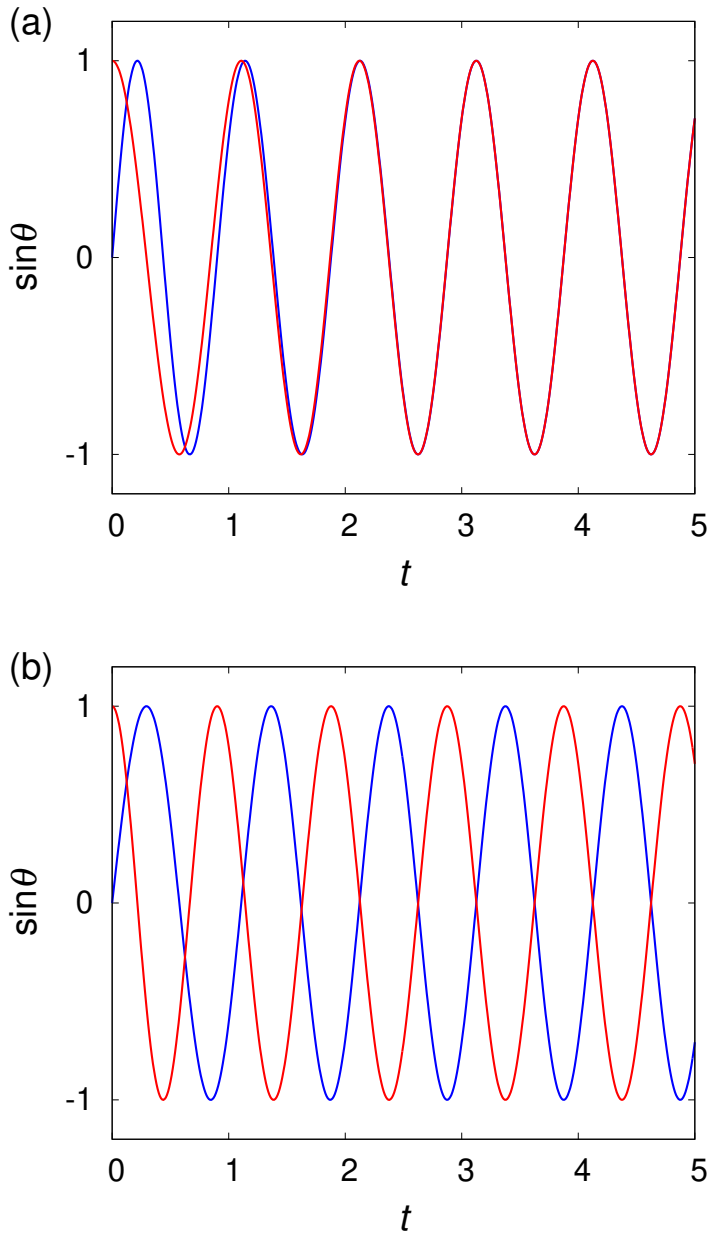

Figure 2.4: Time evolution of phase oscillators for Eq. (2.26) with $\omega = 2\pi$ and $K = 1$. The blue and red lines denote $\theta_1(t)$ and $\theta_2(t)$, respectively. There appear (a) in-phase synchronization for $\alpha = 0$ and (b) anti-phase synchronization for $\alpha = \pi$.

Eq. (2.35) with $\omega = 0$ can be also obtained by redefining all phases as $\theta(t) - \omega t \to \theta(t)$. This is the same as setting the frequency of the rotating frame to ω. Similarly, we can set $K = 1$ because the appearance of solutions to Eq. (2.35) are not affected by rescaling the time as $Kt \to t$. These are in agreement with the results in the previous section.

To study the collective motion of phase oscillators, we define the global order parameter

$$Z(t) := \frac{1}{N} \sum_{j=1}^{N} e^{i\theta_j(t)}. \tag{2.36}$$

$|Z(t)|$ denotes the synchronization degree of oscillators, that is, all oscillators are completely synchronized in phase for $|Z(t)| = 1$ and otherwise for $0 \leq |Z(t)| < 1$. The global order parameter $Z(t)$ also plays an role as the mean field. From Eq. (2.36), Eq. (2.35) is rewritten as

$$\dot{\theta}_j(t) = \omega - K \,\mathrm{Im}[e^{i\alpha} e^{i\theta_j(t)} Z^*(t)], \tag{2.37}$$

where the symbol $*$ denotes the complex conjugate. Eq. (2.37) brings a physical picture such that each independent phase oscillator is driven under the common mean field $Z(t)$.

Eq. (2.35) also has two synchronous solutions similar to Eq. (2.26). For $0 \leq |\alpha| < \pi/2$, all oscillators completely synchronized in phase with a frequency $\omega - K \sin\alpha$, that is,

$$\theta_1(t) = \theta_2(t) = \cdots = \theta_N(t), \tag{2.38}$$

for $|Z(t)| = 1$, as shown in Fig. 2.5(a). On the other hand, for $\pi/2 < |\alpha| \leq \pi$, oscillators converge on $|Z(t)| = 0$, as shown in Fig. 2.5(b). Then, all oscillators are uniformly distributed from $-\pi$ to π. The stability of these solutions can be studied by calculating eigenvalues of the $N \times N$ Jacobian matrix of Eq. (2.35). However, we study it more easily by another method in Section 2.3.5.

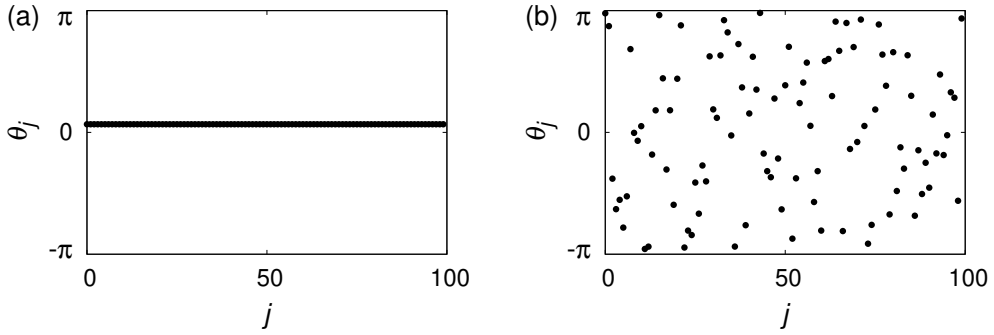

Figure 2.5: Snapshot of the phase $\theta_j(t)$ for the globally coupled phase oscillators described as Eq. (2.35) with $N = 100$. (a) For $\alpha = 0$, all oscillators are completely synchronized in phase for $|Z(t)| = 1$. (b) For $\alpha = \pi$, they converge on $|Z(t)| = 0$. We use the initial conditions selected uniformly at random.

2.3.3 Watanabe-Strogatz approach

To describe the collective motion of phase oscillators, it may not always be necessary to observe the behavior of all oscillators. By using the Watanabe-Strogatz approach [49], the population of phase oscillators can be described as the dynamics of three dynamical variables and constants determined by initial conditions.

Watanabe-Strogatz approach. *The dynamics of N (≥ 3) phase oscillators described as*

$$\dot{\theta}_j(t) = p(t) - \mathrm{Im}[e^{i\theta_j(t)} q^*(t)], \tag{2.39}$$

where $p(t)$ is a real function and $q(t)$ is a complex function, is reduced to that of three real variables $\rho(t)$, $\Phi(t)$, and $\Psi(t)$ via the transformation

$$\tan\left[\frac{\theta_j(t) - \Phi(t)}{2}\right] = \frac{1-\rho(t)}{1+\rho(t)} \tan\left[\frac{\psi_j - \Psi(t)}{2}\right], \tag{2.40}$$

where the constants ψ_j are determined from initial conditions $\theta_j(0)$ and satisfy the additional condition, for instance,

$$\sum_{j=1}^{N} e^{i\psi_j} = 0. \tag{2.41}$$

Putting $\eta(t) := \rho(t)e^{i\Phi(t)}$ *and* $\zeta(t) := \Phi(t) - \Psi(t)$*, we finally obtain the evolution equation*

$$\dot{\eta}(t) = ip(t)\eta(t) + \frac{1}{2}q(t) - \frac{1}{2}\eta(t)^2 q^*(t), \tag{2.42}$$

$$\dot{\zeta}(t) = p(t) - \mathrm{Im}[\eta(t)q^*(t)]. \tag{2.43}$$

Then, the time evolution of $\theta_j(t)$ *is completely described as that of* $\eta(t)$ *and* $\zeta(t)$ *governed by Eqs. (2.42)-(2.43).*

We omit the details of the Watanabe-Strogatz approach, but we actually derive Eqs. (2.42)-(2.43) for globally coupled phase oscillators. As the more generalized system, we consider M interacting populations of globally coupled N phase oscillators

$$\dot{\theta}_j^a(t) = \omega_a - \frac{1}{N}\sum_{b=1}^{M}\sum_{k=1}^{N} K_{ab}\sin[\theta_j^a(t) - \theta_k^b(t) + \alpha], \tag{2.44}$$

with $j = 1, \cdots, N$ and $a = 1, \cdots, M$. The variable $\theta_j^a(t)$ denotes the phase of oscillator j in population a, and the constant K_{ab} denotes the coupling strength between populations a and b. Of course, for $M = 1$, Eq. (2.44) is identical with Eq. (2.35). We define the global order parameter of population a as

$$Z_a(t) := \frac{1}{N}\sum_{j=1}^{N} e^{i\theta_j^a(t)}, \tag{2.45}$$

and the mean field acting the oscillators in population a as

$$Y_a(t) := \sum_{b=1}^{M} K_{ab} Z_b(t). \tag{2.46}$$

Then, since Eq. (2.44) is rewritten as

$$\dot{\theta}_j^a(t) = \omega_a - \mathrm{Im}[e^{i\alpha}e^{i\theta_j^a(t)}Y_a^*(t)], \tag{2.47}$$

the Watanabe-Strogatz approach can be applied to each population [28].

From $p_a(t) = \omega_a$ and $q_a(t) = e^{-i\alpha}Y_a(t)$, Eqs. (2.42)-(2.43) become

$$\dot{\eta_a}(t) = i\omega_a\eta_a(t) + \frac{1}{2}e^{-i\alpha}Y_a(t) - \frac{1}{2}e^{i\alpha}\eta_a(t)^2Y_a^*(t), \tag{2.48}$$

$$\dot{\zeta_a}(t) = \omega_a - \mathrm{Im}[e^{i\alpha}\eta_a(t)Y_a^*(t)]. \tag{2.49}$$

New variables has the following physical meaning. The dynamics of the complex variable $\eta_a(t)$ composed of $\rho_a(t)$ and $\Phi_a(t)$ corresponds to the motion of the bunch of oscillators in population a. In particular, $\eta_a(t)$ is identical with the global order parameter $Z_a(t)$ in the continuum limit $N \to \infty$ [28]. Therefore, in $N \to \infty$, Eqs. (2.48)-(2.49) become

$$\dot{Z}_a(t) = i\omega_a Z_a(t) + \frac{1}{2}e^{-i\alpha}Y_a(t) - \frac{1}{2}e^{i\alpha}Z_a(t)^2Y_a^*(t), \tag{2.50}$$

$$\dot{\zeta_a}(t) = \omega_a - \mathrm{Im}[e^{i\alpha}Z_a(t)Y_a^*(t)]. \tag{2.51}$$

Then, Eq. (2.50) is the self-contained equation for $Z_a(t)$. Another variable $\Psi_a(t)$ corresponds to the shift of individual oscillators with respect to the bunch. Therefore, the variable $\zeta_a(t)$ means the phase difference between the bunch and individual oscillators.

2.3.4 Ott-Antonsen ansatz

The Ott-Antonsen ansatz [50,51] is another well-known reduction method to the lower-dimensional system. We consider the system described as Eq. (2.47) for large N again. Let $f_a(\theta, t)$ be the probability density function of the phase θ in population a at time t. Then, the continuity equation is

$$\frac{\partial}{\partial t}f_a(\theta,t) = -\frac{\partial}{\partial\theta}\left[\left\{\omega_a - \mathrm{Im}[e^{i\alpha}e^{i\theta}Y_a^*(t)]\right\}f_a(\theta,t)\right]. \tag{2.52}$$

When N is sufficiently large, the global order parameter $Z_a(t)$ given as Eq. (2.45) is also obtained as

$$Z_a(t) = \frac{1}{2\pi}\int_{-\pi}^{\pi} d\theta f_a(\theta,t)e^{i\theta}. \tag{2.53}$$

The Ott-Antonsen ansatz determines the form of $f_a(\theta, t)$ as follows.

Ott-Antonsen ansatz. *Eq. (2.52) has an attracting invariant manifold that contains all relevant dynamics of Eq. (2.44) for sufficiently large N. Then, the probability density function $f_a(\theta, t)$ is given as*

$$f_a(\theta, t) = \frac{1}{2\pi}\left(1 + \sum_{k=1}^{\infty}[Z_a^*(t)e^{ik\theta} + Z_a(t)e^{-ik\theta}]\right), \tag{2.54}$$

where $Z_a(t)$ denotes the global order parameter given as Eq. (2.53).

Substituting Eq. (2.54) into Eq. (2.52), we can obtain the evolution equation for $Z_a(t)$ as Eq. (2.50), which have been obtained by the Watanabe-Strogatz approach in $N \to \infty$. The Ott-Antonsen ansatz is just an "ansatz", but it is well known that this ansatz can be applied to various phase oscillator systems.

2.3.5 Stability of Synchronization

Let us study the stability of synchronous solutions for globally coupled phase oscillators by using Eq. (2.50), as mentioned in Section 2.3.2. In the system described as Eq. (2.37), we have $Y(t) = Ke^{-i\alpha}Z(t)$. Therefore, Eq. (2.50) becomes

$$\dot{Z}(t) = i\omega Z(t) + \frac{K}{2}e^{-i\alpha}Z(t) - \frac{K}{2}e^{i\alpha}|Z(t)|^2 Z(t). \tag{2.55}$$

Putting $R(t)e^{i\Theta(t)} := Z(t)$, the evolution equations for the amplitude $R(t)$ and the argument $\Theta(t)$ are obtained as

$$\dot{R}(t) = \frac{K}{2}\cos\alpha[R(t) - R(t)^3], \tag{2.56}$$

$$\dot{\Theta}(t) = \omega - \frac{K}{2}\sin\alpha[1 + R(t)^2]. \tag{2.57}$$

Here, Eq. (2.57) holds for $R(t) \neq 0$. It is clear that fixed points of $R(t)$ are $R = 1$ and $R = 0$. For $R = 1$, the frequency of synchronized oscillators is $\dot{\Theta}(t) = \omega - K\sin\alpha$. Because the dynamics of $R(t)$ is independent of $\Theta(t)$, we may consider only the Jacobian matrix $\hat{L}_R$ of Eq. (2.56) in order to study

	$0 \leq \lvert\alpha\rvert < \pi/2$	$\pi/2 < \lvert\alpha\rvert \leq \pi$
$R = 1$	stable	unstable
$R = 0$	unstable	stable

Table 2.2: Stability regions of two synchronous solutions to Eq. (2.35).

the stability of synchronous solutions:

$$\hat{L}_R(R) = \frac{K}{2}\cos\alpha(1 - 3R^2). \tag{2.58}$$

For each fixed point, we have

$$\hat{L}_R(1) = -K\cos\alpha, \tag{2.59}$$

$$\hat{L}_R(0) = \frac{K}{2}\cos\alpha. \tag{2.60}$$

Therefore, we obtain the stability regions of $R = 1$ and $R = 0$ as shown in Tab. 2.2. When $|\alpha| = \pi/2$, both of them are neutral. These results are in good agreement with Fig. 2.5 in Section 2.3.2.

The reduction method such as the Watanabe-Strogatz approach or the Ott-Antonsen ansatz is extremely useful for understanding the collective motion of phase oscillators. That is similar in the case of chimera states mentioned in the next chapter.

Chapter 3

Review: Chimera State

In this chapter, we review the previous works of chimera states. Although it is known that chimera states can be seen in a wide variety of systems, we especially focus on chimera states in the one-dimensional array of nonlocally coupled phase oscillators.

3.1 Feature of Chimera States

3.1.1 Nonlocally Coupled Phase Oscillators

As the most basic models, we consider N identical phase oscillators uniformly distributed on the one-dimensional ring. In the continuum limit $N \to \infty$, the dynamics of oscillators is described as

$$\dot{\theta}(x,t) = \omega - \int_{-\pi}^{\pi} dy\, G(x-y)\, \Gamma[\theta(x,t) - \theta(y,t)], \tag{3.1}$$

with 2π-periodic phase $\theta(x,t) \in [-\pi, \pi)$ on the one-dimensional space $x \in [-\pi, \pi)$ under the periodic boundary condition. The natural frequency ω can be set to zero without loss of generality. In this system, the coupling strength characterized by the *coupling kernel* $G(x)$ depends on the distance between oscillators. Such a system is called the *nonlocally coupled system*. Eq. (3.1)

was originally derived from the dynamical model [52]

$$\begin{aligned}
&\dot{\boldsymbol{X}}(x,t) = \boldsymbol{F}[\boldsymbol{X}(x,t)] + \boldsymbol{U}[A(x,t)], \\
&\epsilon \dot{A}(x,t) = -(1 - D\nabla^2)A(x,t) + \int dy\, W[\boldsymbol{X}(y,t)]\delta(x-y),
\end{aligned} \tag{3.2}$$

where $\boldsymbol{U}(A)$ and $W(\boldsymbol{X})$ are general functions of A and $\boldsymbol{X}$, respectively. This model denotes the dynamics of biologically oscillating cells $\boldsymbol{X}$ with the extra substance A mediating interaction between cells. If N is finite, we discretize x into $x_j := -\pi + 2\pi j/N$ $(j = 1, \cdots, N)$ and rewrite Eq. (3.1) as

$$\dot{\theta}_j(t) = \omega - \frac{2\pi}{N} \sum_{k=1}^{N} G_{jk}\, \Gamma[\theta_j(t) - \theta_k(t)], \tag{3.3}$$

where $\theta_j(t) := \theta(x_j, t)$ and $G_{jk} := G(x_j - x_k)$. For numerical simulations of Eq. (3.1), we need to do this discretization.

As the coupling function Γ, the sine coupling [48]

$$\Gamma(\phi) = -\sin(\phi + \alpha), \tag{3.4}$$

is most often used in the study on chimera states [3–13, 15, 18–23, 25–30]. In particular, the phase lag parameter α is essential for the appearance of chimera states. Instead of the sine coupling, the coupling with higher harmonic components is sometimes used [14, 16, 17], for instance, the Hansel-Mato-Meunier coupling [53]

$$\Gamma(\phi) = -\sin(\phi + \alpha) + r\sin(2\phi), \tag{3.5}$$

where r is the amplitude ratio of the second harmonic component. For $r = 0$, Eq. (3.5) recovers the sine coupling. In the globally coupled systems, it is known that such higher harmonic components in the coupling function are responsible for a rich variety of synchronous patterns excluded by the sine coupling [53–58]. Therefore, it is expected that also in the nonlocally coupled systems, there could appear new chimera patterns excluded by the sine coupling.

The coupling kernel $G(x)$ is generally an even real function described as

$$G(x) = \sum_{k=0}^{\infty} g_k \cos(kx), \tag{3.6}$$

with $g_k \in \mathbb{R}$. In the study on chimera states, one of the following coupling schemes is usually chosen.

(i) The exponential kernel [3, 6, 20]:

$$G(x) = \frac{\kappa}{2} e^{-\kappa|x|}, \tag{3.7}$$

where $\kappa > 0$ is a real constant. When the chimera state was first discovered, this coupling was used. Eq. (3.7) is the Green's function associated with the operator $1 - D\nabla^2$ in Eq. (3.2) on $x \in [-\infty, \infty]$. Recently, as the exponential kernel revised on $x \in [0, L)$ under the periodic boundary condition, the hyperbolic kernel

$$G(x) = \frac{\kappa}{2\sinh(\kappa L/2)} \cosh\left[\kappa\left(|x| - \frac{L}{2}\right)\right], \tag{3.8}$$

is also used [18, 19, 21].

(ii) The step kernel [8–12, 16, 22–24]:

$$G(x) = \begin{cases} 1/(2\pi s) & (|x| \le \pi s) \\ 0 & (|x| > \pi s), \end{cases} \tag{3.9}$$

with $0 < s \le 1$. The constant s denotes the coupling range. This kernel is very functional for numerical simulations because the discretized system (3.3) with the step kernel becomes the simple form

$$\dot{\theta}_j(t) = \omega + \frac{1}{2R} \sum_{k=j-R}^{j+R} \Gamma[\theta_j(t) - \theta_k(t)], \tag{3.10}$$

where $R := sN/2$. All the indexes in Eq. (3.10) are regarded as modulo N.

(iii) The cosine kernel [4, 5, 7, 13]:

$$G(x) = A_0 + A_1 \cos(x) + A_2 \cos(2x), \tag{3.11}$$

with $A_0, A_1, A_2 \in \mathbb{R}$. This kernel is often useful for analytical calculations. In addition, it is also used when the systems with negative coupling at large separations, such as neural systems, are studied.

3.1.2 Chimera State

Let us consider nonlocally coupled phase oscillators with the sine coupling described as

$$\dot{\theta}(x,t) = \omega - \int_{-\pi}^{\pi} dy\, G(x-y)\, \sin[\theta(x,t) - \theta(y,t) + \alpha]. \tag{3.12}$$

In this system, there appears the chimera state as shown in Fig. 3.1. The phase pattern [see Fig. 3.1(a)] is clearly separated into two different regions, called the *coherent region* and the *incoherent region*. The coherent region consists of phase-locked oscillators, while the incoherent region consists of drifting oscillators whose phases are scattered from $-\pi$ to π. Fig. 3.1(b) shows the average frequency of each oscillator:

$$\langle \dot{\theta}(x) \rangle := \frac{1}{T} \int_0^T dt'\, \dot{\theta}(x,t'), \tag{3.13}$$

with the measurement time T. In this thesis, $\langle \cdot \rangle$ denotes the time-averaged quantity after a sufficiently long transient time. In the coherent region, oscillators are completely synchronized, and their average frequencies are constant. In contrast, the average frequency in the incoherent region varies continuously. The coexistence of coherent and incoherent regions is the most essential feature of chimera states. Such a chimera basically can not appear in globally coupled or locally (nearest neighbor) coupled phase oscillators [5].

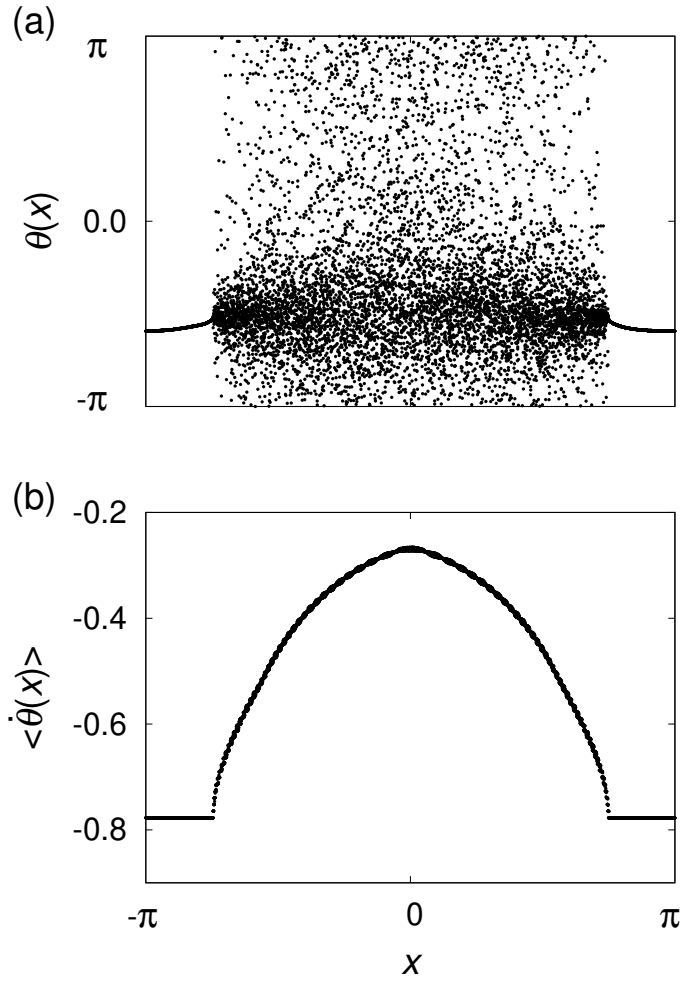

Figure 3.1: Chimera state for Eq. (3.12) with the step kernel. Parameters are $N = 10000$, $\alpha = 1.500$, and $s = 0.700$. (a) The snapshot of the phase $\theta(x,t)$. (b) The profile of the average frequency $\langle\dot{\theta}(x)\rangle$ with $T = 500$.

There also exist chimera states with two or more coherent and incoherent regions, which are often called *multichimera states*. A typical multichimera state with two coherent and incoherent regions is shown in Fig. 3.2. Then, though there exist two coherent regions, all oscillators in the coherent regions have an identical average frequency. However, two coherent regions are separated from each other by the phase almost exactly π, which is a remarkable feature of this multichimera and different from merely two neighboring chimeras. Note that the number of coherent and incoherent regions generally depends on the coupling kernel $G(x)$ and chosen parameters [11].

3.2 Self-Consistency Analysis

3.2.1 Self-Consistency Equation

In this section, we review the self-consistency analysis for chimera states based on [3]. We define the local mean field

$$Y(x,t) := \int_{-\pi}^{\pi} dy\, G(x-y)\, e^{i\theta(y,t)}, \tag{3.14}$$

acting on the oscillator located in point x. Then, Eq. (3.12) is rewritten as

$$\dot{\theta}(x,t) = \omega - \mathrm{Im}[e^{i\alpha} e^{i\theta(x,t)} Y^*(x,t)]. \tag{3.15}$$

Here, we make an important assumption about chimera states.

Assumption. *In the continuum limit $N \to \infty$, the chimera state for Eq. (3.12) is a stationary state in the rotating frame with an appropriate frequency Ω. Then, the probability density function $f_x(\phi, t)$ of the phase $\phi(x,t)$ such that $\phi(x,t) := \theta(x,t) - \Omega t$ is independent of time.*

This assumption means that the local mean field takes the form

$$Y(x,t) = Y_{\mathrm{st}}(x)\, e^{i\Omega t}. \tag{3.16}$$

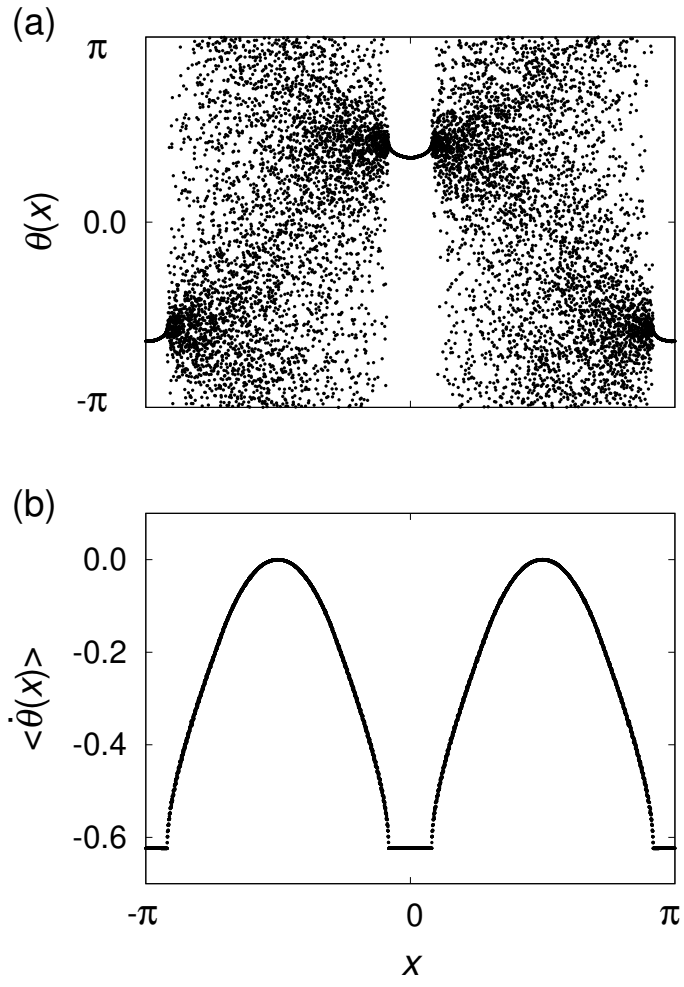

Figure 3.2: Multichimera state for Eq. (3.12) with the step kernel. Parameters are $N = 10000$, $\alpha = 1.500$, and $s = 0.360$. All figures show the same quantities as those in Fig. 3.1.

Then, $Y_{\rm st}(x)$ is defined as

$$Y_{\rm st}(x) = \int_{-\pi}^{\pi} dy\, G(x-y)\, e^{i\phi(y,t)}. \tag{3.17}$$

However, if infinitely many oscillators are contained in each small local subsystem, Eq. (3.17) can be considered as

$$Y_{\rm st}(x) = \int_{-\pi}^{\pi} dy\, G(x-y) \int_{-\pi}^{\pi} d\phi\, f_y(\phi)\, e^{i\phi}. \tag{3.18}$$

We derive the self-consistency equation for $Y_{\rm st}(x)$ from Eq. (3.18).

Putting $Y_{\rm st}(x) =: R(x)e^{i\Theta(x)}$, Eq. (3.15) becomes

$$\dot{\phi}(x,t) = \Delta - R(x)\sin[\phi(x,t) - \Theta(x) + \alpha] =: V_x(\phi), \tag{3.19}$$

where $\Delta := \omega - \Omega$. In coherent regions, it is clear that oscillators have the frequency Ω and satisfy $\dot{\phi} = 0$. From Eq. (3.19), if $R(x) \geq \Delta$, we have the synchronous solution

$$\phi(x) = \arcsin\left[\frac{\Delta}{R(x)}\right] + \Theta(x) - \alpha. \tag{3.20}$$

Eq. (3.20) consists of two solutions, but the stable solution is either one satisfying

$$\frac{dV_x(\phi)}{d\phi} = -R(x)\cos[\phi - \Theta(x) + \alpha] < 0. \tag{3.21}$$

Therefore, we obtain

$$\begin{aligned} e^{i\phi(x)} &= e^{-i\alpha}e^{i\Theta(x)}\left[\sqrt{1-\left(\frac{\Delta}{R(x)}\right)^2} + i\left(\frac{\Delta}{R(x)}\right)\right] \\ &= ie^{-i\alpha}Y_{\rm st}(x)\,\frac{\Delta - i\sqrt{R(x)^2-\Delta^2}}{R(x)^2}. \end{aligned} \tag{3.22}$$

Then, $f_x(\phi)$ is the Dirac delta function.

If $R(x) < \Delta$, we have the drifting solution instead of the synchronous

solution. From the continuity equation

$$0 = -\frac{\partial}{\partial\phi}\left[V_x(\phi) f_x(\phi)\right], \tag{3.23}$$

we have

$$f_x(\phi) = \frac{C}{V_x(\phi)}, \tag{3.24}$$

where the normalizing constant C satisfies

$$C = \left| \int_{-\pi}^{\pi} d\phi \, \frac{1}{V_x(\phi)} \right|^{-1} = \frac{1}{2\pi}\sqrt{\Delta^2 - R(x)^2}. \tag{3.25}$$

Applying Eqs. (3.24)-(3.25), we can obtain

$$\int_{-\pi}^{\pi} d\phi \, f_x(\phi)\, e^{i\phi} = ie^{-i\alpha} Y_{\rm st}(x) \frac{\Delta - \sqrt{\Delta^2 - R(x)^2}}{R(x)^2}. \tag{3.26}$$

Substituting Eq. (3.22) and Eq. (3.26) into Eq, (3.18), we obtain the self-consistency equation for $Y_{\rm st}(x)$ as

$$Y_{\rm st}(x) = ie^{-i\alpha} \int_{-\pi}^{\pi} dy \, Y_{\rm st}(y)\, h(y), \tag{3.27}$$

$$h(x) := \begin{cases} [\Delta - \sqrt{\Delta^2 - R(x)^2}]/R(x)^2 & [\Delta > R(x)] \\ [\Delta - i\sqrt{R(x)^2 - \Delta^2}]/R(x)^2 & [\Delta \leq R(x)]. \end{cases} \tag{3.28}$$

As the sign of the square root of a negative number in Eq. (3.28), we can also choose

$$\sqrt{R(x)^2 - \Delta^2} = -i\sqrt{\Delta^2 - R(x)^2}. \tag{3.29}$$

Then, the self-consistency equation becomes one equation [4, 5]:

$$Y_{\rm st}(x) = ie^{-i\alpha} \int_{-\pi}^{\pi} dy \, Y_{\rm st}(y) \, \frac{\Delta - \sqrt{\Delta^2 - R(x)^2}}{R(x)^2}. \tag{3.30}$$

Solutions to this self-consistency equation include all stationary states for Eq. (3.12), which are not only chimera states but synchronous solutions.

According to [11], chimera solutions to Eq. (3.30) are bifurcated from the completely incoherent solution satisfying $|Z(t)| = 0$ at $\alpha = \pi/2$ and exist for $\alpha < \pi/2$.

3.2.2 Solving Self-Consistency Equation

The self-consistency equation (3.30) is composed of two equations given by the real and imaginary parts, but it has two real unknown functions and one real unknown, namely, $R(x)$, $\Theta(x)$, and Δ. Therefore, we need to add another condition to solve it. The additional condition can be obtained from the fact that Eq. (3.30) are invariant under any rotation, $\Theta(x) \to \Theta(x) + \Theta_0$ [4–6, 13, 16]. This means that the argument $\Theta(x)$ on any point can be set to the arbitrary fixed value, for instance,

$$\Theta(-\pi) = 0. \tag{3.31}$$

Eq. (3.30) under the condition (3.31) can be numerically solved by the following iteration procedure. First, we prepare an initial function $Y_{\rm st}(x)$, i.e., $R(x)$ and $\Theta(x)$. Then, an initial Δ satisfying Eq. (3.31) can be obtained from Eq. (3.30) by Newton's method with respect to Δ. Second, substituting $Y_{\rm st}(x)$ and Δ into the right-hand side of Eq. (3.30), we generate a new $Y_{\rm st}(x)$ from the left-hand side. Third, we obtain a new Δ satisfying Eq. (3.31), again by Newton's method, using the new $Y_{\rm st}(x)$. It only remains to repeat the second and third steps until both $Y_{\rm st}(x)$ and Δ converge. Note that space translational symmetry of $Y_{\rm st}(x)$ is not eliminated in this iteration procedure, so the spatial position of $Y_{\rm st}(x)$ depends on the initial $Y_{\rm st}(x)$.

Fig. 3.3 shows the numerical solution $Y_{\rm st}(x)$ to the self-consistency equation (3.30) for the chimera state. It agrees with the time-averaged local mean field $\langle Y_{\rm st}(x)\rangle$ obtained by the numerical simulation.

3.2.3 Average Frequency

By using $Y_{\rm st}(x)$ and Δ, we can analytically calculate the average frequency $\langle\dot{\theta}(x)\rangle$ for stationary chimera states [3]. From Eqs. (3.24)-(3.25), the average

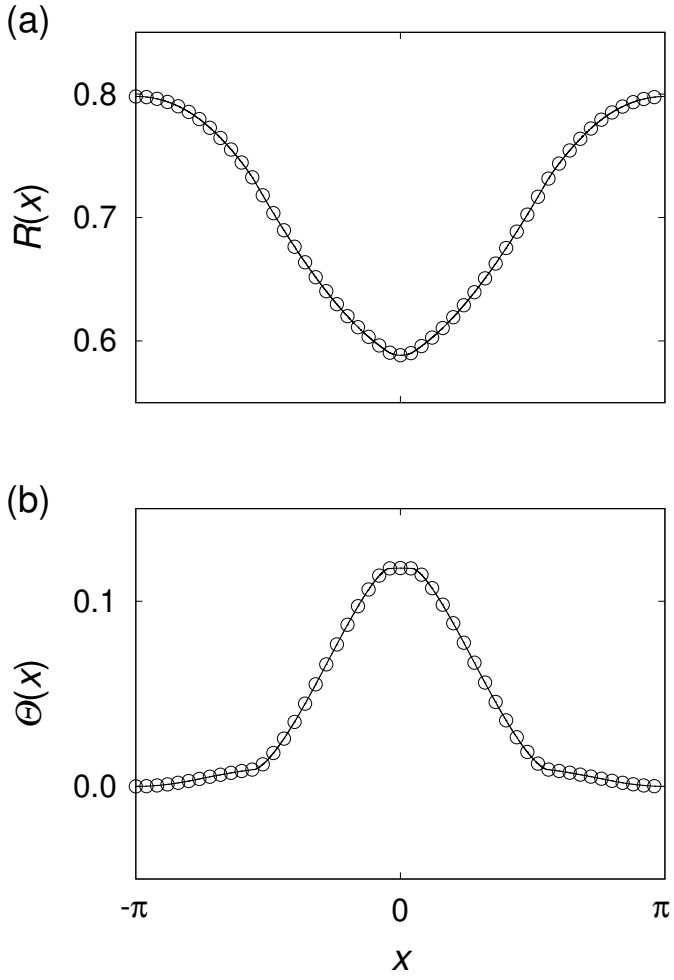

Figure 3.3: Local mean field $Y_{\rm st}(x)$ of the stationary chimera state as shown in Fig. 3.1. (a) The amplitude $R(x)$; (b) The argument $\Theta(x)$. Open circles denote the time-averaged local mean field $\langle Y_{\rm st}(x)\rangle$ obtained by the numerical simulation. Those are plotted once every 2000 oscillators. The solid line denotes the numerical solution $Y_{\rm st}(x)$ to the self-consistency equation (3.30) under the condition (3.31).

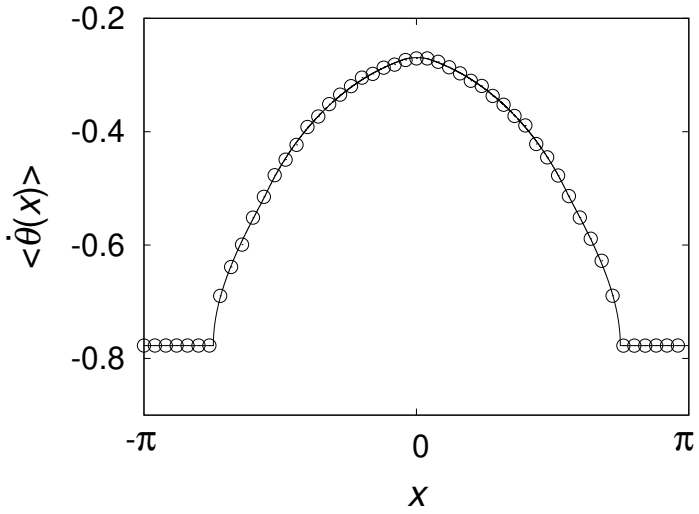

Figure 3.4: Average frequency $\langle\dot{\theta}(x)\rangle$ for the stationary chimera state. Open circles are the same date in Fig. 3.1(b) which are plotted once every 2000 oscillators. The solid line denotes Eq. (3.33) computed from the numerical solutions $Y_{\rm st}(x)$ and Δ in Fig. 3.3.

frequency of each oscillator in incoherent regions can be calculated as

$$\begin{aligned}\langle\dot{\theta}(x)\rangle &= \Omega + \int_{-\pi}^{\pi} d\phi\, f_x(\phi)\,\dot{\phi} \\ &= \Omega + \int_{-\pi}^{\pi} d\phi\, \frac{C}{V_x(\phi)}\, V_x(\phi) \\ &= \Omega + \sqrt{\Delta^2 - R(x)^2}. \end{aligned} \tag{3.32}$$

Therefore, $\langle\dot{\theta}(x)\rangle$ in the whole space is given by

$$\langle\dot{\theta}(x)\rangle = \begin{cases} \Omega + \sqrt{\Delta^2 - R(x)^2} & [\Delta > R(x)] \\ \Omega & [\Delta \le R(x)]. \end{cases} \tag{3.33}$$

Using the numerical solutions $Y_{\rm st}(x)$ and Δ to the self-consistency equation, we can compute Eq. (3.33). It agrees with the result of the numerical simulation as shown in Fig. 3.4.

3.3 Stability of Chimera States

The self-consistency analysis helps us theoretically to understand chimera states. However, just because the self-consistency equation has a chimera solution does not mean that the chimera state is stable. This section deals with the stability of chimera states.

3.3.1 Linear Stability Analysis

To study the stability of chimera states for Eq. (3.12), we define the local order parameter

$$z(x,t) := \lim_{\epsilon \to 0+} \frac{1}{2\epsilon} \int_{x-\epsilon}^{x+\epsilon} dy\, e^{i\theta(y,t)}, \tag{3.34}$$

and we have

$$Y(x,t) = \int_{-\pi}^{\pi} dy\, G(x-y)\, z(y,t). \tag{3.35}$$

$|z(x,t)|$ denotes the synchronization degree of oscillators around point x, similarly to the global order parameter $|Z(t)|$. For $|z(x,t)| = 1$, the oscillators in the neighborhood of x are completely synchronized in phase. Otherwise, when their phases are scattered, we obtain $0 \leq |z(x,t)| < 1$. Therefore, we can identify $|z(x,t)| = 1$ and $0 \leq |z(x,t)| < 1$ as the coherent and incoherent regions for chimera states, respectively. In $N \to \infty$, the system described as Eq. (3.15) can be considered as interacting subpopulations of globally coupled infinite oscillators in each small local subsystem, similar to Eq. (2.44). In this case, the local order parameter $z(x,t)$ is considered as the global order parameter in the local subsystem around x. Therefore, applying the Watanabe-Strogatz approach to each subpopulation, we obtain the evolution equation for $z(x,t)$ [9] as

$$\dot{z}(x,t) = i\omega z(x,t) + \frac{1}{2} e^{-i\alpha} Y(x,t) - \frac{1}{2} e^{i\alpha} z^2(x,t) Y^*(x,t). \tag{3.36}$$

Instead of Eq. (3.34), the local order parameter can be also defined as

$$z(x,t) = \int_{-\pi}^{\pi} d\theta\, f_x(\theta,t)\, e^{i\theta}, \tag{3.37}$$

where $f_x(\theta, t)$ is the probability density function of the phase $\theta(x)$ at time t. Then, Eq. (3.36) can be obtained by another method [7, 11] using the Ott-Antonsen ansatz.

We assume that chimera states are stationary again. Similarly to Eq. (3.16), the local order parameter takes the form

$$z(x,t) = z_{\rm st}(x)\, e^{i\Omega t}. \tag{3.38}$$

Substituting Eq. (3.16) and Eq. (3.38) into Eq. (3.36), we have

$$0 = i\Delta z_{\rm st}(x) + \frac{1}{2}e^{-i\alpha}Y_{\rm st}(x) - \frac{1}{2}e^{i\alpha}z_{\rm st}^2(x)Y_{\rm st}^*(x). \tag{3.39}$$

Solving Eq. (3.39) as a quadratic equation in terms of $z_{\rm st}(x)$, the solutions are

$$z_{\rm st}(x) = ie^{-i\alpha}\frac{\Delta \pm \sqrt{\Delta^2 - |Y_{\rm st}(x)|^2}}{Y_{\rm st}^*(x)}. \tag{3.40}$$

When $\Delta > |Y_{\rm st}(x)|$, the solution with the negative sign of the square root satisfies $|z(x,t)| < 1$, while the other does not. On the other hand, When $\Delta \leq |Y_{\rm st}(x)|$, both of solutions satisfy $|z(x,t)| = 1$. However, the stable solution in coherent regions is either one satisfying Eq. (3.21). Therefore, as the stable solution satisfying $|z(x,t)| \leq 1$ in the whole space, we obtain

$$z_{\rm st}(x) = ie^{-i\alpha}\, Y_{\rm st}(x)\, h(x), \tag{3.41}$$

$$h(x) = \begin{cases} [\Delta - \sqrt{\Delta^2 - |Y_{\rm st}(x)|^2}]/|Y_{\rm st}(x)|^2 & [\Delta > |Y_{\rm st}(x)|] \\ [\Delta - i\sqrt{|Y_{\rm st}(x)|^2 - \Delta^2}]/|Y_{\rm st}(x)|^2 & [\Delta \leq |Y_{\rm st}(x)|], \end{cases} \tag{3.42}$$

where $h(x)$ is the same equation as Eq. (3.28). Fig. 3.5 shows the local order parameter for the stationary chimera state given as Eqs. (3.41)-(3.42). Integrating Eq. (3.41), we obtain the self-consistency equation for $Y_{\rm st}(x)$ as

$$Y_{\rm st}(x) = ie^{-i\alpha}\int_{-\pi}^{\pi} dy\, G(x-y)Y_{\rm st}(y)\, h(y). \tag{3.43}$$

This equation corresponds to the self-consistency equation (3.27) in the pre-

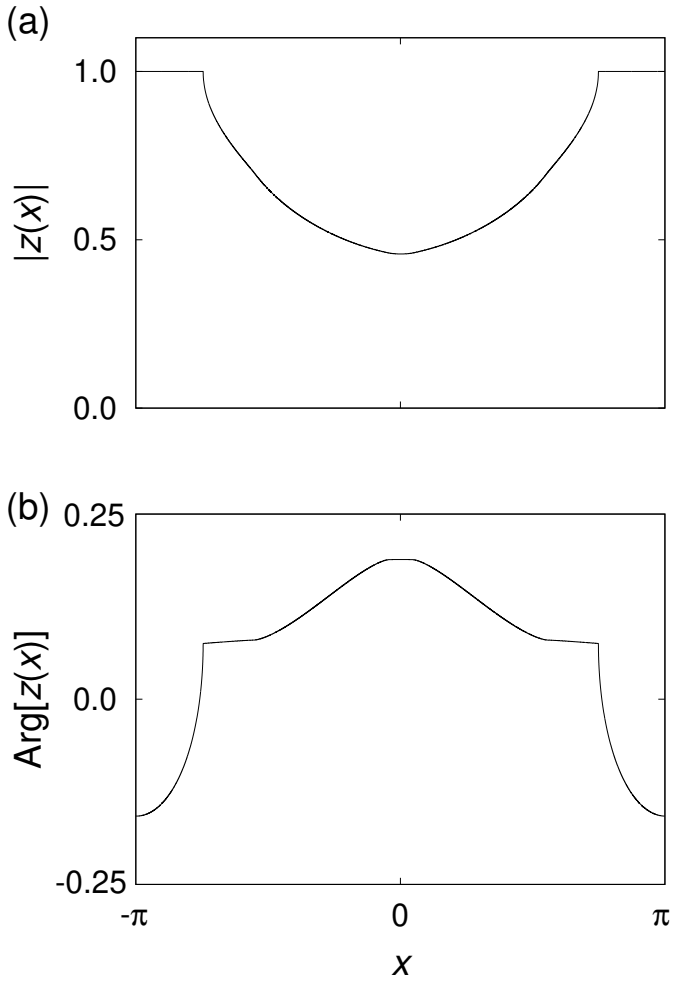

Figure 3.5: Local order parameter $z_{\rm st}(x)$ for the stationary chimera state as shown in Fig. 3.1. (a) The amplitude $|z_{\rm st}(x)|$; (b) the argument of $z(x,t)$. These figures are obtained by Eq. (3.41) from the numerical solutions $Y_{\rm st}(x)$ and Δ corresponding to Fig. 3.3.

vious section.

Let us consider the linear stability analysis for stationary chimeras. Substituting $z(x,t) = [z_{\rm st}(x) + v(x,t)]\, e^{i\Omega t}$ with a small perturbation $v(x,t)$ into Eq. (3.36), we obtain a linear evolution equation for $v(x,t)$ as

$$\dot{v}(x,t) = g(x) z_{\rm st}(x) + \frac{1}{2} e^{-i\alpha} V(x,t) - \frac{1}{2} e^{i\alpha} z_{\rm st}^2(x) V^*(x,t), \tag{3.44}$$

$$g(x) := \begin{cases} i\sqrt{\Delta^2 - R(x)^2} & [\Delta > R(x)] \\ -\sqrt{R(x)^2 - \Delta^2} & [\Delta \le R(x)], \end{cases} \tag{3.45}$$

$$V(x,t) := \int_{-\pi}^{\pi} dy\, G(x-y)\, v(y,t). \tag{3.46}$$

We rewrite Eqs. (3.44)-(3.46) as $\dot{\boldsymbol{v}} = \hat{L}\, \boldsymbol{v}$ using $\boldsymbol{v}(x,t) = [\mathrm{Re}\, v(x,t),\, \mathrm{Im}\, v(x,t)]^T$. To study the linear stability of stationary chimeras, we must solve the eigenvalue problem of $\hat{L}$, which is generally an infinite dimensional matrix. According to [11, 13, 23], the spectrum of $\hat{L}$ consists of the essential spectrum and the point spectrum. In the present case, the essential spectrum is given by

$$\{g(x) : -\pi \le x \le \pi\} \cup \{c.c.\}, \tag{3.47}$$

consisting of pure imaginary and negative real eigenvalues, which correspond to incoherent and coherent regions, respectively, as shown in Fig. 3.6. Therefore, the stability of stationary chimeras should be determined only by the point spectrum. If the number of nonzero g_k in Eq. (3.6) is finite, such as the cosine kernel, we may solve the eigenvalue problem of a finite size matrix to obtain the point spectrum [11, 13, 23]. However, when the kernel has infinite numbers of nonzero g_k, such as the step kernel, we must directly compute all eigenvalues of $\hat{L}$, as mentioned in Chapter 5.

3.3.2 Lyapunov Spectrum

Chimera states are surely stable in the continuum limit $N \to \infty$. However, the stability of chimeras in finitely discretized systems is questioned. Wolfrum *at al.* [9] studied the Lyapunov spectrum of chimera states for Eq. (3.12)

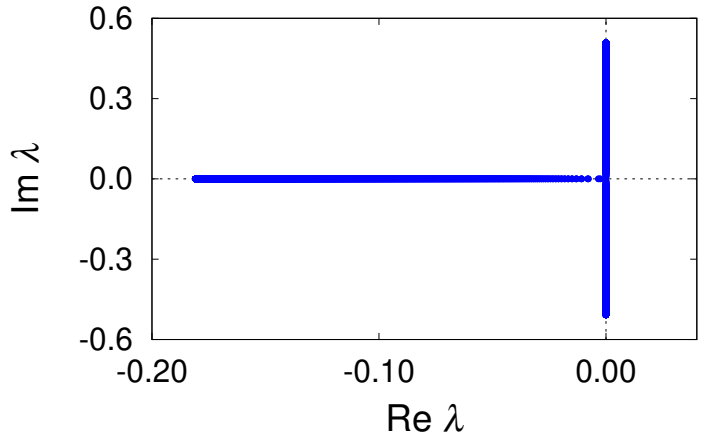

Figure 3.6: Essential spectrum λ calculated by Eq. (3.47) from the numerical solutions $Y_{\rm st}(x)$ and Δ in Fig. 3.3. The dashed lines are drawn only for reference.

with the step kernel. The Lyapunov exponent is defined as follows. We consider a point $\boldsymbol{X}(t)$ in the neighborhood of a solution for Eq. (2.1) at $t = 0$. Letting $\delta\boldsymbol{X}_\nu(t)$ be the separation along an eigenvector $\boldsymbol{e}_\nu$ of the Jacobian matrix $\hat{L}$ from the solution, the Lyapunov exponent $\Lambda(\nu)$ is defined as the following real scalar:

$$\Lambda(\nu) := \lim_{t\to\infty} \frac{1}{t} \ln \left| \frac{\delta\boldsymbol{X}_\nu(t)}{\delta\boldsymbol{X}_\nu(0)} \right|. \tag{3.48}$$

Therefore, we have

$$\delta\boldsymbol{X}_\nu(t) = e^{\Lambda(\nu)t}\, \delta\boldsymbol{X}_\nu(0). \tag{3.49}$$

When $\Lambda(\nu) > 0$, the separation $\delta\boldsymbol{X}_\nu(t)$ exponentially diverges with time. In contrast, when $\Lambda(\nu) < 0$, it converges on zero. Therefore, if all Lyapunov exponents are not positive, the solution is stable or neutral stable.

Fig. (3.7) shows Lyapunov spectra $\Lambda_N(\nu)$ numerically computed for chimera trajectories. The indexes ν of the Lyapunov exponents are sorted in the order such that $\Lambda_1(\nu) \le \Lambda_2(\nu) \le \cdots \le \Lambda_N(\nu)$. For finite N, chimera states have the positive Lyapunov exponents, that is, they are unstable. Moreover, as N is increased, the maximal Lyapunov exponent decreases and approaches

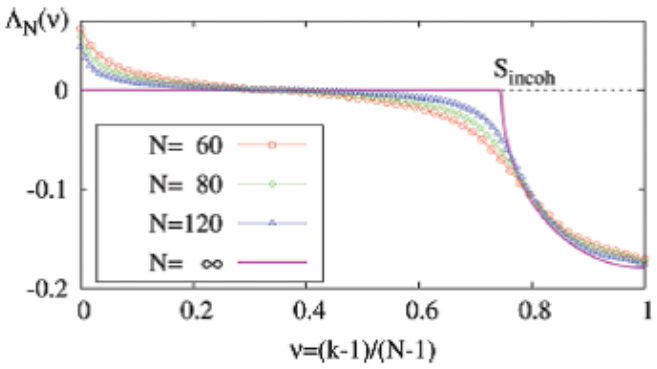

Figure 3.7: Lyapunov spectra $\Lambda_N(\nu)$ computed for chimera trajectories of Eq. (3.12) with the step kernel. Parameters are $s = 0.700$ and $\alpha = 1.500$ [9].

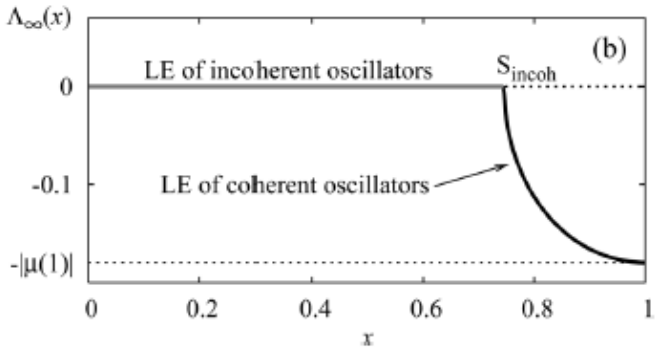

Figure 3.8: Lyapunov spectra $\Lambda_\infty(x)$ of the chimera state in $N \to \infty$. Parameters are the same as those in Fig. (3.7) [9].

zero. In $N \to \infty$, the Lyapunov spectrum of chimera states is given by

$$\Lambda_\infty(x) := \begin{cases} 0 & [0 \le x \le S_{\rm incoh}] \\ -\sqrt{|Y_{\rm st}(x)|^2 - \Delta^2} & [S_{\rm incoh} < x \le 1]. \end{cases} \tag{3.50}$$

where x denotes the continuum parameter corresponding to ν, as shown in Fig. 3.8. $\Lambda_\infty(x)$ corresponds to the real part of the essential spectrum given by Eq. (3.45) and Eq. (3.47). Similarly to the essential spectrum, $\Lambda_\infty(x) < 0$ (stable) and $\Lambda_\infty(x) = 0$ (neutral) correspond to coherent and incoherent regions, respectively. Therefore, it is shown that chimera states are neutral stable in $N \to \infty$, but they become unstable for finite N.

3.3.3 Chimera's Collapse

Even if N is finite, we have observed that chimera states are maintained in numerical simulations where we can not use infinite N in principle. However, for especially small N, chimera states are chaotic transient [10, 42]. As shown in Fig. 3.9, the chimera state composed of a few oscillators suddenly collapses without advance notice and changes over to the completely synchronous state. Fig. 3.10 shows the histogram of lifetimes τ of chimera states obtained by numerical simulations of Eq. (3.12) with the step kernel using different initial conditions. The distribution of the lifetimes $\rho(\tau)$ clearly follows an exponential low

$$\rho(\tau) = \gamma e^{-\gamma t}, \tag{3.51}$$

with a constant collapse rate γ and the average lifetime

$$\langle \tau \rangle = \gamma^{-1}. \tag{3.52}$$

Therefore, it is concluded that the chimera's collapse is randomly caused by the finite size effect.

Fig. 3.11 shows average lifetimes $\langle \tau \rangle$ of chimera states for increasing N. They are fitted by an exponential growth

$$\langle \tau \rangle \propto e^{\xi N}, \tag{3.53}$$

with an exponential rate $\xi = 0.23$. From this result, it is shown that lifetimes of chimeras diverge to infinity in $N \to \infty$. In [10], the authors mentioned that it is very unlikely to observe even a single collapse event in numerical simulations for $N \geq 60$.

3.3.4 Weak Chimera

As mentioned above, chimera states in the one-dimensional system with the sine coupling are unstable without taking the continuum limit $N \to \infty$. On the other hand, Ashwin and Burylko [14] used the Hansel-Mato-Meunier coupling (3.5) and proposed the *weak chimera* similar to the chimera state.

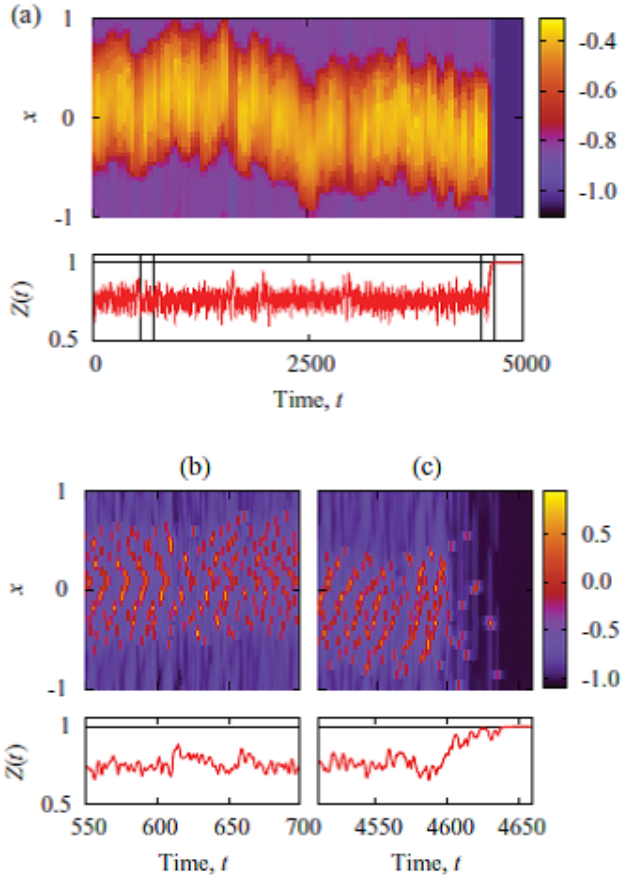

Figure 3.9: Chimera's collapse for Eq. (3.12) with the step kernel. Parameters are $N = 40$, $R = 14$, and $\alpha = 1.460$. The whole space is defined as $x \in [-1, 1]$. Figures (a) show the space time plot of the average frequency $\langle \dot{\theta}(x) \rangle$ and the global order parameter $|Z(t)|$. The chimera state suddenly collapses to the completely synchronous state at $t \simeq 4600$. Figures (b) and (c) show a magnification of segments well before the collapse and directly at the collapse [10].

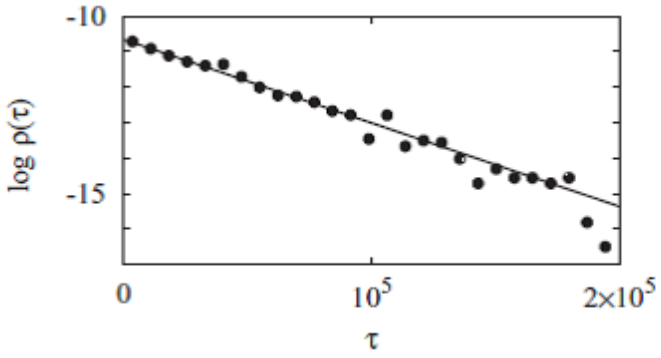

Figure 3.10: Histogram of lifetimes τ of chimera states obtained by 2000 numerical simulations (circles). The data is plotted in logarithmic scale with fitted exponential distribution (solid line). Parameters are the same as those in Fig. (3.9) [10].

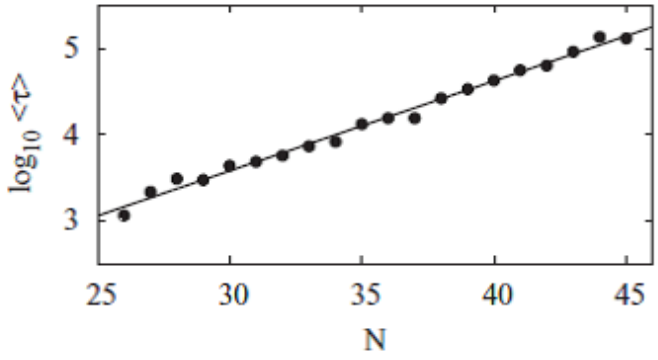

Figure 3.11: Average lifetimes $\langle\tau\rangle$ of chimera states for increasing N (circles) and fitted exponential growth (solid line). Each point is obtained by 2000 numerical simulations with $R/N \simeq 0.350$ and $\alpha = 1.460$ [10].

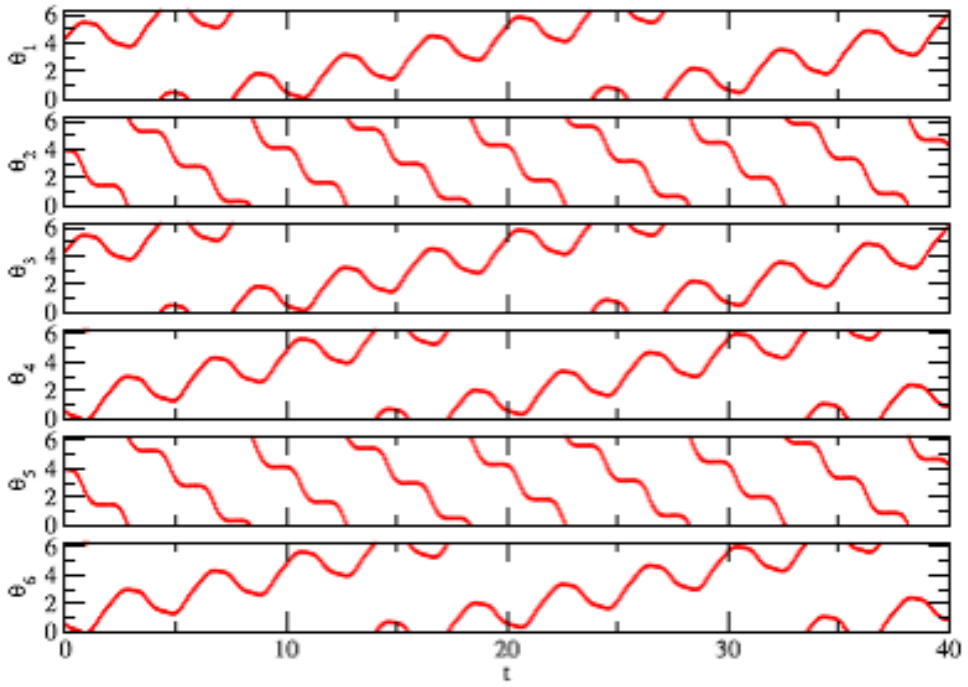

Figure 3.12: Weak chimera in the ring of six phase oscillators governed by Eq. (3.10) with the Hansel-Mato-Meunier coupling (3.5). Parameters are $R = 2$, $\alpha = -1.560$, and $r = -0.1$. Figures show the time evolution of the phase $\theta_j(t) \in [0, 2\pi]$. The frequency of $\theta_2(t)$ and $\theta_5(t)$ clearly differs from that of the others [14].

Weak chimeras are defined by the coexistence of frequency-synchronous and -asynchronous oscillators in coupled identical phase oscillators, but they are not necessarily spatially structured as coherent and incoherent regions, as shown in Fig. 3.12. Ashwin and Burylko analytically proved that weak chimeras in the ring of a few phase oscillators such as $N = 4, 6, 10$ are surely stable for $r \neq 0$ and cannot appear in globally coupled systems.

3.4 Another Chimera State

Chimera states also appear in phase oscillator systems other than the one-dimensional system. As an example of chimeras that can be mathematically analyzed in detail, we review symmetry breaking in interacting populations

of globally coupled phase oscillators [27–29] in this section. For instance, we consider the dynamics of two interacting populations described as

$$\dot{\theta}_j^a(t) = \omega - \sum_{b=1}^{2} \frac{K_{ab}}{N_b} \sum_{k=1}^{N_a} \sin[\theta_j^a(t) - \theta_k^b(t) + \alpha], \tag{3.54}$$

where $N_1 = N_2$, $K_{11} = K_{22} =: \mu > 0$, and $K_{12} = K_{21} =: \nu > 0$. Also, we define $A := \mu - \nu$ and $\beta := \pi/2 - \alpha$. For Eq. (3.54), two populations are identical. However, there appears the chimera state where synchronized ($a = 1$) and desynchronized ($a = 2$) populations coexist, as shown in Fig. 3.13. Then, an initial condition determines which population is synchronized or desynchronized. Eq. (3.54) can be considered as a minimal model of the right and left brains. From this, it have been suggested that there is similarity between such a chimera and unihemispheric sleep of dolphins and other sea mammals [27].

The assumption that chimera states are stationary is not always true. For Eq. (3.54), there appears the breathing chimera state where the global order parameter of a desynchronized population oscillates temporally, as shown in Fig. 3.14. It is shown that this breathing chimera branches via Hopf bifurcation from the stable stationary chimera. When the breathing chimeras were first discovered, Abrams *et al.* [27] posed the question of whether such breathing chimeras exist in the case of one-dimensional arrays.

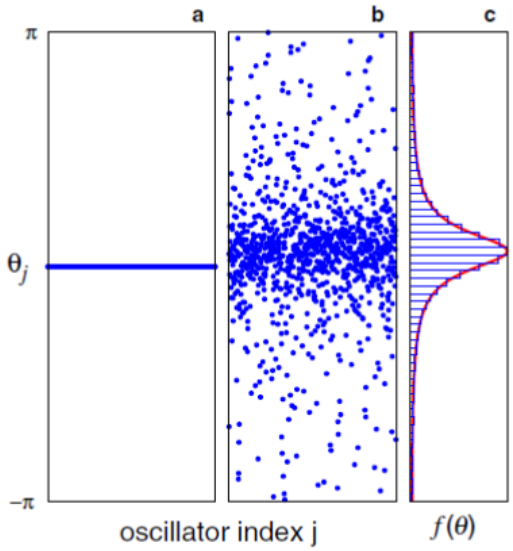

Figure 3.13: Snapshot of a chimera state in two interacting populations described as Eq. (3.54) with $N_1 = N_2 = 1024$, $A = 0.20$, and $\beta = 0.1$. Each figure shows (a) the synchronized population, (b) the desynchronized population, and (c) the density of desynchronized phases [27].

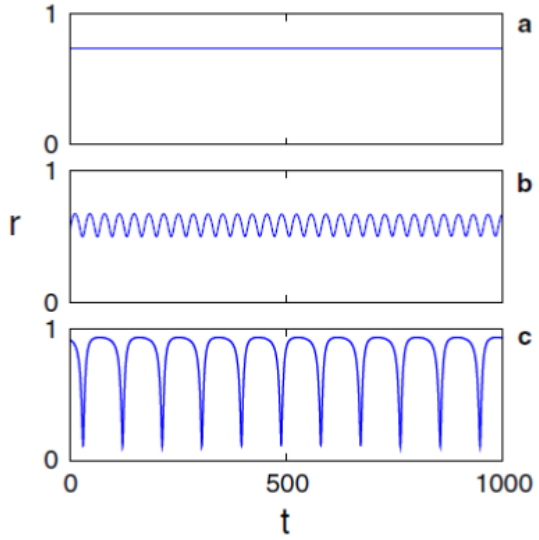

Figure 3.14: Time evolution of the global order parameter of a desynchronized population for Eq. (3.54) with $N_1 = N_2 = 128$ and $\beta = 0.1$. The stationary chimera appears for (a) $A = 0.20$, while the breathing chimeras appear for (b) $A = 0.28$ and (c) $A = 0.35$ [27].

Chapter 4

Persistent Chimera State

When N is finite, chimera states in one-dimensional nonlocally coupled phase oscillators with the sine coupling are chaotic transient and finally collapse into the completely synchronous solution [9,10,42]. Doesn't there exist stable chimera states in finitely discretized systems? In this chapter, we numerically study chimera states by using the coupling function different from the sine coupling and obtain the result that chimera states can be stable even without taking the continuum limit $N \to \infty$, which we call the *persistent chimera state* [16].

4.1 Model

We consider a ring of N identical nonlocally coupled phase oscillators described as

$$\begin{aligned} \dot{\theta}_j(t) &= \omega + \frac{1}{2R} \sum_{k=j-R}^{j+R} \Gamma[\theta_j(t) - \theta_k(t)], \\ \Gamma(\phi) &= -\sin(\phi + \alpha) + r \sin(2\phi), \end{aligned} \tag{4.1}$$

with $j = 1, \cdots, N$. The natural frequency ω is set to zero, and the coupling range R is fixed as $R/N \simeq 0.350$. As the coupling function, we choose the Hansel-Mato-Meunier coupling (3.5) with the phase lag parameter α and the amplitude ratio r [53]. For Eq. (4.1), there appear weak chimeras, which

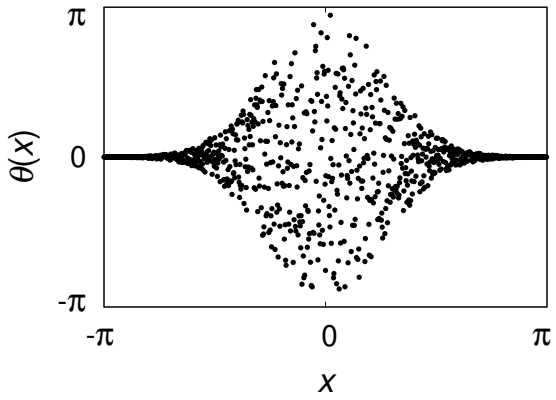

Figure 4.1: Initial condition given as Eq. (4.2) with $N = 1000$.

can be persistent (nontransient) in the system composed of even the minimal number of oscillators [14, 17]. Therefore, we also expect that persistent chimera states excluded by the sine coupling could be observed in this system.

4.2 Stable Solutions in $N \to \infty$

First, we consider stable solutions for sufficiently large N corresponding to the continuum limit. To assist the appearance of chimeras, we use the following initial condition [5], which is so close to a chimera state as shown in Fig. 4.1:

$$\theta_j(0) = 6 \exp\left[-30\left(\frac{j}{N} - \frac{1}{2}\right)^2\right] R_j, \tag{4.2}$$

where $R_j \in [-1/2, 1/2]$ is a uniform random number. Fig. 4.2 shows the results of numerical simulations of Eq. (4.1) for several $r \geq 0$ and fixed $\alpha = 1.460$, where chimera states can be observed in the case of the sine coupling ($r = 0$). In our numerical simulations, chimera states are observed for $r < 0.073$ as shown in Figs. 4.2(a)-(c). The phase pattern (left panels) is clearly separated into coherent and incoherent regions. The right panels show the profiles of the average frequency after the transient time $t_{\rm rel} = 2000$. For $r \geq 0.073$, chimera states gradually disappear with increasing r. Furthermore, chimera states are not observed for $r \geq 0.110$. Then, each

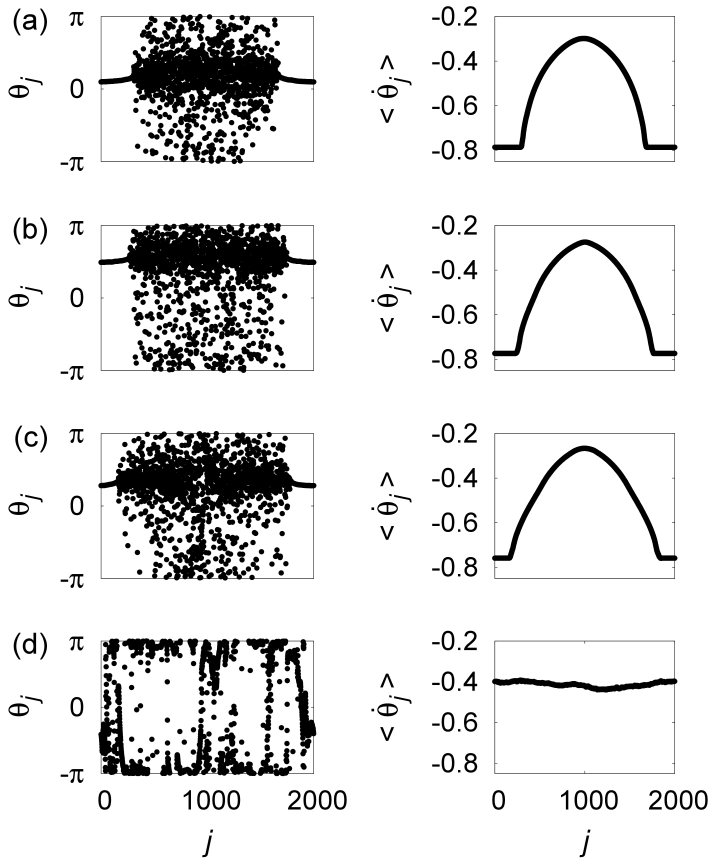

Figure 4.2: Results of numerical simulations of Eq. (4.1) with $N = 2000$ and $\alpha = 1.460$. In each row, the left panel shows the snapshot of phase $\theta_j(t)$, and the right panel shows the profile of the average frequency $\langle \dot{\theta}_j \rangle$ with $T = 5000$. For (a) $r = 0.001$, (b) $r = 0.030$, and (c) $r = 0.060$, chimera states are observed, while they are not observed for (d) $r = 0.120$ [16].

oscillator evolves almost independently, where the average frequency seems to converge on a constant value in $T \to \infty$, though the average frequency in Fig. 4.2(d) still exhibits some fluctuations due to finite T.

For Eq. (4.1), there also appear the completely synchronous solution $\theta_1(t) = \cdots = \theta_N(t) = \Omega t$. By the linear stability analysis, we can obtain the stability region. Letting $\psi_j(t)$ be the small perturbation applied to synchronized oscillator j, the linear evolution equation for $\psi_j(t)$ is obtained as

$$\dot{\psi}_j(t) = \Gamma'(0)\psi_j(t) - \frac{1}{2R}\,\Gamma'(0) \sum_{\substack{k=j-R \\ k\neq j}}^{j+R} \psi_k(t), \tag{4.3}$$

where

$$\Gamma'(\phi) := \frac{d\Gamma(\phi)}{d\phi} = -\cos(\phi+\alpha) + 2r\cos(2\phi). \tag{4.4}$$

Therefore, the Jacobian matrix $\hat{L}$ of Eq. (4.1) for the completely synchronous solution is

$$\hat{L} = \begin{pmatrix} a_0 & a_1 & \cdots & a_{N-2} & a_{N-1} \\ a_{N-1} & a_0 & \cdots & a_{N-3} & a_{N-2} \\ \vdots & & \ddots & & \vdots \\ a_2 & a_3 & \cdots & a_0 & a_1 \\ a_1 & a_2 & \cdots & a_{N-1} & a_0 \end{pmatrix}, \tag{4.5}$$

$$a_n = \begin{cases} \Gamma'(0) & (n=0) \\ -\Gamma'(0)/(2R) & (n=1,\cdots,R,\ N-R,\cdots,N-1) \\ 0 & (\text{otherwise}). \end{cases} \tag{4.6}$$

The matrix (4.5) is a circulant matrix. Because all eigenvalues Λ_l ($l = 0,\cdots,N-1$) of the circulant matrix are calculated as

$$\Lambda_l = \sum_{n=0}^{N-1} e^{i\frac{2\pi}{N}nl}\, a_n, \tag{4.7}$$

we have

$$\Lambda_l = \Gamma'(0)\left\{1 - \frac{1}{R}\sum_{n=1}^{R}\cos\left[\frac{2\pi}{N}nl\right]\right\}. \tag{4.8}$$

Then, we have $\Lambda_0 = 0$, and the sign of $\Lambda_{l\neq 0}$ is identical with that of $\Gamma'(0)$. Therefore, when $\Gamma'(0) < 0$, namely,

$$r < \frac{1}{2}\cos\alpha, \tag{4.9}$$

the completely synchronous solution is stable. For $r < \cos\alpha/2$ ($\simeq 0.055$ at $\alpha = 1.460$), chimera states are also stable, as shown in Figs. 4.2(a)-(b).

As other solutions to Eq. (4.1), we can expect wave solutions

$$\theta_j(t) = \Omega t \pm \frac{2\pi}{N}k(j-1), \tag{4.10}$$

with the wave number $k \in \mathbb{N}$. Fig. 4.3(a) shows the wave solution with $k = 1$. When $k = 0$, Eq. (4.10) is the completely synchronous solution. We can also obtain the stability region of the wave solution for each k. Because the Jacobian matrix $\hat{L}$ for the wave solution is also circulant matrix, we finally obtain eigenvalues as

$$\begin{aligned}\Lambda_l &= \frac{1}{R}\sum_{n=1}^{R}\left[\cos\left(\frac{2\pi}{N}kn\right)\cos\alpha\left\{\cos\left(\frac{2\pi}{N}nl\right)-1\right\}\right. \\ &\quad \pm i\sin\left(\frac{2\pi}{N}kn\right)\sin\alpha\sin\left(\frac{2\pi}{N}nl\right) \\ &\quad \left.-2r\cos\left(\frac{4\pi}{N}kn\right)\left\{\cos\left(\frac{2\pi}{N}nl\right)-1\right\}\right].\end{aligned} \tag{4.11}$$

Then, we have $\Lambda_0 = 0$. Since Λ_l is a complex value, the stability of the wave solution is determined by the sign of the real part of Λ_l. In the present case, the wave solution with $k = 1$ is stable for $r \geq 0.004$ as shown in Fig. 4.3(b), while wave solutions with $k \neq 1$ are unstable in the present parameter region. The survey of the stability regions of stable solutions is depicted in Fig. 4.4.

4.3 Lifetime of Chimera State

We below confirm whether chimera states, particularly for $r > 0$, are transient or really stable even when N is finite. Fig. 4.5 shows the average lifetime

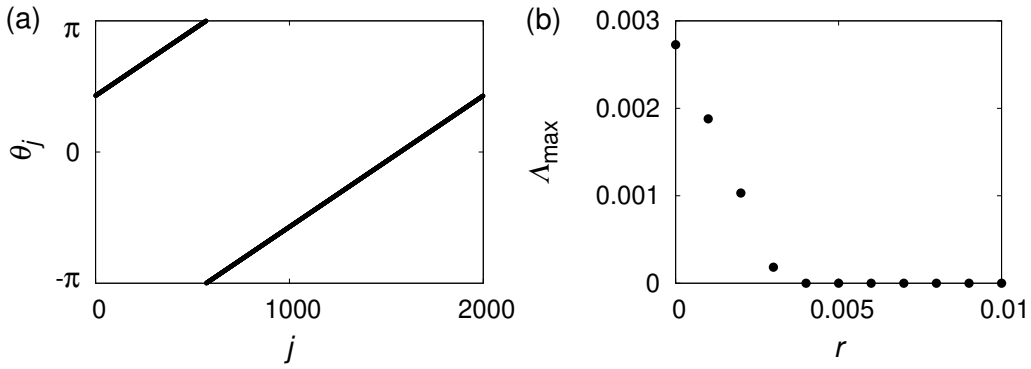

Figure 4.3: (a) Wave solution with the wave number $k = 1$. (b) Maximum value of real parts of eigenvalues Λ_l for the wave solution with $k = 1$ for Eq. (4.1) with $N = 2000$ and $\alpha = 1.460$.

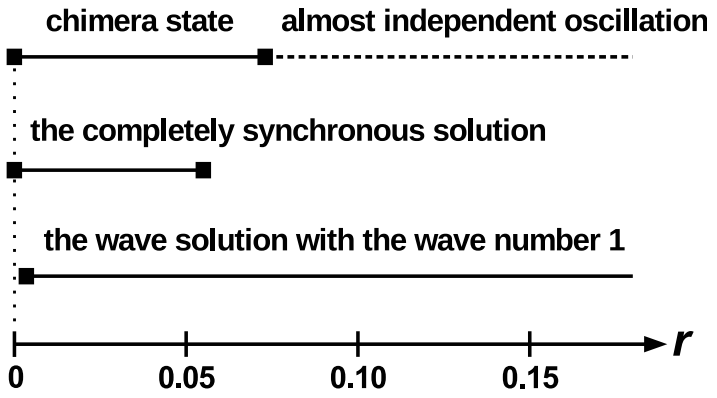

Figure 4.4: Phase diagram of stable solutions to Eq. (4.1) with $\alpha = 1.460$ in the continuum limit ($N = 2000$). Horizontal lines denote the stability regions of each solution. We have not clearly determined the transition between the chimera state and almost independent oscillation yet. Note that the stability region of the wave solution with $k = 1$ does not cover $r = 0$ [16].

τ of chimera states for $N = 30$, as increasing r from 0 to $(\cos\alpha)/2 \simeq 0.055$. Here, we regard the lifetime of the chimera state as the time at which the completely synchronous solution appears, that is, the global order parameter given as Eq. (2.36) reaches $|Z(t)| = 1$. As for the chimera state with small N, we should note that it is difficult to judge the appearance of the chimera state, because the spatial position of the chimera state does not stay still but fluctuates [8], in particular, more violently as N becomes smaller. In fact, for $N = 30$, we could not observe the characteristic profile of the average frequency. However, we observed that the coherent region exists in the phase pattern, which convinces us of the appearance of the chimera state.

In numerical simulations for Fig. 4.5, there is also a possibility that chimera states collapse into a stable solution other than the completely synchronous solution, for instance, the wave solution with $k = 1$. However, we never observed such collapse in our simulations from 1000 different initial conditions given as Eq. (4.2) at each r.

As r is increased, the average lifetime τ increases monotonically and appears to diverge to infinity at some r^*. Assuming some values as r^*, we obtain Fig. 4.6 by the log-log plot of the data $(\Delta r, \tau)$ where $\Delta r := r^* - r$. From this figure, we can assume the power law

$$\tau \propto (\Delta r)^{-\zeta}, \tag{4.12}$$

where ζ is a real exponent, and we determine $r^* \simeq 0.039$ from the best linear fitting of the data. Since $r^* < (\cos\alpha)/2 \simeq 0.055$, the chimera state and the completely synchronous solution are bistable for $r^* < r < (\cos\alpha)/2$ even in the finite N cases. However, we cannot exclude the possibility of $r^* = (\cos\alpha)/2$, because it is difficult to obtain the exact value of r^* due to divergent simulation time.

Next, we study chimera states with $N = 30$ for $r \geq (\cos\alpha)/2$ where the completely synchronous solution is unstable. The possibility that chimera states appear in the region without the stable completely synchronous solution differs from the case of the sine coupling. In this region, chimera states cannot collapse into the completely synchronous solution. Though

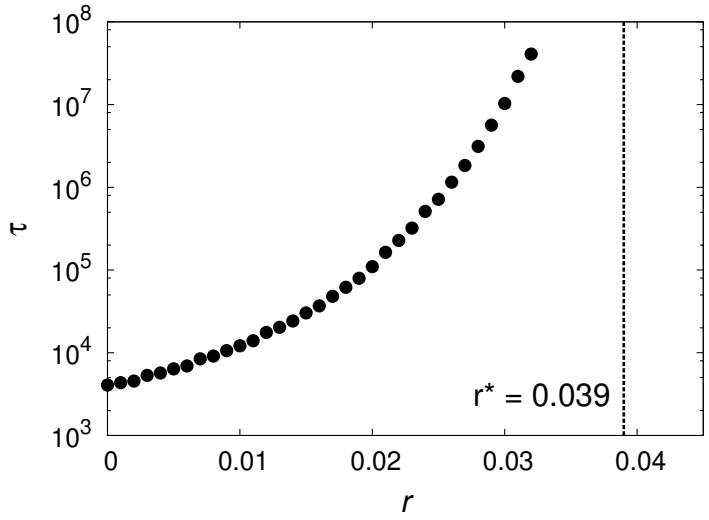

Figure 4.5: Average lifetime τ of chimera states for $N = 30$ and $\alpha = 1.460$. Each point is the average over 1000 simulations from different initial conditions given as Eq. (4.2) [16].

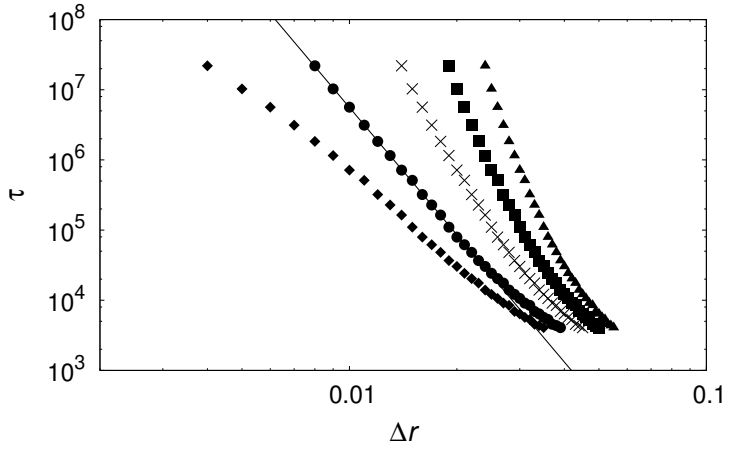

Figure 4.6: Log-log plot of the data $(\Delta r, \tau)$ for $r^* = 0.035$ (diamonds), 0.039 (circles), 0.045 (crosses), 0.050 (squares), and 0.055 (triangles). The data for $r^* = 0.039$ are fitted linearly by the least squares method (black line), where we used only the data $\tau \geq 300000$ to obtain better linearity for this fitting [16].

the wave solution with $k = 1$ is stable in this region, we never observed that chimera states collapse into it within our maximum simulation time $t = 2 \times 10^8$. Therefore, the collapse of the chimera state should not occur if other stable non-chimera solutions do not exist. Though we searched for stable non-chimera solutions other than the wave solution by extensive numerical simulations, we were not able to find any such solutions. From the above results, we conclude that, in a certain range of $r > (\cos\alpha)/2$, the chimera state and the wave solution are bistable, and the chimera state can be persistent even in the finite N cases. This is consistent with $\tau \to \infty$ for $r > r^*$.

Fig. 4.7 shows the stability region of the chimera state. The red region corresponding to stable chimera states in the continuum limit ($N = 2000$) is spread around $r = (\cos\alpha)/2$. In the finite N cases, chimera states for small r become transient, while chimera states for large r remain persistent for $r > (\cos\alpha)/2$ at least. For $\cos\alpha < 0.150$, we can observe that there exists a region $r^* < r < (\cos\alpha)/2$ where chimera states are persistent for $N = 30$. Note that the stability region of the persistent chimera state (hatched in Fig. 4.7) extends to the $r = 0$ line. This means that chimera states with the sine coupling can be also persistent for finite N. Specifically, the average lifetime τ of the chimera state increases similarly to Fig. 4.5 as $\cos\alpha$ is decreased on the $r = 0$ line and diverges at $\cos\alpha^* \simeq 0.044$. However, this result does not contradict the previous work [10] because the parameter α in that work corresponds to the line of black circles ($\alpha = 1.460$) in Fig. 4.7, which has a larger $\cos\alpha$ than our hatched region on the $r = 0$ line.

4.4 Other Chimera States & Weak Chimera

When we studied the collapse of chimera states at $\alpha = 1.460$, we infrequently observed that a chimera state collapses into a weak chimera as shown in Fig. 4.8. In [14], the existence of weak chimeras for Eq. (4.1) is confirmed in the system composed of a small number of oscillators ($N = 4$, 6, and 10). In our numerical simulations with a larger number of oscillators ($N = 30$),

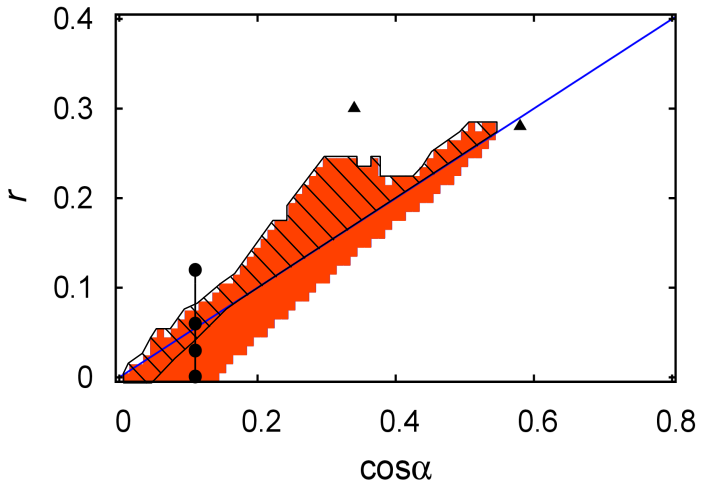

Figure 4.7: Stability region of the chimera state on the $(\cos\alpha, r)$ plane for $N = 2000$ (red region). In the hatched region, there appear the persistent chimera state that is stable for $N = 30$ at least. The blue line denotes $r = (\cos\alpha)/2$, and the completely synchronous solution is stable for $r < (\cos\alpha)/2$. Black circles and triangles denote the parameter values of Fig. 4.2 and Fig. 4.9, respectively [16].

such a weak chimera is stable in a small range of $r < (\cos\alpha)/2$, for instance, $0.032 \leq r \leq 0.040$ at $\alpha = 1.460$.

As other solutions, we observed characteristic chimera states in the continuum limit ($N = 2000$), as shown in Fig. 4.9. Other than the black triangles in Fig. 4.7, we observed such chimeras in a large region of the parameter space. However, we do not describe the region in detail since it is beyond the scope of this thesis.

4.5 Summary of This Chapter

In this chapter, we numerically studied chimera states in nonlocally coupled phase oscillators with the Hansel-Mato-Meunier coupling. In the continuum limit, chimera states appear around $r = (\cos\alpha)/2$. For $r < (\cos\alpha)/2$, the chimera state and the completely synchronous solution can be bistable. In this region of the finite N cases, chimera states are transient for $r < r^*$,

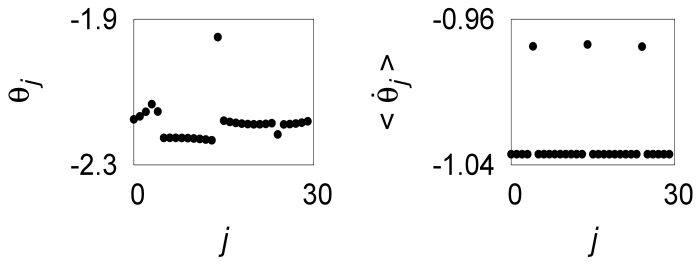

Figure 4.8: Weak chimera for Eq. (4.1) with $N = 30$, $\alpha = 1.460$, and $r = 0.032$, which are the parameter values on the line of black circles in Fig. 4.7. The left figure shows the snapshot of the phase $\theta_j(t)$, and the right figure shows the profile of the average frequency $\langle \dot{\theta}_j \rangle$ [16].

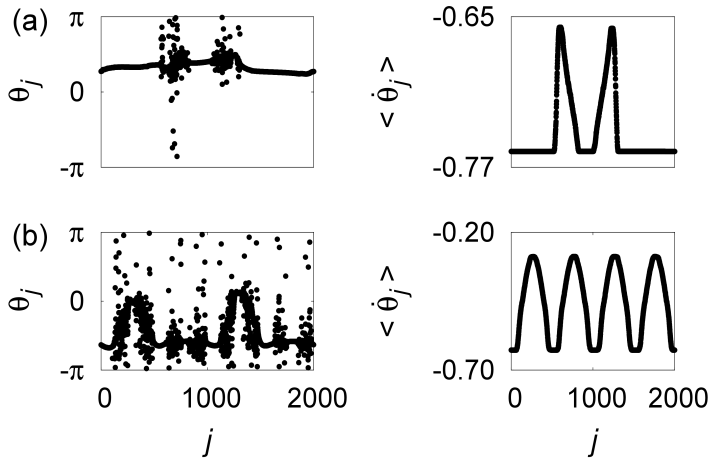

Figure 4.9: Characteristic chimera states for Eq. (4.1) with $N = 2000$. The left figures show the snapshot of phase $\theta_j(t)$, and the right figures show the profile of the average frequency $\langle \dot{\theta}_j \rangle$. Parameters are (a) $\alpha = 0.950$ and $r = 0.280$, and (b) $\alpha = 1.220$ and $r = 0.300$, which are plotted in Fig. 4.7 [16].

while they are persistent for $r^* < r < (\cos\alpha)/2$. Moreover, even for $r > (\cos\alpha)/2$, they are persistent in the region where chimera states are stable in $N \to \infty$. At first, we expected chimera states to become persistent due to the destabilization of the completely synchronous solution by the effect of r. However, the persistent chimera state appears not only in the unstable region of the completely synchronous solution as expected but also in its stable region. As a result, we have discovered that chimera states with the sine coupling can also become persistent by using appropriate α in the stability region of the completely synchronous solution. Though we have numerically found the persistent chimera state, its bifurcation-theoretical understanding is still an open problem.

Chapter 5

Breathing Chimera State

Chimera states in one-dimensional nonlocally coupled phase oscillators in the continuum limit are assumed to be stationary states in most studies [3–6, 11, 13, 18, 19, 21, 23]. This assumption plays an important role in various studies and forms the basis of the analytical theory. However, there is also the question of whether breathing chimeras exist in the one-dimensional system, similarly to two interacting populations of globally coupled phase oscillators [27]. In this chapter, we numerically demonstrate that breathing chimeras can appear even in the one-dimensional system, and we show that the system exhibits a Hopf bifurcation from a stationary chimera to a breathing one [22].

5.1 Model

We consider nonlocally coupled phase oscillators with the sine coupling in $N \to \infty$ described as

$$\begin{aligned} \dot{\theta}(x,t) &= \omega - \int_{-\pi}^{\pi} dy\, G(x-y) \sin[\theta(x,t) - \theta(y,t) + \alpha], \\ G(x) &= \begin{cases} 1/(2\pi s) & (|x| \le \pi s) \\ 0 & (|x| > \pi s), \end{cases} \end{aligned} \tag{5.1}$$

with the phase $\theta(x,t)$ on the space $x \in [-\pi, \pi]$ under the periodic boundary condition. The natural frequency ω is set to zero. The coupling range s satisfies $0 < s \leq 1$. For numerical simulations, we need to discretize x into $x_j := -\pi + 2\pi j/N$ $(j = 0, \cdots, N-1)$. Then, Eq. (5.1) is rewritten as

$$\dot{\theta}_j(t) = \omega - \frac{1}{2R} \sum_{k=j-R}^{j+R} \sin[\theta_j(t) - \theta_k(t) + \alpha], \tag{5.2}$$

where $\theta_j(t) = \theta(x_j, t)$ and $R = sN/2$.

To answer the question posed by Abrams *et al.* [27], Laing [7] demonstrated that there also appear breathing chimeras in the one-dimensional system by introducing phase lag parameter heterogeneity $\alpha = \alpha_0 + \alpha_1 \cos x$, but phase oscillators are not identical in this system. After that, Bolotov *et al.* [19, 21] numerically confirmed that similar breathing chimeras appear in the system composed of identical phase oscillators with improved heterogeneity $\alpha = \alpha_0 + \alpha_1 |Y(x,t)|^2$. However, we do not use such heterogeneity.

5.2 Numerical Simulation

We focus on the multichimera state with two coherent and incoherent regions, as shown in Fig. 5.1. When we use the word "multichimera" below, it basically means such a multichimera state. To assist the appearance of multichimeras for numerical simulations, we use the following initial condition

$$\theta(x) = \begin{cases} \exp\left[-30\left(\dfrac{|x|}{2\pi} - \dfrac{1}{4}\right)^2\right] p(x) & \left(0 \leq |x| < \dfrac{\pi}{2}\right) \\ \exp\left[-30\left(\dfrac{|x|}{2\pi} - \dfrac{1}{4}\right)^2\right] p(x) + \pi & \left(\dfrac{\pi}{2} \leq |x| < \pi\right), \end{cases} \tag{5.3}$$

where $p(x) \in [-\pi, \pi]$ is a uniform random number. As shown in Fig. 5.2, this initial condition is close to a multichimera. Fig. 5.3 shows the stability region of the multichimera obtained by the numerical simulation of Eq. (5.1) with

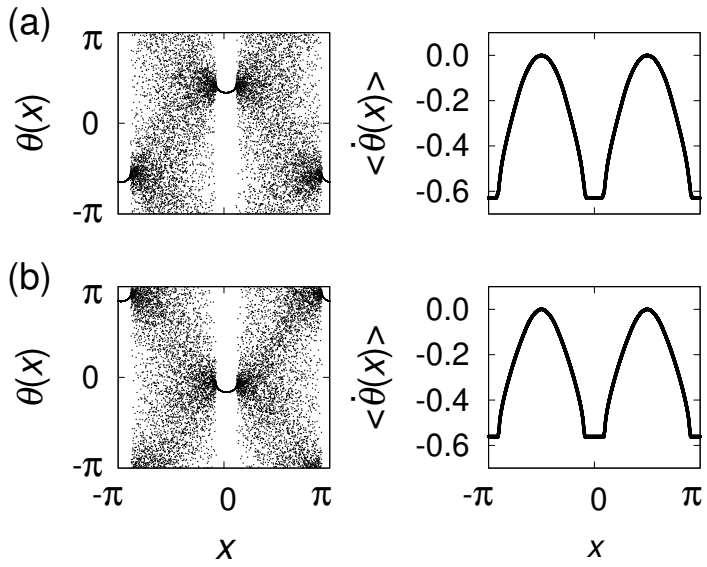

Figure 5.1: Multichimera state with two coherent and incoherent regions for Eq. (5.1) with $N = 100000$ and $\alpha = 1.480$. In each row, the left panel shows the snapshot of the phase $\theta(x,t)$, and the right panel shows the profile of the average frequency $\langle\dot{\theta}(x)\rangle$ with $T = 2000$. (a) The breathing multichimera appears for $s = 0.360$, while (b) the stationary multichimera appears for $s = 0.440$. All figures are plotted once every 10 oscillators.

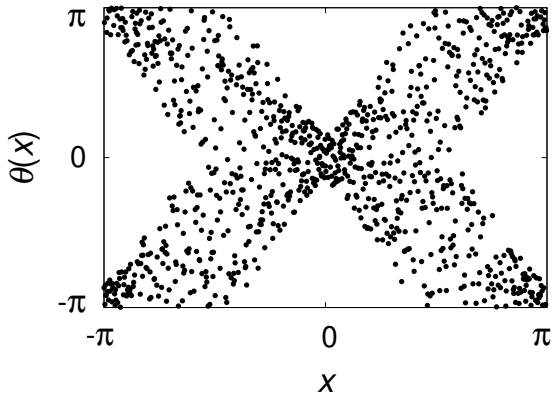

Figure 5.2: Initial condition given as Eq. (5.3) with $N = 1000$.

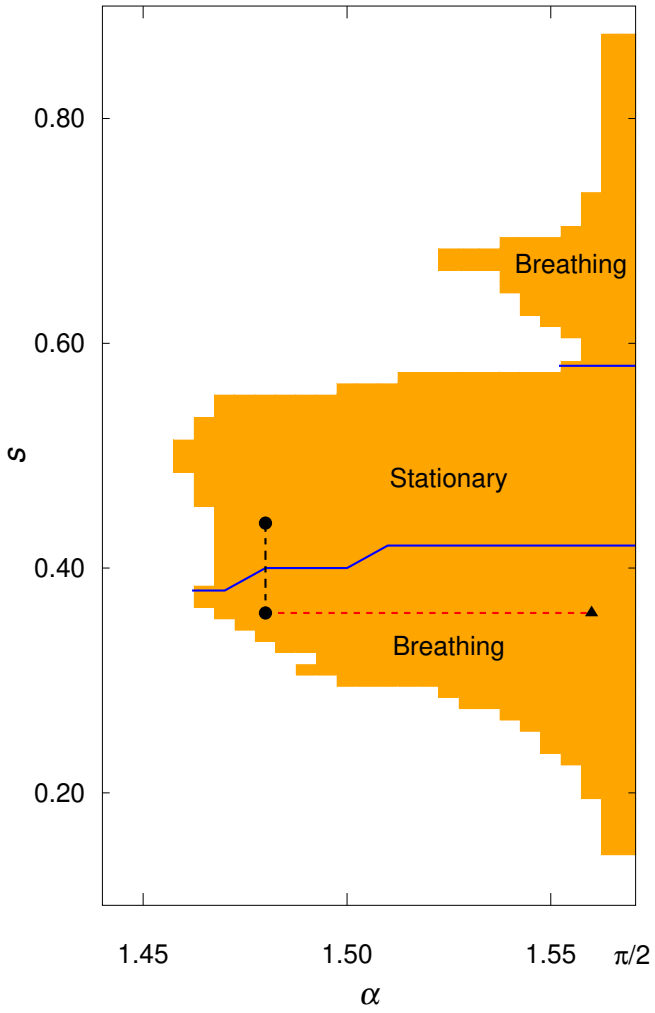

Figure 5.3: Stability region of the multichimera for Eq. (5.1) obtained by the numerical simulation with $N = 100000$. Black circles denote the parameter values of Fig. 5.1. The blue line denotes the Hopf bifurcation points obtained by the linear stability analysis for the stationary multichimera with fixed α in Section 5.4.1.

$N = 100000$. This result is consistent with the phase diagram in [12] as far as the stability region of the multichimera is concerned. However, in [12], the stationary and breathing multichimeras are not distinguished, and the region of the breathing one is identified as a part of the region of the stationary one.

It is mostly assumed that the chimera state for Eq. (5.1) is a stationary state in the rotating frame with a frequency Ω. This precisely means that the local order parameter

$$z(x,t) := \lim_{\epsilon \to 0+} \frac{1}{2\epsilon} \int_{x-\epsilon}^{x+\epsilon} dy\, e^{i\theta(y,t)}, \tag{5.4}$$

and the local mean field

$$Y(x,t) = \int_{-\pi}^{\pi} dy\, G(x-y)\, e^{i\theta(y,t)}, \tag{5.5}$$

take the form $z(x,t) = z_{\rm st}(x)\, e^{i\Omega t}$ and $Y(x,t) = Y_{\rm st}(x)\, e^{i\Omega t}$, respectively. Then, the global order parameter

$$Z(t) = \frac{1}{2\pi} \int_{-\pi}^{\pi} dy\, e^{i\theta(y,t)}, \tag{5.6}$$

also takes the form $Z(t) = Z_{\rm st}\, e^{i\Omega t}$ with $Z_{\rm st} \in \mathbb{C}$, so $|Z(t)|$ is independent of time. In the case of stationary multichimeras, $|Z(t)|$ should vanish in $N \to \infty$, but we found that $|Z(t)|$ can oscillate periodically at appropriate parameters (α, s) and sufficiently large N. Fig. 5.4 shows the time evolution of $|Z(t)|$ for multichimeras in Fig. 5.1. The blue solid line ($s = 0.360$) exhibits a clear periodic oscillation, while the orange dashed line ($s = 0.440$) merely exhibits a small fluctuation around zero. We call the former state the breathing multichimera and regard the latter as the stationary multichimera. We can distinguish between stationary and breathing multichimeras by observing the time evolution of $|Z(t)|$, but that is difficult for small N because large fluctuation in $|Z(t)|$ is unavoidable as shown in Fig. 5.5. To distinguish between these clearly, we needed 10000 oscillators at least in our numerical simulation.

The detailed periodic behavior of the breathing multichimera can be con-

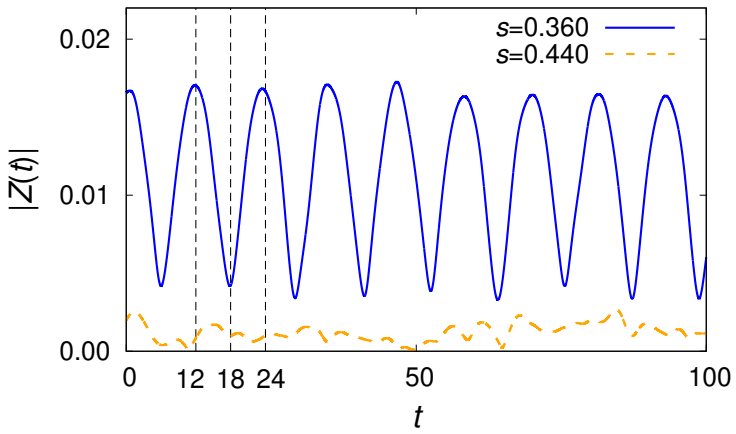

Figure 5.4: Time evolution of the global order parameter $|Z(t)|$ for multichimeras in Fig. 5.1. The multichimera is breathing for $s = 0.360$ (blue solid line), while it is stationary for $s = 0.440$ (orange dashed line). Vertical dashed lines correspond to the times t in Fig. 5.6 [22].

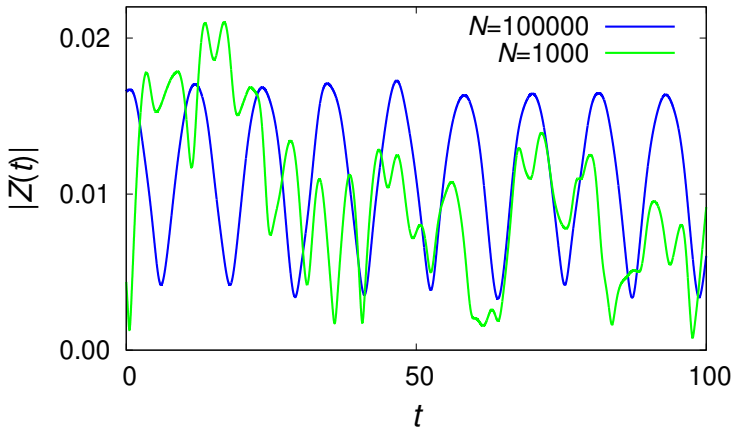

Figure 5.5: Time evolution of the global order parameter $|Z(t)|$ for multichimeras with $\alpha = 1.480$ and $s = 0.360$. When $N = 1000$ (green line), it is difficult to distinguish whether or not the multichimera is breathing. The blue line is the same as that in Fig. 5.4.

firmed as the periodic oscillation of $|Y(x,t)|$ as shown in Fig. 5.6. $|Y(x,t)|$ takes a bimodal form, where the positions of the peaks correspond to each center of the coherent regions. Within a period of $|Z(t)|$ approximately corresponding to $t = 12 \sim 24$ in Fig. 5.4, $|Y(x,t)|$ experiences the variation in one-half of its period, and within the next period of $|Z(t)|$, $|Y(x,t)|$ completes its whole period. In the simulation of Fig. 5.6, the angular frequency of $|Y(x,t)|$ is calculated as about 0.270.

Thus, breathing chimera states also exist in the one-dimensional system without introducing phase lag parameter heterogeneity [7, 19, 21]. In this chapter, we focus on the breathing multichimera and study the bifurcation mechanism from the stationary multichimera by the linear stability analysis for the stationary multichimera.

5.3 Stationary Multichimera

Before the linear stability analysis for the stationary multichimera, we need to obtain the numerical solution to the self-consistency equation for $Y_{\rm st}(x)$

$$Y_{\rm st}(x) = ie^{-i\alpha} \int_{-\pi}^{\pi} dy\, G(x-y)\, Y_{\rm st}(y)\, h(y), \tag{5.7}$$

$$h(x) = \begin{cases} [\Delta - \sqrt{\Delta^2 - |Y_{\rm st}(x)|^2})/|Y_{\rm st}(x)|^2] & [\Delta > |Y_{\rm st}(x)|] \\ [\Delta - i\sqrt{|Y_{\rm st}(x)|^2 - \Delta^2})/|Y_{\rm st}(x)|^2] & [\Delta \leq |Y_{\rm st}(x)|], \end{cases} \tag{5.8}$$

with the step kernel. At first, We tried to numerically solve Eq. (5.7) with the step kernel by iteration procedure mentioned in Sec. 3.2.2. However, we were not able to obtain the stationary solution $Y_{\rm st}(x)$ of the multichimera because $Y_{\rm st}(x)$ converged on another solution corresponding to a standard chimera state with one coherent and one incoherent region, under any initial conditions. Since where the iteration converges is attributed to the property of the iteration procedure, this does not mean that the stationary multichimera solution does not exist in this system. To solve this problem, we try to obtain the corresponding solution by using another coupling kernel,

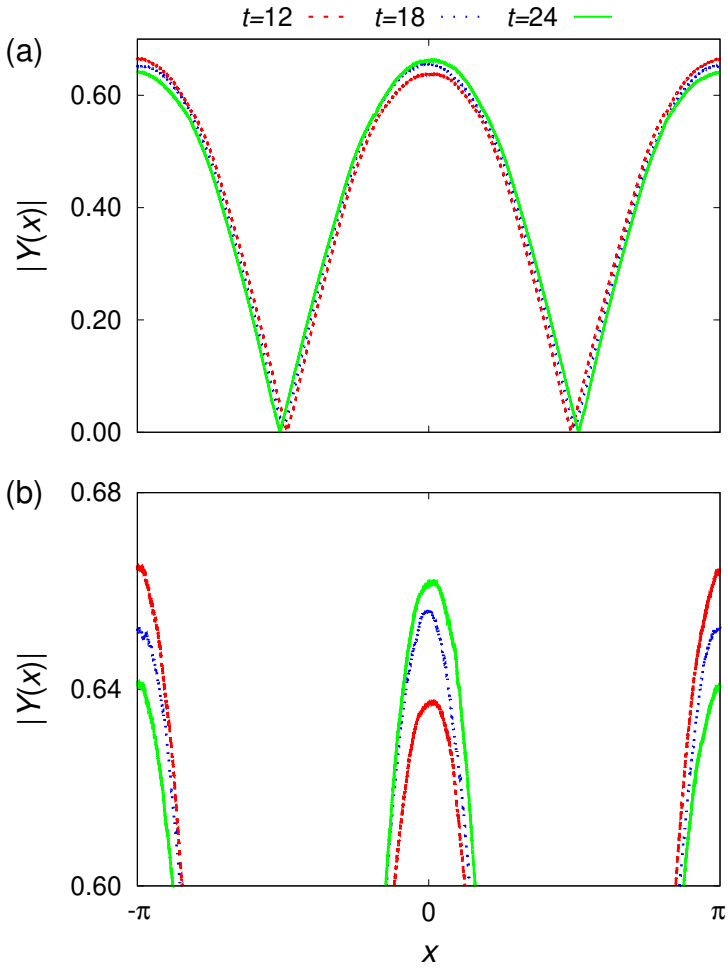

Figure 5.6: Snapshot of the local mean field $|Y(x,t)|$ for the breathing multichimera in Fig. 5.1. (a) The global view of the snapshot; (b) the upper enlarged view. The red dashed line ($t = 12$) and green solid line ($t = 24$) approximately correspond to peaks of $|Z(t)|$, while the blue dotted line ($t = 18$) approximately corresponds to a valley, as shown in Fig. 5.4 [22].

instead of the step kernel.

The coupling kernel $G(x)$ is generally an even real function of $x \in [-\pi, \pi)$ described as

$$G(x) = \sum_{k=0}^{\infty} g_k \cos(kx), \tag{5.9}$$

with $g_k \in \mathbb{R}$. According to [11], it is analytically proved that multichimeras exist under the condition $g_1 \neq 0$, and the local mean field $Y_{\rm st}(x)$ of a stationary multichimera is given by an even function

$$Y_{\rm st}(x) = \sum_{m=1}^{\infty} C_{2m-1} \cos[(2m-1)x], \tag{5.10}$$

with $C_{2m-1} \in \mathbb{C}$. This means that all multichimera solutions to Eq. (5.7) can be transformed into the form (5.10) by the appropriate spatial translation. Using Eq. (5.10), $h(x)$ turns out to be an even function because $|Y_{\rm st}(x)|$ is also even. Let a set of $\tilde{Y}(x)$ satisfying Eq. (5.10) and Δ be a solution to Eq. (5.7). Substituting Eq. (5.9) and Eq. (5.10) into Eq. (5.7) and eliminating the terms whose integrands are odd functions of y, we have

$$\begin{aligned} Y_{\rm st}(x) &= ie^{-i\alpha} \sum_{k=0}^{\infty} g_k \sum_{m=1}^{\infty} C_{2m-1} \\ &\quad \times \int_{-\pi}^{\pi} dy \cos[k(x-y)] \cos[(2m-1)y]\, h(y) \\ &= 2ie^{-i\alpha} \sum_{k=0}^{\infty} g_k \cos(kx) \sum_{m=1}^{\infty} C_{2m-1} \\ &\quad \times \int_{0}^{\pi} dy \cos(ky) \cos[(2m-1)y]\, h(y). \end{aligned} \tag{5.11}$$

Moreover, changing the variable as $y' = y - \pi/2$ in the integration in Eq. (5.11), it becomes

$$\begin{aligned} Y_{\rm st}(x) &= 2ie^{-i\alpha} \sum_{k=0}^{\infty} g_k \cos(kx) \sum_{m=1}^{\infty} C_{2m-1} \\ &\times \int_{-\frac{\pi}{2}}^{\frac{\pi}{2}} dy' \cos\left[k\left(y'+\frac{\pi}{2}\right)\right] \cos\left[(2m-1)\left(y'+\frac{\pi}{2}\right)\right] h\left(y'+\frac{\pi}{2}\right). \end{aligned} \tag{5.12}$$

Since the function $h(y'+\pi/2)$ in the integrand is an even function of y' too, we again eliminate the terms whose integrands are odd functions of y', and we have

$$\begin{aligned} Y_{\rm st}(x) &= 2ie^{-i\alpha}\sum_{l=1}^{\infty} g_{2l-1}\cos[(2l-1)x]\sum_{m=1}^{\infty} C_{2m-1}(-1)^{l+m} \\ &\quad\times\int_{-\frac{\pi}{2}}^{\frac{\pi}{2}} dy'\sin[(2l-1)y']\sin[(2m-1)y']\,h\left(y'+\frac{\pi}{2}\right). \quad (5.13) \end{aligned}$$

From the above, for $Y_{\rm st}(x)$ and Δ of a stationary multichimera satisfying Eq. (5.7), we can finally obtain

$$Y_{\rm st}(x) = ie^{-i\alpha}\sum_{l=1}^{\infty} g_{2l-1}\sum_{m=1}^{\infty} C_{2m-1}A_{lm}\cos[(2l-1)x], \quad (5.14)$$

where A_{lm} is a complex constant. Eq. (5.14) shows that $Y_{\rm st}(x)$ and Δ of a stationary multichimera depends only on the odd harmonic coefficients g_{2m-1}, not on the even harmonic coefficients g_{2m} of the coupling kernel $G(x)$. This is because we recover Eq. (5.14) even when we substitute the identical set of $Y_{\rm st}(x)$ and Δ into Eq. (5.7) with another coupling kernel, for instance,

$$G_{\rm odd}(x) = \sum_{m=1}^{\infty} g_{2m-1}\cos[(2m-1)x], \quad (5.15)$$

with the same set of odd harmonic coefficients g_{2m-1}. Therefore, each stationary multichimera for $G(x)$ and $G_{\rm odd}(x)$ systems has an identical local mean field. This does not mean that the stability properties of these multichimeras are also identical. However, Eq. (5.7) for each system have an identical stationary multichimera solution, whether or not each multichimera is stable. It is expected that for Eq. (5.7) with $G_{\rm odd}(x)$, $Y_{\rm st}(x)$ converges on the stationary multichimera solution by the iteration procedure because it dose not have the standard chimera solution due to $g_0 = 0$ [11]. In fact, the coupling kernel $G_{\rm odd}(x)$ corresponding to the step kernel is useful for obtaining the numerical solution of the stationary multichimera.

To confirm the above property, we perform a numerical simulation using

a new coupling kernel $G_{\rm odd}(x)$ with the same set of odd harmonic coefficients g_{2m-1} of the step kernel $G(x)$. The coefficients g_k of the step kernel are given as

$$g_k = \begin{cases} 1/(2\pi) & (k=0) \\ \sin(\pi kr)/(\pi^2 kr) & (k \neq 0), \end{cases} \tag{5.16}$$

but an infinite number of coefficients are required to make $G_{\rm odd}(x)$. Instead of these coefficients, we use

$$G_{\rm odd}(x) = [G(x) - G(x-\pi)]/2, \tag{5.17}$$

in our numerical simulation. For this $G_{\rm odd}(x)$, we also observed stationary multichimeras. Fig. 5.7 shows the time-averaged local mean fields $\langle Y_{\rm st}(x)\rangle$ of the stationary multichimeras using the step kernel $G(x)$ and the corresponding $G_{\rm odd}(x)$. They are clearly identical and also agree with the numerical solution $Y_{\rm st}(x)$ to the self-consistency equation (5.7) with $G_{\rm odd}(x)$. Here, we have chosen the additional condition

$$\Theta(-\pi) = -\frac{\pi}{2}, \tag{5.18}$$

for solving the self-consistency equation, instead of Eq. (3.31). From this result, when we perform the linear stability analysis for the stationary multichimera, we can use the local order parameter $z_{\rm st}(x)$ computed from the numerical solution to Eq. (5.7) with the corresponding $G_{\rm odd}(x)$, instead of the step kernel $G(x)$. The local order parameter of the stationary multichimera can be obtained by

$$z_{\rm st}(x) = ie^{-i\alpha} Y_{\rm st}(x)\, h(x), \tag{5.19}$$

as shown in Fig. 5.8.

Multichimeras can also appear for the other $G_{\rm odd}(x)$ system, e.g., $G_{\rm odd}(x) = \cos x$ [13], $G_{\rm odd}(x) = g_1 \cos x + g_3 \cos 3x$ as shown in Fig. 5.9, and so on. In our numerical simulations for various $G_{\rm odd}(x)$ systems, we found an interesting property common to multichimeras for $G_{\rm odd}(x)$, which is an exact

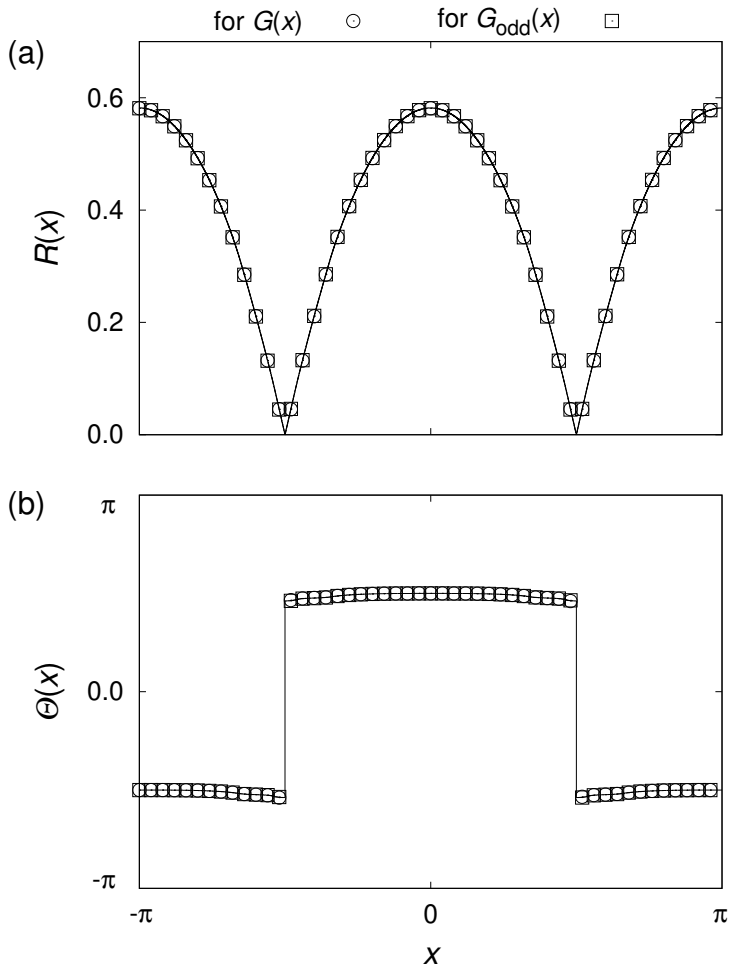

Figure 5.7: Local mean field $Y_{\rm st}(x)$ of the stationary multichimera corresponding to Fig. 5.1. (a) The amplitude $R(x)$; (b) the argument $\Theta(x)$. Open circles denote the time-averaged local mean field $\langle Y_{\rm st}(x)\rangle$ for the step kernel $G(x)$, and open squares denote $\langle Y_{\rm st}(x)\rangle$ for $G_{\rm odd}(x)$ with the same parameters. Note that those are plotted once every 2000 oscillators. The solid line denotes the numerical solution $Y_{\rm st}(x)$ to the self-consistency equations (5.7) with $G_{\rm odd}(x)$ [22].

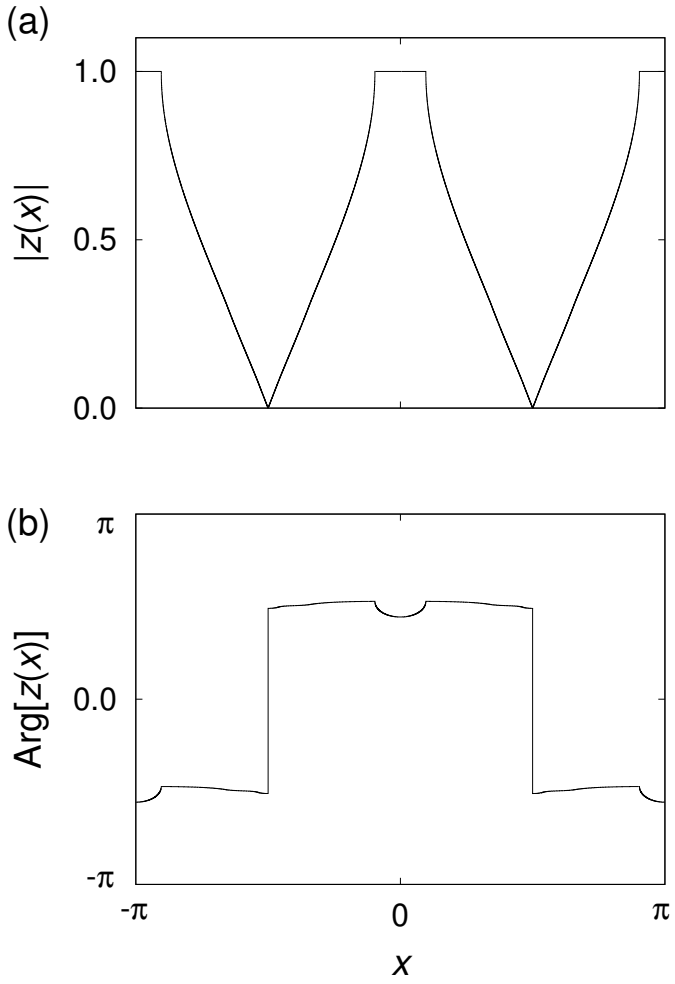

Figure 5.8: Local order parameter $z_{\rm st}(x)$ of the stationary multichimera. (a) The amplitude $|z_{\rm st}(x)|$; (b) the argument of $z(x,t)$. These figures are obtained by Eq. (5.19) from the numerical solutions $Y_{\rm st}(x)$ and Δ corresponding to Fig. 5.7.

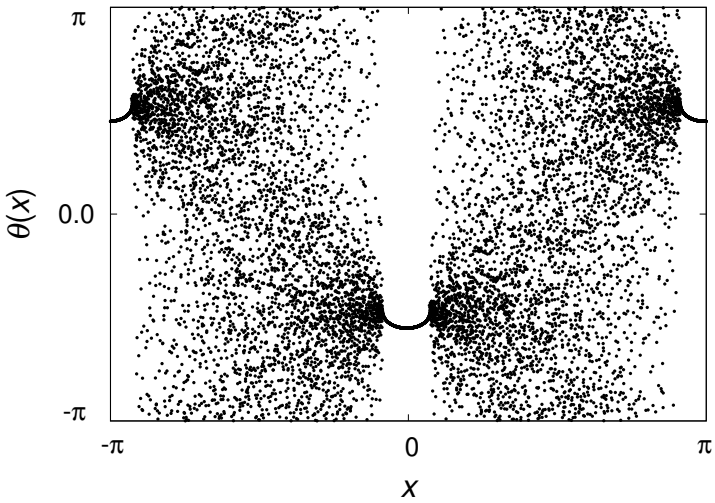

Figure 5.9: Snapshot of a multichimera for $G_{\rm odd}(x) = g_1 \cos x + g_3 \cos 3x$ with $N = 10000$, $\alpha = 1.500$, $g_1 = 1$, and $g_3 = -0.0916$. The phase $\theta(x,t)$ on any point x satisfies Eq. (5.20) [22].

relationship between the phase $\theta(x,t)$ as

$$|\theta(x,t) - \theta(x-\pi,t)| = \pi, \tag{5.20}$$

on any point x. In fact, for any $G_{\rm odd}(x)$, we obtain $\dot{\theta}(x,t) - \dot{\theta}(x-\pi,t) = 0$ under Eq. (5.20) from rewritten phase equation

$$\dot{\theta}(x,t) = \omega - {\rm Im}[e^{i\alpha} e^{i\theta(x,t)} Y^*(x,t)], \tag{5.21}$$

because the relation $Y(x,t) = -Y(x-\pi,t)$ is satisfied at any time. This means that Eq. (5.20) can be a solution to Eq. (5.21) with $G_{\rm odd}(x)$ whether stable or not, but our simulations show that the system with $G_{\rm odd}(x)$ always converges on the solution satisfying Eq. (5.20) under any initial conditions. For the kernel other than $G_{\rm odd}(x)$, this property is not exact, but seems to be satisfied only in the meaning of average, as seen in Fig. 5.1. Under Eq. (5.20), the global order parameter $|Z(t)|$ exactly vanishes, and the oscillation of the local mean field $|Y(x,t)|$, as shown in Fig. 5.6, cannot appear. Therefore, the appearance of breathing multichimeras is forbidden in the $G_{\rm odd}(x)$ systems.

5.4 Breathing Multichimera

It is known that the breathing chimeras in the other studies [7, 19, 21, 27] branch via Hopf bifurcation from stable stationary chimeras. If the present breathing multichimera also branches via Hopf bifurcation, an unstable stationary multichimera should exist in the neighborhood of the bifurcation point. The local mean field of this unstable stationary multichimera should be a solution to the self-consistency equation (5.7) and identical with that of the stationary multichimera for the $G_{\rm odd}(x)$ system.

5.4.1 Hopf bifurcation

A Hopf bifurcation, where a fixed point loses stability and a limit cycle appears around the unstable fixed point, is caused by a pair of complex conjugate eigenvalues of the Jacobian matrix which crosses the imaginary axis on the complex plane. As mentioned in Sec. 3.3.1, the linear stability of the stationary chimera is determined by the eigenvalues of the matrix $\hat{L}$ such that $\dot{\boldsymbol{v}} = \hat{L}\,\boldsymbol{v}$ with $\boldsymbol{v}(x,t) = [\mathrm{Re}\, v(x,t),\, \mathrm{Im}\, v(x,t)]^T$ where the small perturbation $v(x,t)$ governed by

$$\begin{aligned} \dot{v}(x,t) &= g(x) z_{\rm st}(x) + \frac{1}{2} e^{-i\alpha} V(x,t) - \frac{1}{2} e^{i\alpha} z_{\rm st}^2(x) V^*(x,t), \\ V(x,t) &= \int_{-\pi}^{\pi} dy\, G(x-y) v(y,t), \end{aligned} \tag{5.22}$$

where

$$g(x) = \begin{cases} i\sqrt{\Delta^2 - |Y_{\rm st}(x)|^2} & [\Delta > |Y_{\rm st}(x)|] \\ -\sqrt{|Y_{\rm st}(x)|^2 - \Delta^2} & [\Delta \le |Y_{\rm st}(x)|]. \end{cases} \tag{5.23}$$

The eigenvalues of $\hat{L}$ consist of the essential spectrum and the point spectrum, but the stability of the stationary chimera is determined only by the point spectrum [11, 13, 23].

Since the step kernel $G(x)$ has infinite numbers of nonzero g_k, we cannot the method for obtaining the point spectrum in [11, 13]. Therefore, we discretize the space coordinate $x \to x_j = -\pi + 2\pi j/M$ $(j = 0, \cdots, M-1)$ and

compute all eigenvalues λ by solving the eigenvalue problem of $2M \times 2M$ matrix L_d such that $\dot{\boldsymbol{v}}_d = L_d \boldsymbol{v}_d$ with $\boldsymbol{v}_d(t) = [\cdots, \mathrm{Re}\, v(x_j, t), \mathrm{Im}\, v(x_j, t), \cdots]^T$. Then, we use $Y_{\mathrm{st}}(x)$ and Δ satisfying Eq. (5.7) with the corresponding $G_{\mathrm{odd}}(x)$, instead of $G(x)$. Note that we insert the original kernel $G(x)$ into Eq. (5.22) to solve the eigenvalue problem, though $G_{\mathrm{odd}}(x)$ is used for computing $Y_{\mathrm{st}}(x)$ and Δ. Fig. 5.10(a) shows all the eigenvalues λ of L_d with $M = 5000$, $\alpha = 1.480$, and $s = 0.360$ on the complex plane. As seen from this figure, we have some eigenvalues with positive real part because the stationary multichimera is unstable and changes into a breathing one at these parameters. We can regard those eigenvalues as roughly separating into two groups. Group 1 consists of some eigenvalues around the real axis, and group 2 consists of others around the imaginary values about 0.270 and their complex conjugate, as shown in Fig. 5.10(c).

Even though we can observe the eigenvalues with a positive real part, we cannot easily tell whether they belong to the point spectrum or a fluctuation of the essential spectrum caused by finite discretization. If an eigenvalue with a positive real part belongs to such a fluctuation, its real part should go to zero in $M \to \infty$, while an eigenvalue in the point spectrum keeps the positive real part in that limit. We computed the eigenvalues of L_d with various M and found their limiting behaviors as M is increased, as shown in Fig. 5.11. From this figure, we can see that the maximum value of the real parts of the eigenvalues in group 1 tends to go to zero, while that value in group 2 converges to a positive constant. Therefore, it turns out that at least a pair of the complex conjugate eigenvalues in group 2 belongs to the point spectrum, while the eigenvalues in group 1 belong to the fluctuation of the essential spectrum. At the other parameters where the stationary multichimera is stable, the point spectrum contains only the eigenvalues with a negative real part, as shown in Fig. 5.10(b).

Fig. 5.12 shows that a Hopf bifurcation from a stationary multichimera to a breathing one occurs for $\alpha = 1.480$, denoted by the black dashed line in Fig. 5.3. The Hopf bifurcation points for $\alpha = 1.480$ and other values are shown as the blue line in Fig. 5.3. Note that the absolute values of the imaginary parts of the point spectrum, as shown in Fig. 5.10(a), are nearly

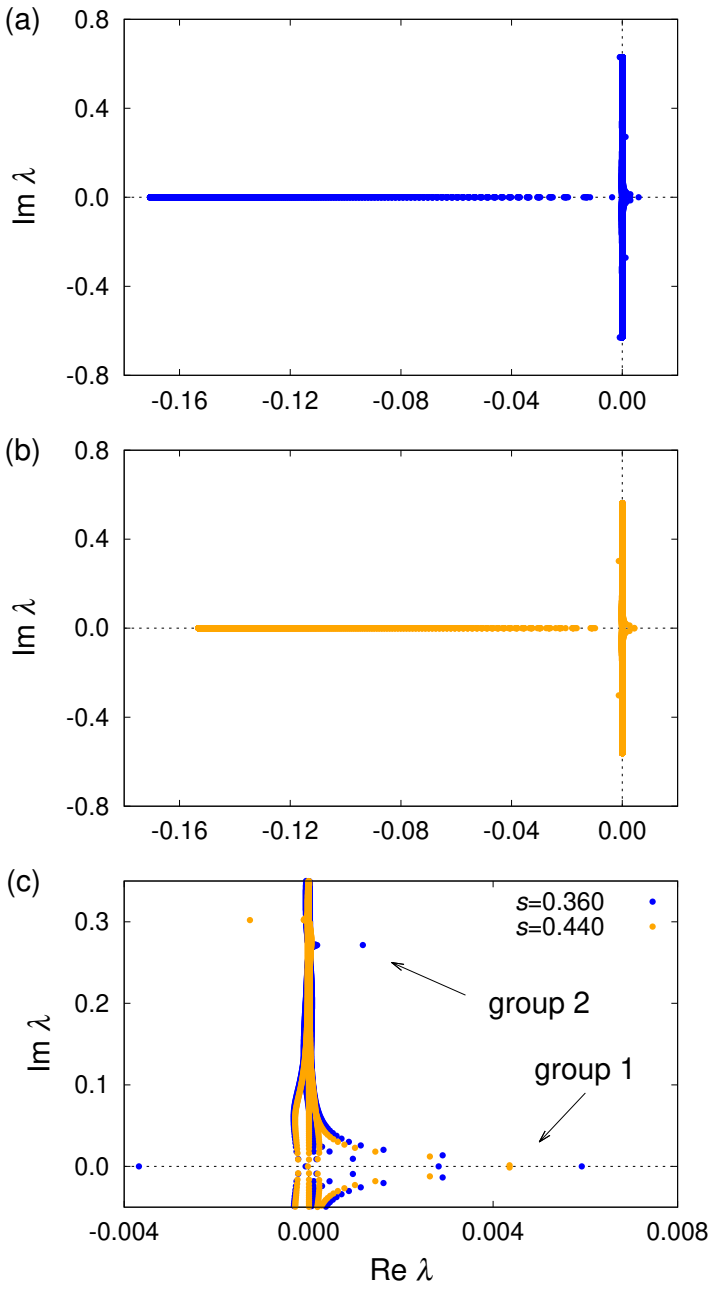

Figure 5.10: Complex eigenvalues λ of L_d with $M = 5000$ and $\alpha = 1.480$ using $Y_{\rm st}(x)$ with $N = 200000$. (a) All eigenvalues for the unstable stationary multichimera that changes to a breathing one ($s = 0.360$); (b) those for the stable stationary multichimera ($s = 0.440$). (c) The enlarged view of (a) and (b) denoted by the blue and orange points, respectively. The dashed lines in each panel are drawn only for reference [22].

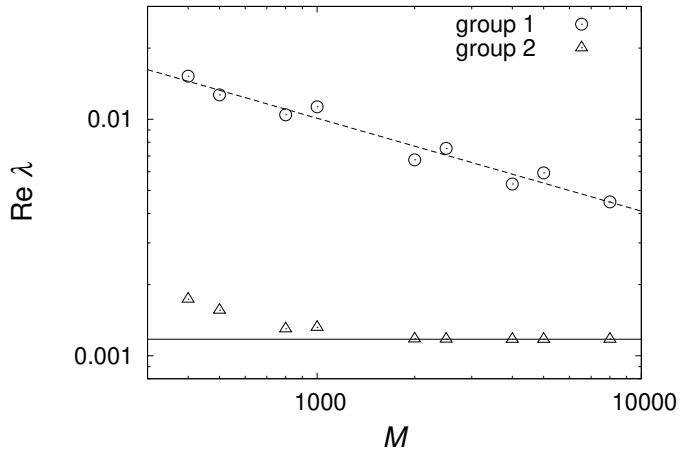

Figure 5.11: Transition of the positive real parts of the eigenvalues of L_d for an unstable stationary multichimera ($\alpha = 1.480$ and $s = 0.360$) with increasing M. Circles denote the maximum values of the real parts of the eigenvalues in group 1, and triangles denote those in group 2. The data for group 1 are fitted linearly (dashed line) in the log-log plot and go to zero with increasing M. In contrast, the data for group 2 converge to a positive constant 1.175×10^{-3} (solid line) [22].

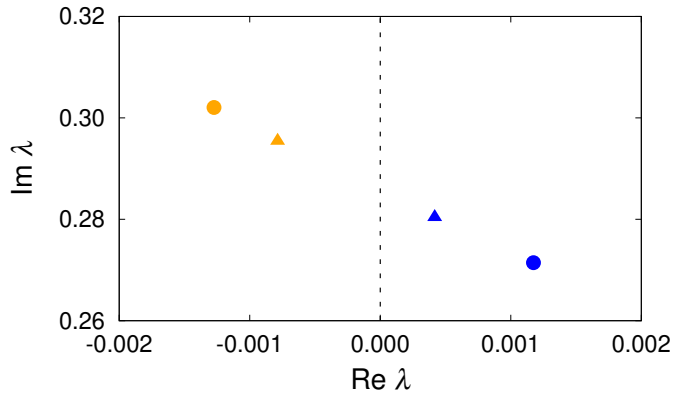

Figure 5.12: Hopf bifurcation for fixed $\alpha = 1.480$. Each point shows the point spectrum with the positive imaginary part for $s = 0.440$ (orange circle), $s = 0.420$ (orange triangle), $s = 0.380$ (blue triangle), and $s = 0.360$ (blue circle), and corresponds to the black dashed line in Fig. 5.3. The point for $s = 0.400$, that is very close to the Hopf bifurcation point, is omitted because we could not distinguish the point spectrum from other eigenvalues. The dashed line is the imaginary axis [22].

equal to the angular frequency of the local mean field $|Y(x,t)|$, as shown in Fig. 5.6, which is calculated to be about 0.270. This result agrees with the occurrence of a supercritical Hopf bifurcation [1].

5.4.2 Non-standard Hopf bifurcation

Next, we compare breathing multichimeras for fixed $s = 0.360$, denoted by the red dashed line in Fig. 5.3. In our numerical calculation, we found that the positive real parts of the point spectrum tend to go to zero as α is increased toward $\alpha = \pi/2$. We infer that the real parts of the point spectrum is exactly zero at $\alpha = \pi/2$. In other words, the breathing multichimera branches via non-standard Hopf bifurcation [23] at $\alpha = \pi/2$ since chimera solutions do not exist for $\alpha > \pi/2$ [11]. However, we were not able to confirm this inference numerically because it is difficult to distinguish the point spectrum whose real parts are almost zero for $\alpha \simeq \pi/2$ as shown in Fig. 5.13. According to the theory of Hopf bifurcation [1], the amplitude of the limit cycle is almost proportional to the positive real part of the point spectrum in the neighborhood of the bifurcation point. Fig. 5.14 looks as if $|Z(t)|$ does not oscillate periodically for $\alpha = 1.560$, but the oscillation is too small to get over the fluctuation in $|Z(t)|$ since the real part of the point spectrum is very small.

We also found that the real parts of eigenvalues belonging to the fluctuation of the essential spectrum become small as α is increased toward $\alpha = \pi/2$. The positive real parts of these eigenvalues correspond to instability caused by the finite discretization. Therefore, the degree of instability for multichimeras becomes smaller as α is brought close to $\pi/2$, which is similar to the appearance of the persistent chimera state with the sine coupling around $\alpha = \pi/2$ as mentioned in Chapter 4.

5.5 Summary of This Chapter

In this chapter, we studied the multichimera with two coherent and incoherent regions in one-dimensional nonlocally coupled phase oscillators and

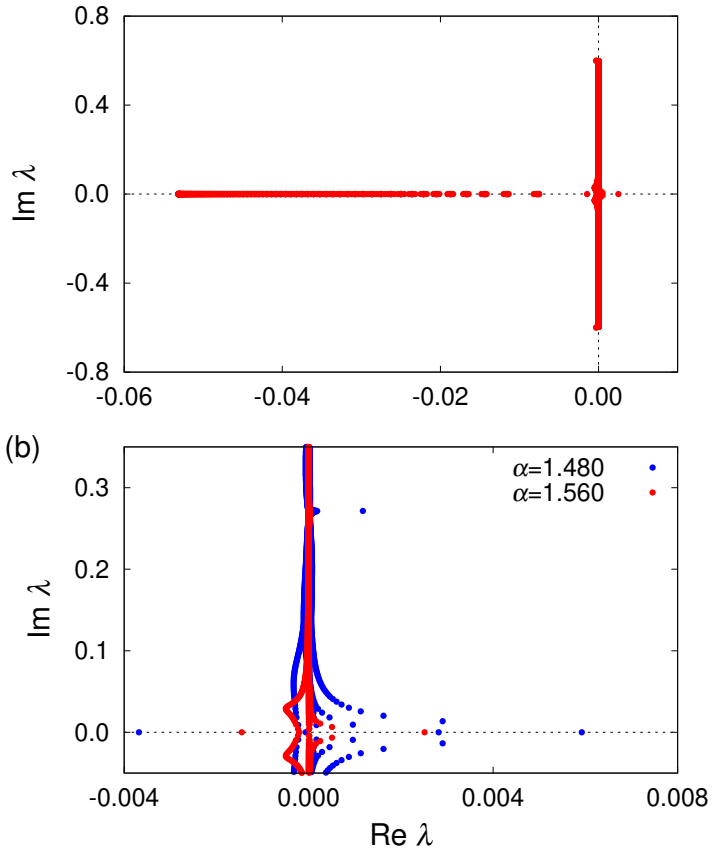

Figure 5.13: Complex eigenvalues λ of L_d with $M = 5000$, $s = 0.360$, and $\alpha = 1.560$. Figure (a) shows all eigenvalues. Figure (b) is the enlarged view of (a), and the blue points denotes eigenvalues for $\alpha = 1.480$ corresponding to Fig. 5.10.

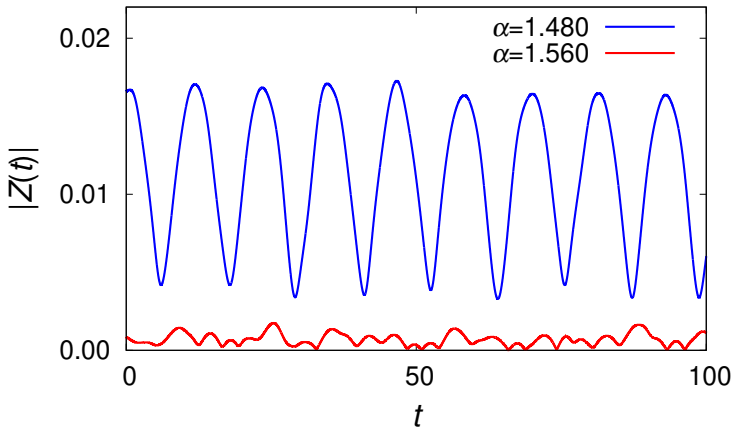

Figure 5.14: Time evolution of the global order parameter $|Z(t)|$ for the breathing multichimera with $N = 100000$, $\alpha = 1.560$, and $s = 0.360$ (red line). The blue line is the same as that in Fig. 5.4.

numerically found breathing multichimera states with oscillatory global order parameter $|Z(t)|$, without introducing phase lag parameter heterogeneity [7, 19, 21]. Moreover, we showed that the system exhibits a Hopf bifurcation from a stationary multichimera to a breathing one by the linear stability analysis for the stationary multichimera.

Furthermore, we showed that the local mean field $Y_{\rm st}(x)$ of stationary multichimeras depends on only odd harmonic coefficients g_{2m-1} of the coupling kernel $G(x)$. This means that if $G(x)$ has the same set of the odd harmonic coefficients, then $Y_{\rm st}(x)$ of stationary multichimeras are common to all those $G(x)$ systems for the same parameters. We were able to actually apply $Y_{\rm st}(x)$ of the $G_{\rm odd}(x)$ system to the linear stability analysis for the stationary multichimera in the $G(x)$ system, even though we were not able to obtain $Y_{\rm st}(x)$ of the stationary multichimera in the $G(x)$ system. The method used in this chapter is based on the fact that $Y_{\rm st}(x)$ of stationary multichimeras is characterized by only odd harmonic components, namely, Eq. (5.10). We expect that a similar method is applied to other stationary multichimera states because their local mean fields are also characterized by a set of specific harmonic components [11].

In contrast to the $G(x)$ system, multichimeras in the $G_{\rm odd}(x)$ systems can-

not breathe because the system converges on the solution satisfying Eq. (5.20) with vanishing $|Z(t)|$. Therefore, it is inferred that the coupling kernel is an important factor for the appearance of breathing chimeras in the one-dimensional system. It may be interesting to find other breathing chimeras by using other appropriate coupling kernels, but it is an open problem.

Chapter 6

Appearance of New Coherent Regions

We continue to study breathing multichimeras in one-dimensional nonlocally coupled phase oscillators with the sine coupling. In this chapter, we demonstrate that there appears another type of breathing multichimera with multiple coherent regions whose average frequencies are respective different. New coherent regions suddenly appear in the incoherent regions of the original breathing multichimera. We show that the appearance of new coherent regions is caused by increasing the amplitude of the breathing. Moreover, we derive a new self-consistency equation extended for breathing chimeras and numerically solve it [24].

6.1 Another Type of Breathing Chimera

We continue to consider the system described as Eq. (5.1). In this system, there appears the breathing multichimera whose phase pattern looks the same as that of the stationary multichimera, as shown in Fig. 5.1. We call such a breathing multichimera type-1 below.

In contrast, the phase pattern of the breathing chimera reported by Bolotov *et al.* [19, 21] differs markedly in appearance from that of the stationary chimera, as shown in Fig. 6.1. They considered the one-dimensional system

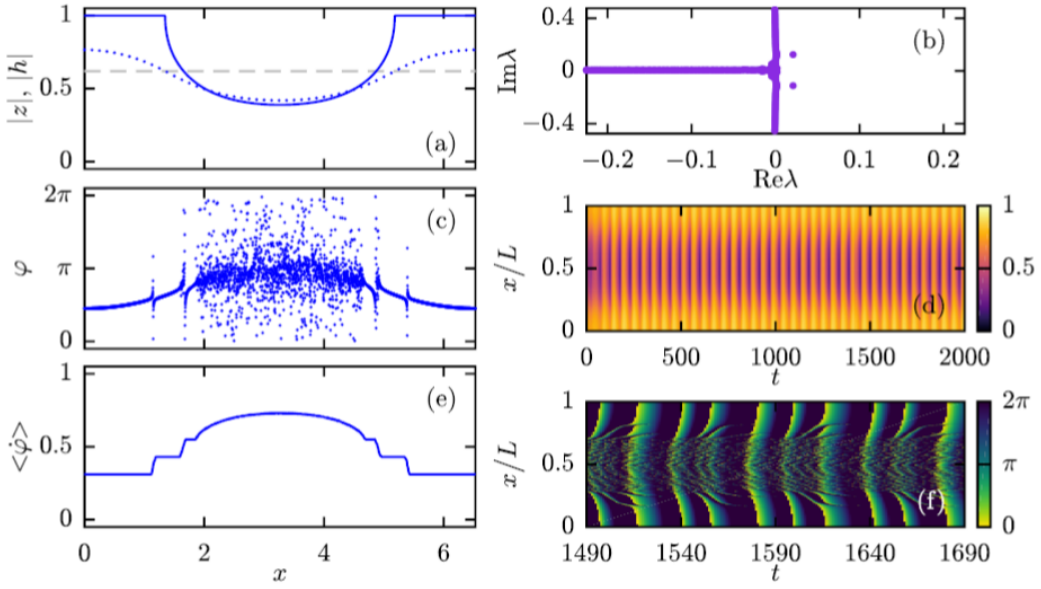

Figure 6.1: Breathing chimera state with phase lag parameter heterogeneity $\alpha = \alpha_0 + \alpha_1|Y(x,t)|^2$ with $\alpha_0 = 0.3\pi$ and $\alpha_1 = 0.65$. (b) All eigenvalues for the unstable stationary chimera state. (c) The snapshot of the phase $\varphi(x,t)$. (e) The profile of the average frequency $\langle\dot{\varphi}\rangle$. The details of figures (a), (d), and (f) are omitted [21].

with phase lag parameter heterogeneity $\alpha = \alpha_0+\alpha_1|Y(x,t)|^2$ and numerically demonstrated that such a breathing chimera appears for $\alpha_1 \neq 0$. However, we numerically found that there appears another type of breathing multichimera similar to it without introducing parameter heterogeneity, as shown in Fig. 6.2. We call the new breathing multichimera type-2 below. The type-2 breathing multichimera has two kinds of coherent regions with respective different average frequencies. The first coherent regions around $x = 0$ and $x = \pm\pi$ in Fig. 6.2(a) correspond to the coherent regions of the stationary or type-1 breathing multichimera, and the second coherent regions lie on the both sides of each first coherent region. The type-2 breathing multichimera appears in the blue region of Fig. 6.3. In our numerical simulations, there does not exist the bistable region of the type-1 and type-2. In this chapter, we aim for understanding these two types of breathing multichimeras theoretically.

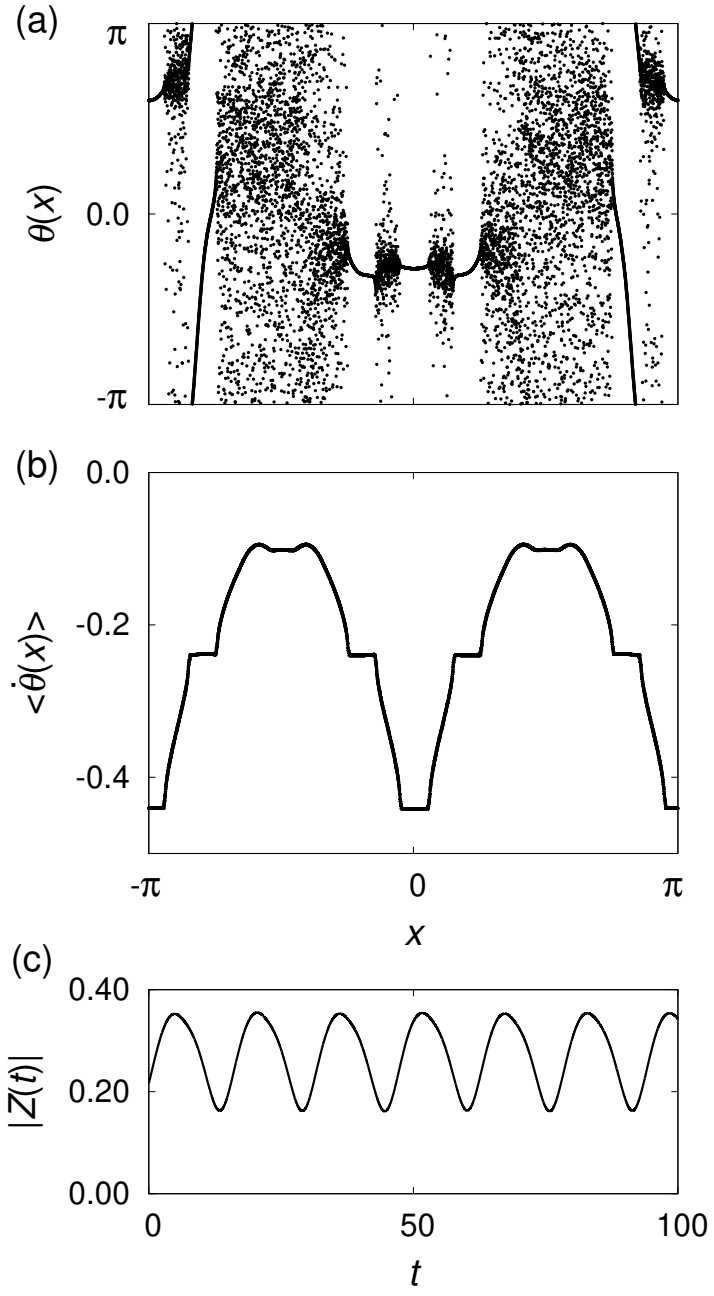

Figure 6.2: Type-2 breathing multichimera for Eq. (5.1) with $\alpha = 1.500$ and $s = 0.600$. (a) The snapshot of the phase $\theta(x,t)$. (b) The profile of the average frequency $\langle\dot{\theta}(x)\rangle$ with $T = 2000$. (c) Time evolution of the global order parameter $|Z(t)|$. These figures are obtained by the numerical simulation with (a)-(b) $N = 10000$ and (c) $N = 100000$.

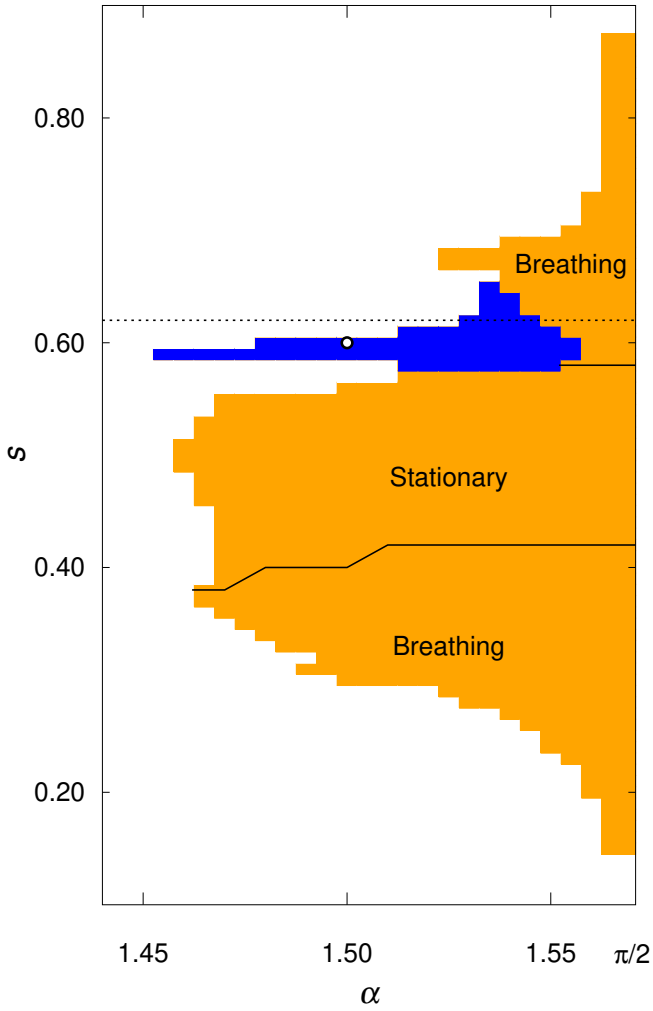

Figure 6.3: Stability region of multichimera states for Eq. (5.1) with $N = 100000$. The type-2 breathing multichimera appears in the blue region. The orange region is identical with Fig. 5.3.

6.2 Theory for Breathing Multichimeras

First, we study the properties common to the type-1 and type-2 breathing multichimeras. When the solution is stationary, the local order parameter $z(x,t)$ and the local mean field $Y(x,t)$ take the forms $z(x,t) = z_{\rm st}(x)\, e^{i\Omega t}$ and $Y(x,t) = Y_{\rm st}(x)\, e^{i\Omega t}$, respectively. For breathing multichimeras, we newly assume that the local mean field $z(x,t)$ takes the form

$$z(x,t) = \sum_{k=-\infty}^{\infty} z_k(x)\, e^{i(\Omega + k\delta)t}, \tag{6.1}$$

with the frequencies Ω and $\delta > 0$. This is the exponential Fourier series of $z(x,t)$. When $z_{k\neq 0}(x) = 0$, Eq. (6.1) recovers the stationary solution as $z_0(x) = z_{\rm st}(x)$. If the frequency Ω of the rotating flame is set to zero by choosing the suitable natural frequency, $z(x,t)$ oscillates around the center $z_0(x)$ in the phase space, and $z_{k\neq 0}(x)$ characterizes the amplitude of the breathing. Then, the local mean field $Y(x,t)$ is also obtained as

$$Y(x,t) = \sum_{k=-\infty}^{\infty} Y_k(x)\, e^{i(\Omega + k\delta)t}, \tag{6.2}$$

where $Y_k(x) := \int_{-\pi}^{\pi} dy\, G(x-y)\, z_k(y)$. Substituting Eq. (6.1) and Eq. (6.2) into the evolution equation

$$\dot{z}(x,t) = i\omega z(x,t) + \frac{1}{2}e^{-i\alpha}Y(x,t) - \frac{1}{2}e^{i\alpha}z^2(x,t)Y^*(x,t), \tag{6.3}$$

we obtain the equation for all k as

$$0 = i\Delta_k z_k(x) + \frac{1}{2}e^{-i\alpha}Y_k(x) - \frac{1}{2}e^{i\alpha}\sum_{l+m-n=k} z_l(x)z_m(x)Y_n^*(x), \tag{6.4}$$

where $\Delta_k := \omega - \Omega - k\delta$ $(= \Delta - k\delta)$. Similarly to the case of stationary chimeras, we also regard Eq. (6.4) as a quadratic equation in terms of $z_k(x)$:

$$0 = A_k(x){z_k}^2(x) - 2B_k(x)z_k(x) + C_k(x), \tag{6.5}$$

where

$$A_k(x) := e^{i\alpha} Y_k^*(x), \tag{6.6}$$

$$B_k(x) := i\Delta_k - e^{i\alpha} \sum_{l \neq k} z_l(x) Y_l^*(x), \tag{6.7}$$

$$C_k(x) := -e^{-i\alpha} Y_k(x) + e^{i\alpha} \sum_{\substack{l \neq k \\ m \neq k}} z_l(x) z_m(x) Y_{l+m-k}^*(x), \tag{6.8}$$

and obtain the solution

$$z_k(x) = \frac{B_k(x) + \{{B_k}^2(x) - A_k(x) C_k(x)\}^{\frac{1}{2}}}{A_k(x)}. \tag{6.9}$$

As the argument of the square root in Eq. (6.9), we choose either one that satisfies $|z(x,t)| \leq 1$ and that is stable if it belongs to the coherent regions ($|z(x,t)| = 1$). We can regard Eq. (6.9) as a new self-consistency equation for the set of the complex functions $z_k(x)$ and numerically solve it in Section 6.4.

By using Eq. (6.1), we can obtain the average frequency $\langle \dot{\theta}(x) \rangle$ for breathing multichimeras. To simplify notation, we define an integral operator $\mathcal{D}$ as

$$\mathcal{D}A := \lim_{\epsilon \to 0+} \frac{1}{2\epsilon} \int_{x-\epsilon}^{x+\epsilon} dy\, A(y). \tag{6.10}$$

Then, $z(x,t)$ is described as $\mathcal{D}e^{i\theta}$. $\mathcal{D}A$ denotes that the function $A(x)$ is averaged in the neighborhood of a point x. Note that the continuous functions for x, e.g. $Y(x,t)$, are not affected by $\mathcal{D}$. Operating $\mathcal{D}$ on Eq. (5.21), we have

$$\begin{aligned} \mathcal{D}\,\dot{\theta} &= \mathcal{D}\,(\,\omega - \mathrm{Im}[e^{i\alpha} e^{i\theta} Y^*]\,) \\ &= \omega - \mathrm{Im}[e^{i\alpha} z(x,t)\, Y^*(x,t)]. \end{aligned} \tag{6.11}$$

Interestingly, the right-hand side of Eq. (6.11) is identical with that of Eq. (2.43) obtained together with Eq. (6.3) by the Watanabe-Strogatz approach. Averaging both sides of Eq. (6.11) temporally, we have

$$\langle \dot{\theta}(x) \rangle = \omega - \mathrm{Im}[e^{i\alpha} \langle z(x)\, Y^*(x) \rangle], \tag{6.12}$$

since

$$\langle \mathcal{D}\,\dot{\theta} \rangle = \mathcal{D}\,\langle \dot{\theta} \rangle = \langle \dot{\theta}(x) \rangle. \tag{6.13}$$

Moreover, because

$$\langle z(x)\,Y^*(x) \rangle = \sum_{k=-\infty}^{\infty} z_k(x)\,Y_k^*(x), \tag{6.14}$$

is established under a sufficiently long measurement time, we finally obtain the average frequency for breathing multichimeras as

$$\langle \dot{\theta}(x) \rangle = \omega - \mathrm{Im}\left[e^{i\alpha} \sum_{k=-\infty}^{\infty} z_k(x)\,Y_k^*(x) \right]. \tag{6.15}$$

From Eq. (6.9), Eq. (6.15) is rewritten as

$$\langle \dot{\theta}(x) \rangle = \Omega + k\delta - \{ {B_k}^2(x) - A_k(x) C_k(x) \}^{\frac{1}{2}}. \tag{6.16}$$

For stationary multichimeras ($z_0(x) = z_{\mathrm{st}}(x)$ and $z_{k\neq 0}(x) = 0$), Eq. (6.16) for $k = 0$ is identical with Eq. (3.33) derived by Kuramoto and Battogtokh [3].

Let us consider the linear stability with respect to the short-wavelength perturbation. Now, let the phase $\theta(x,t)$ be the breathing multichimera satisfying Eq. (6.1). It is assumed that the local mean field $Y(x,t)$ is invariable when a small perturbation $\phi(x,t)$ is added to only one phase oscillator at a point x. Then, substituting $\theta(x,t) + \phi(x,t)$ into $\theta(x,t)$ in Eq. (5.21), we obtain a linear evolution equation for $\phi(x,t)$ as

$$\dot{\phi}(x,t) = [\partial_\theta V(\theta, x)]\,\phi(x,t), \tag{6.17}$$

$$\partial_\theta V(\theta, x) = -\mathrm{Re}[e^{i\alpha} e^{i\theta(x,t)} Y^*(x,t)], \tag{6.18}$$

where $V(\theta, x)$ denotes the right-hand side of Eq. (5.21). Operating $\mathcal{D}$ on Eq. (6.18) and averaging it temporally, from Eq. (6.14), we finally obtain

$$\langle \partial_\theta V(x) \rangle = -\mathrm{Re}\left[e^{i\alpha} \sum_{k=-\infty}^{\infty} z_k(x)\,Y_k^*(x) \right]. \tag{6.19}$$

Then, we have expected that $\langle \partial_\theta V(x) \rangle$ is the continuous function for x that is not affected by $\mathcal{D}$, though $\partial_\theta V(\theta, x)$ is not continuous. Eq. (6.19) determines whether or not the breathing multichimera is stable with respect to the short-wavelength perturbation. When the breathing multichimera is stable, we obtain $\langle \partial_\theta V(x) \rangle < 0$ in the coherent regions and $\langle \partial_\theta V(x) \rangle = 0$ in the incoherent regions. Note that even if $\langle \partial_\theta V(x) \rangle \leq 0$ for all x, the breathing multichimera is not always stable.

The right-hand sides of Eq. (6.15) and Eq. (6.19) can be combined into a complex equation

$$f(x) := i\omega - e^{i\alpha} \sum_{k=-\infty}^{\infty} z_k(x)\, Y_k^*(x). \tag{6.20}$$

Fig. 6.4 shows the profiles of Eq. (6.20) for the type-1 and type-2 breathing multichimeras and agrees with our analytical calculation. Thus, Eq. (6.20) is the important function describing the properties for breathing multichimeras. In the case of stationary chimeras, Eq. (6.20) and its complex conjugate are identical with the essential spectrum given as Eq. (3.47) if the natural frequency ω is set to the appropriate value such that $\Omega = 0$.

6.3 Relation between Breathing Multichimeras

Next, we study the relation between the type-1 and type-2 breathing multichimeras. In this section, we fix the parameter $s = 0.620$, denoted by the black dotted line in Fig. 6.3. In our numerical simulation, there appear the type-1 for $1.550 \leq \alpha < \pi/2$ and the type-2 for $\alpha < 1.550$. Then, the real part of the point spectrum, which characterizes the amplitude of the limit cycle oscillation, increases monotonically as α is decreased from $\pi/2$, similarly to Section 5.4.2. From this result, we suppose that the type-1 breathing multichimera changes to the type-2 by increasing the amplitude of the breathing. In other words, when the effect of $z_{k\neq 0}(x)$ becomes large, the second coherent regions suddenly appear in the incoherent regions of the type-1 breathing multichimera.

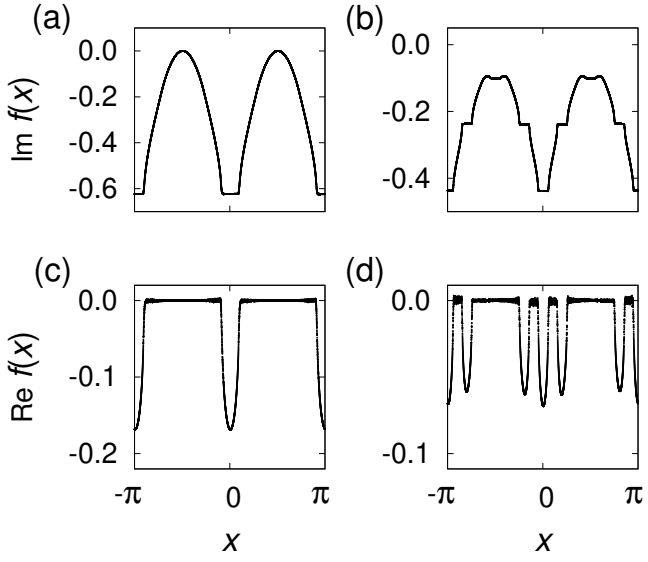

Figure 6.4: Profile of Eq. (6.20) for breathing multichimeras with $N = 10000$. (a)-(b) The imaginary part corresponds to the average frequency, and (c)-(d) the real part corresponds to the linear stability with respect to the short-wavelength perturbation. Figures (a) and (c) denote the type-1 for $\alpha = 1.480$ and $s = 0.360$, and Figures (b) and (d) denote the type-2 in Fig. 6.2. All figures are depicted from $\langle z_k(x) \rangle$ and $\langle Y_k(x) \rangle$ for $k \in [-5, 5]$ obtained by the numerical simulation.

6.3.1 Type-1 Breathing Multichimera

If the type-1 breathing multichimera appears during its small amplitude of the breathing after a Hopf bifurcation, the coefficient functions $z_k(x)$ of the local order parameter $z(x,t)$ may satisfy

$$z_k(x) = O(\varepsilon^{|k|}), \tag{6.21}$$

where ε is a sufficiently small value [1]. Then, those of the local mean field $Y(x,t)$ also satisfy $Y_k(x) = O(\varepsilon^{|k|})$ similarly. For $k = 0$, applying Eq. (6.21) to Eq. (6.9) and eliminating the $O(\varepsilon^1)$ terms, we have

$$z_0(x) = ie^{-i\alpha} \frac{\Delta_0 - \sqrt{{\Delta_0}^2 - |Y_0(x)|^2}}{Y_0^*(x)}, \tag{6.22}$$

then $A_0(x) = e^{i\alpha}Y_0^*(x)$, $B_0(x) = i\Delta_0$, and $C_0(x) = e^{-i\alpha}Y_0(x)$. This equation is identical with Eq. (5.19) for the stationary multichimera. Therefore, we obtain $z_0(x) \simeq z_{\rm st}(x)$, $Y_0(x) \simeq Y_{\rm st}(x)$, and $\Delta_0 \simeq \Delta$, where $z_{\rm st}(x)$, $Y_{\rm st}(x)$, and Δ correspond to the unstable stationary multichimera with same parameters. In fact, the time-averaged $\langle Y_0(x)\rangle$ for the type-1 breathing multichimera and the numerical solution $Y_{\rm st}(x)$ to the self-consistency equation (5.7) look like identical, as shown in Fig. 6.5.

Since $z_0(x)$ corresponds to the origin of oscillation, $z_k(x)\, e^{ik\delta t}$ for $k = \pm 1$ are the main terms characterizing oscillation for the type-1 breathing multichimera. Applying Eq. (6.21) to Eq. (6.9) for $k = \pm 1$ and eliminating the $O(\varepsilon^2)$ terms, we have

$$z_k(x) = \frac{-e^{-i\alpha}Y_k(x) + e^{i\alpha}{z_0}^2(x)Y_{-k}^*(x)}{2[i\Delta_k - e^{i\alpha}z_0(x)Y_0^*(x)]}. \tag{6.23}$$

$z_{\pm 1}(x)$ has order of ε^1 for almost all x, but it would become large rapidly at special points $x = x_s$ such that

$$i(\Omega + k\delta) = i\omega - e^{i\alpha}z_0(x)Y_0^*(x), \tag{6.24}$$

since the denominator of the right-hand side of Eq. (6.23) becomes zero. Remarkably, the right-hand side of Eq. (6.24) is identical with Eq. (6.20) for the unstable stationary multichimera. In the incoherent regions, Eq. (6.20) is a pure imaginary number, and its imaginary part corresponds to the average frequency. For stationary multichimeras in the present system, the average frequency of the coherent region is equal to $\Omega < 0$, which is the minimum value of the average frequency. Therefore, if $\Omega + \delta$ with $\delta > 0$ is less than the maximum value of the average frequency, there exist the points x_s such that Eq. (6.24) for $k = 1$. Note that δ is nearly equal to the absolute value of the imaginary part of the point spectrum in the neighborhood of a Hopf bifurcation point.

Such a profile as $|z_1(x)|$ becomes large rapidly is particularly observed just before switching to the type-2 breathing multichimera. In Fig. 6.6, we compare the type-1 and type-2 breathing multichimeras before and after

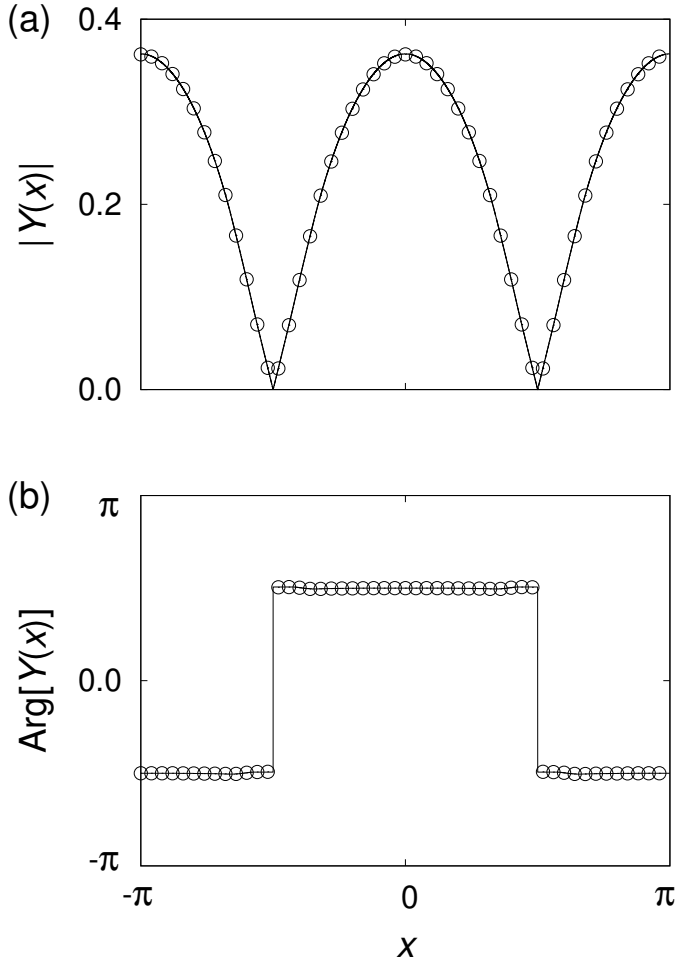

Figure 6.5: Local mean field of the type-1 breathing multichimera. (a) The amplitude; (b) the argument. Open circles denote the time-averaged $\langle Y_0(x)\rangle$ with $N = 100000$, $\alpha = 1.551$ and $s = 0.620$. Those circles are plotted once every 2000 oscillators. The solid line denotes the numerical solution $Y_{\rm st}(x)$ to the self-consistency equation (5.7) with same parameters. This solution corresponds to the unstable stationary multichimera.

switching from the type-1 to the type-2. For the type-1 with $s = 0.620$ and $\alpha = 1.551$ [see the left low in Fig. 6.6], we obtained $\Omega \simeq -0.3602$ and $\delta \simeq 0.2151$ by the numerical simulation, then Eq. (6.24) is established for $k = 1$. As shown in Fig. 6.6(g), $|z_1(x)|$ is very small for almost all x, but it becomes large rapidly at the points x_s such that $\langle \dot{\theta}(x_s) \rangle = \Omega + \delta$.

6.3.2 Type-2 Breathing Multichimera

For the type-2 breathing multichimera, $z_0(x)$ is not identical with $z_{\rm st}(x)$ clearly, as shown in Fig. 6.6(f), and the order of $z_{k\neq 0}(x)$ is larger than that of the type-1, as shown in Figs. 6.6(g) and (h). Therefore, the coefficient functions $z_k(x)$ of the local order parameter does not satisfy Eq. (6.21)

In our numerical simulation, we obtained $\Omega \simeq -0.3974$ and $\delta \simeq 0.2067$ for the type-2 with $s = 0.620$ and $\alpha = 1.549$. When Figs. 6.6(a) and (b) are compared, we observe that a part of the incoherent region for the type-1 suddenly changes the second coherent region for the type-2. Remarkably, the second coherent regions appear at the same points as x_s for the type-1 and have the average frequency $\Omega + \delta$. From this result, we can explain that the type-1 breathing multichimera changes to the type-2 by increasing the amplitude of the breathing, as follows. After the non-standard Hopf bifurcation at $\alpha = \pi/2$, there appears the type-1 breathing multichimera with small oscillation. The amplitude of this oscillation is mainly characterized by $z_{\pm 1}(x)$, which are very small for almost all x but large at x_s for $k = 1$. As α is decreased, $z_{\pm 1}(x)$, especially $z_1(x_s)$, gradually becomes large and reaches the threshold $|z(x,t)| = 1$ at x_s for $\alpha \simeq 1.550$. When α is decreased from $\alpha = 1.550$ again, $z_1(x_s)$ cannot become large anymore. Instead, the second coherent regions ($|z(x,t)| = 1$) with the average frequency $\Omega + \delta$ appear around x_s for increasing the amplitude of the breathing, in other words, the type-1 changes to the type-2. Such a scenario, that $|z(x,t)| = 1$ is realized at only one point and the coherent region appears around it, has analogy with the appearance of stationary chimeras at $\alpha = \pi/2$ [11,23]. As shown in Fig. 6.3, the type-1 breathing multichimera does not change to the type-2 for $s < 0.400$. This seems to be because an increase of the amplitude is smaller

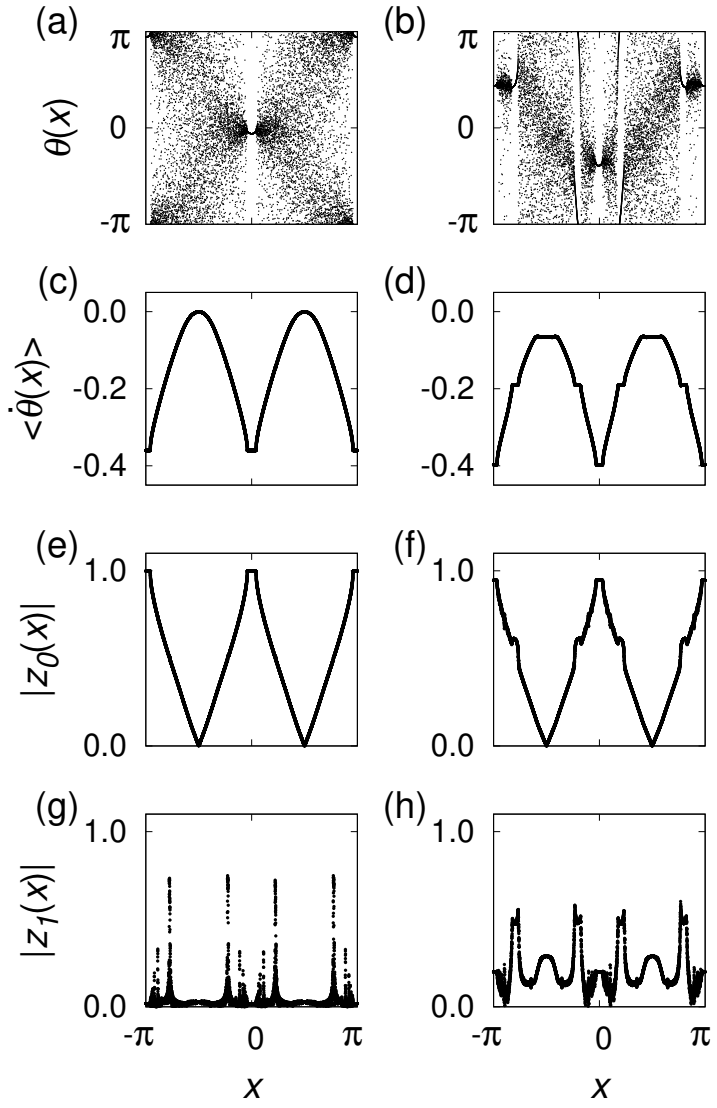

Figure 6.6: Comparison between the type-1 and type-2 breathing multi-chimeras with $N = 100000$ and $s = 0.620$. The left low denotes the type-1 for $\alpha = 1.551$, and the right low denotes the type-2 for $\alpha = 1.549$. (a)-(b) The snapshot of the phase $\theta(x,t)$; (c)-(d) the profile of the average frequency $\langle\dot{\theta}(x)\rangle$. Figures (e)-(f) and (g)-(h) show the amplitude of the time averaged $\langle z_0(x)\rangle$ and $\langle z_1(x)\rangle$, respectively. All figures are plotted once every 10 oscillators. The type-1 changes to the type-2 at $\alpha \simeq 1.550$.

than that for $s > 0.600$, but the correct reason is an open problem.

For $k \geq 2$, there can also exist special points similar to x_s, where Eq. (6.24) is satisfied, if $\Omega + k\delta$ is less than the maximum value of the average frequency. Then, the type-2 breathing chimera has not only the second coherent regions but the third coherent regions and more. Though such points for $k \geq 2$ do not exist in the present system, we have already seen the breathing chimera with the third coherent regions in Fig. 6.1. In fact, the average frequency of the third coherent regions looks to be equal to $\Omega + 2\delta$. We emphasize that our analytical theory mentioned in Sections 6.2 and 6.3 can be applied to the system with phase lag parameter heterogeneity only by replacing α to $\alpha(x)$.

6.4 Solving New Self-consistency Equation

In this section, we numerically solve the new self-consistency equation given as Eq. (6.9), especially, for the type-2 breathing multichimera. Eq. (6.9) are composed of one complex function for every k. Therefore, two additional conditions are wanting at least because there are the set of unknown complex functions $\{z_k(x)\}$ and two real unknowns Ω and δ. For stationary chimeras as mentioned in Sec. 3.2.2, the invariance under any rotation is utilized for solving the self-consistency equation. However, we need to prepare other additional conditions in the present case because the number of conditions are not yet enough to solve Eq. (6.9) if such a condition is added.

The function $f(x)$ given as Eq. (6.20) is beneficial for determining the frequencies Ω and δ. The average frequencies of the first and second coherent regions are equal to Ω and $\Omega + \delta$, respectively. Moreover, the stable coherent region satisfies $\mathrm{Re}f(x) < 0$ and has an extreme value of $\mathrm{Re}f(x)$ once every coherent region, as shown in Fig. 6.4. By using these properties, the frequencies Ω and δ can be considered as the dependent variables of $\{z_k(x)\}$. Letting x_{c1} and x_{c2} be extreme points in the first and second coherent regions, respectively, we obtain

$$\Omega = \mathrm{Im}f(x_{c1}), \tag{6.25}$$

$$\delta = \mathrm{Im}f(x_{c2}) - \mathrm{Im}f(x_{c1}), \tag{6.26}$$

where $\mathrm{Im}f(x_{c2}) > \mathrm{Im}f(x_{c1})$. The frequencies Ω and δ are uniquely determined according to Eqs. (6.25)-(6.26) with correct $\{z_k(x)\}$. Note that Eq. (6.25) is also established in the case of stationary chimeras. By adding Eqs. (6.25)-(6.26) to Eq. (6.9), we can obtain the complete self-consistency equation for the type-2 breathing multichimera.

There are several important points to numerically solve the new self-consistency equation. First, we modify $k \in [-\infty, \infty]$ to $k \in [-10, 10]$ on the basis of the assumption that $z_k(x)$ with sufficiently large $|k|$ is small enough not to affect the other $z_k(x)$. This is justified by the numerical simulation. Second, in order to compute Ω and δ more correctly, $\mathrm{Im}f(x_{c1})$ and $\mathrm{Im}f(x_{c2})$ in Eqs. (6.25)-(6.26) are replaced with the average values around each extreme point. The third point is the selection method of the argument of the square root in Eq. (6.9) that consists of two solutions. In our numerical calculation, we found that if all $z_k(x)$ are close to the correct solution, the order of these two solutions is greatly different except for $k = 0, 1$. Therefore, the larger one is easily rejected by the constraint condition $|z(x,t)| \leq 1$. However, such a selection is difficult in the first coherent regions for $k = 0$ and in the second coherent regions for $k = 1$ because the order of two solutions is not very different. Either of two solutions in these regions corresponds to the stable solution, and the other corresponds to the unstable one. This can be shown as follows. Eq. (6.9) is transformed to

$$f(x) = i(\Omega + k\delta) - \{{B_k}^2(x) - A_k(x)C_k(x)\}^{\frac{1}{2}}, \tag{6.27}$$

where $f(x)$ is the same function as Eq. (6.20). Interestingly, the left-hand side of Eq. (6.27) is independent of k. Since $\mathrm{Im}f(x) = \Omega$ in the first coherent regions, the square root for $k = 0$ is the real value that is identical with $\mathrm{Re}f(x)$. Therefore, one corresponding to $\mathrm{Re}f(x) < 0$ is stable, and the other corresponding to $\mathrm{Re}f(x) > 0$ is unstable. The same is true in the second coherent regions for $k = 1$. From this, we can select the stable one as the solution of Eq. (6.9) at almost all x for $k = 0, 1$. However, for the point x such that $\mathrm{Re}f(x) \simeq 0$, the stable and unstable solutions are too close to distinguish them. To solve this problem, we replace the terms corresponding

to the right-hand side of Eq. (6.27) in Eq. (6.9) for $k = 0, 1$ with the averaged value of those for $k \neq 0, 1$ if it is difficult to distinguish two solutions.

Fig. 6.7 shows the numerical solution to the new self-consistency equation for the type-2 breathing multichimera solved by the Steffensen's method. Open circles in Fig. 6.7 denote the time-averaged $\langle z_k(x) \rangle$ obtained by the numerical simulation, and we use them as the initial condition for solving the self-consistency equation. They look like identical. Although it may seem that they are not identical in a part of $|z_1(x)|$, that is caused by the calculation error depending on finite-size effects for the numerical simulation of Eq. (5.1). We succeeded in obtaining the solution to the self-consistency equation by using the initial condition that was very close to the correct solution. However, when other initial conditions was used, the correct solution was not able to be obtained because $\{z_k(x)\}$ diverged to infinity. This is a weak point of our numerical method.

6.5 Summary of This Chapter

In this chapter, we continued to study the breathing multichimera states and numerically demonstrated that there appear two types of breathing multichimeras. The type-1 breathing multichimera looks the same as the stationary multichimera at a glance, while the type-2 has multiple coherent regions with respective different average frequencies. This feature of the type-2 can be also seen for the breathing chimera with phase lag parameter heterogeneity [19, 21].

Next, as the properties common to the type-1 and type-2 breathing multichimeras, we derived the new self-consistency equation (6.9) and the function $f(x)$ given as Eq. (6.20) whose imaginary and real parts correspond to the average frequency and the linear stability with respect to the short-wavelength perturbation, respectively. By using these equations, it is shown that the type-1 breathing multichimera changes to the type-2 by increasing the amplitude of the breathing. Then, the second coherent regions with the average frequency $\Omega + \delta$ appear in the incoherent regions. Such transitions that new

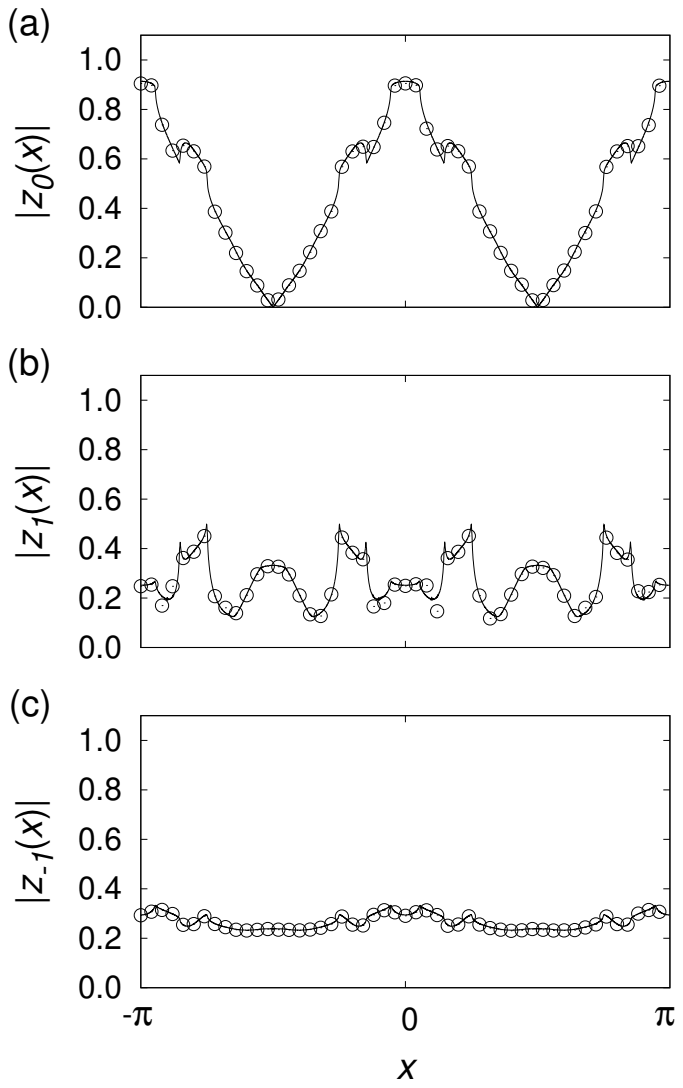

Figure 6.7: Local order parameter of the type-2 breathing multichimera for $\alpha = 1.500$ and $r = 0.600$ corresponding to Fig. 6.2. Figures show the amplitude of (a) $z_0(x)$, (b) $z_1(x)$, and (c) $z_{-1}(x)$. Open circles denote each time-averaged quantity obtained by the numerical simulation with $N = 100000$, and they are plotted once every 2000 oscillators. The solid line denotes the numerical solution to the new self-consistency equation.

coherent region appears in the incoherent region are often reported numerically in several systems different from the phase oscillator system [33, 38]. However, it is unclear whether those transitions in other systems are same as the present phenomenon.

Finally, we numerically solved the new self-consistency equation (6.9). Then, the frequencies Ω and δ is formulated as dependent variables of $\{z_k(x)\}$, given as Eqs. (6.25)-(6.26). Our numerical method succeeded in solving the self-consistency equation, but it was necessary to use the initial condition that was very close to the correct solution. For obtaining the breathing chimera solution more easily, we need to improve on the present method in future.

Chapter 7

Summary

The behavior of coupled oscillator systems can describe various pattern formations in a wide range of scientific fields. Among them, chimera states have especially attracted great interest of many researchers since the first discovery in 2002 [3]. In spite of long studies, there still remain some fundamental problems. This thesis has dealt with a few of such problems for chimera states in the one-dimensional array of nonlocally coupled phase oscillators.

In Chapter 2, we have reviewed the basic studies of phase oscillators and their synchronization. Moreover, in Chapter 3, we have reviewed the previous works of chimera states. In the previous works, it is reported that chimera states including multichimera states in the one-dimensional systems are stable in the continuum limit $N \to \infty$ and becomes chaotic transient in finitely discretized systems [8, 10]. In addition, chimera states in $N \to \infty$ have been assumed to be stationary states in most studies [3–6, 11, 13, 18, 19, 21–23]. This assumption forms the basis of the analytical theory for chimera states, e.g., the self-consistency equation of the local mean field and the linear stability analysis for stationary chimera states. In our studies, we answer two simple questions: (a) whether there exist persistent chimera states for finite N, and (b) whether there exist non-stationary chimera states in $N \to \infty$.

As the answer to the question (a), we have discovered the persistent chimera state, whose lifetime diverges to infinity even if N is finite, in the system with the Hansel-Mato-Meunier coupling [16], in Chapter 4. The per-

sistent chimera state appears not only in the unstable region of the completely synchronous solution but in its stable region. Furthermore, we have shown that chimera states in the system with the sine coupling can also become persistent by using appropriate parameters in the stability region of the completely synchronous solution. The persistency of chimera states are also agreed by the linear stability analysis for the stationary chimera state.

As the answer to the question (b), we have demonstrated that the breathing multichimera states appear in the system with the sine coupling without introducing phase lag parameter heterogeneity [22], in Chapter 5. The breathing multichimeras are characterized by oscillatory global order parameter, and there exist two types of breathing multichimeras. The type-1 breathing multichimera has the phase pattern similar to that of the stationary multichimera. We have shown that a type-1 breathing multichimera branches via Hoph bifurcation from a stationary one by the linear stability analysis for the stationary multichimera. The coupling kernel $G(x)$ is an important factor for the appearance of breathing multichimeras. In fact, the breathing multichimeras cannot appear in the G_{odd} system at least.

In Chapter 6, we have numerically demonstrated that there can also appear the type-2 breathing multichimera with multiple coherent regions whose average frequencies are respective different. Moreover, we have shown that the type-1 breathing multichimera changes to the type-2 by increasing the amplitude of the breathing. Our analytical theory for breathing multichimeras can also apply to the breathing chimera states with phase lag parameter heterogeneity [7, 19, 21]. Furthermore, we have derived a new self-consistency equation extended for breathing multichimeras and numerically solved it for the type-2 breathing multichimera.

Both of the persistency for finite N and the breathing behavior in $N \to \infty$ are related to the fundamental properties common to chimera states in the one-dimensional nonlocally coupled phase oscillator system that is one of the most basic models. We believe that our studies in this thesis will be helpful for a deeper understanding of chimera states.

Bibliography

[1] Y. Kuramoto, *Chemical Oscillation, Waves, and Turbulence* (Springer, Berlin, 1984).

[2] A. Pikovsky, M. Rosenblum, and J. Kurths, *Synchronization: A Universal Concept in Nonlinear Sciences* (Cambridge University Press, Cambridge, 2003).

[3] Y. Kuramoto and D. Battogtokh, Nonlinear Phenom. Complex Syst. **5**, 380 (2002).

[4] D. M. Abrams and S. H. Strogatz, Phys. Rev. Lett. **93**, 174102 (2004).

[5] D. M. Abrams and S. H. Strogatz, Int. J. Bifurc. Chaos **16**, 21 (2006).

[6] G. C. Sethia, A. Sen, and F. M. Atay, Phys. Rev. Lett. **100**, 144102 (2008).

[7] C. R. Laing, Physica D **238**, 1569 (2009).

[8] O. E. Omel'chenko, M. Wolfrum, and Y. L. Maistrenko, Phys. Rev. E **81**, 065201(R) (2010).

[9] M. Wolfrum, O. E. Omel'chenko, S. Yanchuk, and Y. L. Maistrenko, Chaos **21**, 013112 (2011).

[10] M. Wolfrum and O. E. Omel'chenko, Phys. Rev. E **84**, 015201 (2011).

[11] O. E. Omel'chenko, Nonlinearity **26**, 2469 (2013).

[12] Y. L. Maistrenko, A. Vasylenko, O. Sudakov, R. Levchenko, and V. L. Maistrenko, Int. J. Bifurc. Chaos **24**, 1440014 (2014).

[13] J. Xie, E. Knobloch, and H.-C. Kao, Phys. Rev. E **90**, 022919 (2014).

[14] P. Ashwin and O. Burylko, Chaos **25**, 013106 (2015).

[15] M. J. Panaggio and D. M. Abrams, Nonlinearity **28**, R67 (2015).

[16] Y. Suda and K. Okuda, Phys. Rev. E **92**, 060901 (2015).

[17] C. Bick and P. Ashwin, Nonlinearity **29**, 1468 (2016).

[18] L. Smirnov, G. Osipov, and A. Pikovsky, J. Phys. A **50**, 08LT01 (2017).

[19] M. I. Bolotov, L. A. Smirnov, G. V. Osipov, and A. S. Pikovsky, Jetp Lett. **106**, 393 (2017).

[20] H. Cheng, Q. Dai, N. Wu, Y. Feng, H. Li, and J. Yang, Commun. Nonlinear Sci. Numer. Simul. **56**, 1 (2018).

[21] M. Bolotov, L. Smirnov, G. Osipov, and A. Pikovsky, Chaos **28**, 045101 (2018).

[22] Y. Suda and K. Okuda, Phys. Rev. E **97**, 042212 (2018).

[23] O. E. Omel'chenko, Nonlinearity **31**, R121 (2018).

[24] Y. Suda and K. Okuda, (in preparation).

[25] S.-i. Shima and Y. Kuramoto, Phys. Rev. E **69**, 036213 (2004).

[26] E. A. Martens, C. R. Laing, and S. H. Strogatz, Phys. Rev. Lett. **104**, 044101 (2010).

[27] D. M. Abrams, R. Mirollo, S. H. Strogatz, and D. A. Wiley, Phys. Rev. Lett. **101**, 084103 (2008).

[28] A. Pikovsky and M. Rosenblum, Phys. Rev. Lett. **101**, 264103 (2008).

[29] M. J. Panaggio, D. M. Abrams, P. Ashwin, and C. R. Laing, Phys. Rev. E **93**, 012218 (2016).

[30] Y. Zhu, Z. Zheng, and J. Yang, Phys. Rev. E **89**, 022914 (2014).

[31] I. Omelchenko, Y. Maistrenko, P. Hövel, and E. Schöll, Phys. Rev. Lett. **106**, 234102 (2011).

[32] I. Omelchenko, B. Riemenschneider, P. Hövel, Y. Maistrenko, and E. Schöll, Phys. Rev. E **85**, 026212 (2012).

[33] I. Omelchenko, O. E. Omel'chenko, P. Hövel, and E. Schöll, Phys. Rev. Lett. **110**, 224101 (2013).

[34] L. Schmidt, K. Schönleber, K. Krischer, and V. García-Morales, Chaos **24**, 013102 (2014).

[35] S. W. Haugland, L. Schmidt, and K. Krischer, Sci. Rep. **5**, 9883 (2015).

[36] L. Schmidt and K. Krischer, Chaos **25**, 064401 (2015).

[37] I. Omelchenko, A. Zakharova, P. Hövel, J. Siebert, and E. Schöll, Chaos **25**, 083104 (2015).

[38] Q. Dai, D. Liu, H. Cheng, H. Li, and J. Yang, PLoS ONE **12(10)**, e0187067 (2017).

[39] A. M. Hagerstrom, T. E. Murphy, R. Roy, P. Hövel, I. Omelchenko, and E. Schöll, Nat. Phys. **8**, 658 (2012).

[40] M. R. Tinsley, S. Nkomo, and K. Showalter, Nat. Phys. **8**, 662 (2012).

[41] E. A. Martens, S. Thutupalli, A. Fourriére, and O. Hallatschek, Proc. Natl. Acad. Sci. USA **110**, 10563 (2013).

[42] D. P. Rosin, D. Rontani, N. D. Haynes, E. Schöll, and D. J. Gauthier, Phys. Rev. E **90**, 030902 (2014).

[43] B. van der Pol, Philos. Mag. **2**, 978 (1926).

[44] R. FitzHugh, Biophys. J. **1**, 445 (1961).

[45] J. Nagumo, S. Arimoto, and S. Yoshizawa, Proc. IRE **50**, 2061 (1962).

[46] A. L. Hodgkin and A. F. Huxley, J Physiol. **117(4)**, 500 (1952).

[47] I. Prigogine and R. Lefever, J. Chem. Phys. **48**, 1695 (1968).

[48] H. Sakaguchi and Y. Kuramoto, Prog. Theor. Phys. **76**, 576 (1986).

[49] S. Watanabe and S. H. Strogatz, Physica D **74**, 197 (1994).

[50] E. Ott and T. M. Antonsen, Chaos **18**, 037113 (2008).

[51] E. Ott and T. M. Antonsen, Chaos **19**, 023117 (2009).

[52] Y. Kuramoto, Prog. Theor. Phys. **94**, 321 (1995).

[53] D. Hansel, G. Mato, and C. Meunier, Phys. Rev. E **48**, 3470 (1993).

[54] H. Daido, Prog. Theor. Phys. **88**, 1213 (1992).

[55] K. Okuda, Physica D **63**, 424 (1993).

[56] H. Daido, Physica D **91**, 24 (1996).

[57] H. Kori and Y. Kuramoto, Phys. Rev. E **63**, 046214 (2001).

[58] P. Ashwin, O. Burylko, and Y. Maistrenko, Physica D **237**, 454 (2008).